12-8-2016

Predictive Modeling of a Two-stage Gearbox towards Fault Detection

Edward J. Diehl
University of Connecticut - Storrs, edward.diehl@uconn.edu

Predictive Modeling of a Two-stage Gearbox towards Fault Detection

Edward James Diehl, PhD

University of Connecticut, 2016

This research presents a systematic approach to health monitoring using dynamic gearbox models (DGM) and the harmonic wavelet transforms (HWT) for vibration response analysis. A comprehensive DGM is developed, the model parameters are identified through correlated numerical and experimental investigations, and HWT analysis is performed to illustrate the fault detection and diagnosis procedure and capability of this approach. The model fidelity is validated first by spectrum analysis, using constant speed experimental data, and secondly by HWT analysis, using non-stationary experimental data. The comparison confirms that both the frequency content and the predicted, relative response magnitudes match with physical measurements. Model prediction and experimental data are compared for healthy gear operation and seeded gear faults including a pinion with a missing tooth, tooth root crack, tooth spall and varying tooth chip severities, demonstrating that fault type and severity are distinguishable. The research shows fault modeling in combination with HWT data analysis is able to identify fault types, evaluate fault relative severity, and greatly reduce pattern recognition library development. This approach can facilitate successful fault detection, diagnosis and prognosis for gearbox systems, providing a physically meaningful connection of fault indicators to the actual fault patterns thus paving the way to real-time condition monitoring.

Predictive Modeling of a Two-stage Gearbox towards Fault Detection

Edward James Diehl

B.S., United States Merchant Marine Academy, 1992

M.S., Rensselaer Polytechnic Institute, 1996

A Dissertation

Submitted in Partial Fulfillment of the

Requirements for the Degree of

Doctor of Philosophy

at the

University of Connecticut

2016

APPROVAL PAGE

Doctor of Philosophy Dissertation

Predictive Modeling of a Two-stage Gearbox towards Fault Detection

Presented by

Edward James Diehl, B.S., M.S.

Major Advisor _____
Jiong Tang

Associate Advisor _____
Robert Gao

Associate Advisor _____
Brice Cassenti

Associate Advisor _____
Chengyu Cao

Associate Advisor _____
Xu Chen

University of Connecticut
2016

ACKNOWLEDGEMENTS

I want to acknowledge the people who have been so very crucial during my doctoral studies. Foremost, I would like to express my gratitude to my advisor Dr. Jiong Tang. Before applying to the University of Connecticut, when I was still uncertain if it would even be possible to change my career direction and pursue a PhD, I sent emails to several professors listed on the Mechanical Engineering Department website requesting a meeting to learn more about the program. Dr. Tang was the first professor to respond and agree to meet. His encouragement at that meeting, especially regarding becoming a teacher, inspired me to believe this dream was obtainable and to apply. After being accepted into the PhD program and learning that I was also offered a part-time lecturer position at the United States Coast Guard Academy, it was Dr. Tang who encouraged me that I would be able to balance both. It was Dr. Tang who helped me get funding for a research grant, and it has been his patience, motivation, enthusiasm and incredible insight that has helped me see this journey through. I feel incredibly lucky to have Dr. Tang as my advisor and mentor.

I would also like to thank Dr. Robert Gao, Dr. Brice Cassenti, Dr. Chengyu Cao and Dr. Xu Chen, for serving on my advisory committee. Their guidance, constructive criticism and support are most appreciated and invaluable.

Also, I am grateful to former and current colleagues in the Structure and System Dynamics Laboratory: Yi Lu, Shengli "Victor" Zhang, Kai Zhou, Ji Zhao, Qi Shuai, Jiawen Xu, Arun Hegde, Matthew Cremins, Pei Cao, Yuan Yuan and Shilong Li. Their teamwork and mutual support have been extremely important to me. I'm especially thankful for Yi's patience and guidance when I first joined our lab and for Victor's dedication and insight as we worked through research obstacles together.

Special thanks to my colleagues and students at the United States Coast Guard Academy. Without their support and constant encouragement, I could never have balanced my doctoral pursuit with my pursuit of a teaching career. In particular I'm appreciative of Dean Kurt Colella, Dr. Todd Taylor and CDR Mike Corl for taking a chance when hiring me seven years ago as a temporary lecturer and for

mentoring my teaching. Amongst the many faculty who have offered assistance in numerous ways, Dr. Bill Simpson, CDR Tom DeNucci, CDR Mike Plumley, CDR Dave Clippinger, Dr. Andy Foley, Dr. Elisha Garcia, and LT Sean Munnis have been especially helpful. I'm also very grateful for the cadets who have been and are my students. Teaching these incredible young men and women has motivated me to pursue this PhD so I might someday become a permanent faculty member.

Most importantly, I'd like to thank my family. My wife Lori is my best friend, shows me unconditional love and support, and has kept me laughing for the past twenty-five years. I can't express how much I appreciate my two amazing kids, John and Andrea, who have gracefully sacrificed some of the attention they deserved to allow me to pursue this dream. These three people are the center of my universe. I also want to acknowledge the role my older brother, James Diehl, has played in my life and in this journey. Jim's autism prevents him from communicating or revealing his hidden brilliance. At the approach of each important milestone in my life, I reflect upon the unfairness that Jim will never experience that milestone, and I'm inspired to push forward believing that my success is also his.

Finally, I appreciate the financial support of the National Science Foundation that funded parts of the research discussed in this dissertation.

TABLE OF CONTENTS

FIGURES

TABLES

NOMENCLATURE

I_i –mass moment of intertia, kg-m^2

m_n – lumped mass, kg

k_{ti} – torsional stiffness, N-m/rad

k_{bi} – shaft bending stiffness, N/m

k – bearing stiffness, N/m

k_{mj} – mesh stiffness, N/m

c_{ti} – torsional damping, N-s/rad

c_{bi} – shaft bending damping, N-s/m

c – bearing damping, N-s/m

c_{mj} – mesh damping, N/m

$\ddot{\theta}_i$ – rotational acceleration, rad/s^2

$\ddot{x}_n, \ddot{y}_n$ – translational acceleration, m/s^2

$\dot{\theta}_i$ – rotational velocity, rad/s

$\dot{x}_n, \dot{y}_n$ – translational velocity, m/s

θ_i – rotational displacement, rad

x_n, y_n – translational displacement, m

α – torque factor

T_i – applied torque, N-m

W_j – dynamic mesh force, N

DTE_1 – dynamic transmission error, rad

β – relative orientation of shaft, rad

ϕ – pressure angle, rad

Introduction

Background

Gears, commonly used to transmit torque, are critical moving components in many power systems including wind turbines, aircraft, automobiles, and ships. Gear-induced vibration has been widely studied and remains an important, fundamental topic in engineering. Tooth-meshing induces vibration with primary and harmonic tones spanning a very wide frequency range. Vibration signals from gearboxes are frequently used as information carriers for condition monitoring. Diagnosis and prognosis of gear faults remain topics of great importance and considerable research.

The variety of gearbox monitoring and diagnosis approaches can be loosely categorized into data-based, model-based, or a hybrid of these two. In data-based approaches, signal processing techniques are employed to seek faults by analyzing measured operational data to identify distinguishable features which indicate faults. These fault features are based on patterns learned from empirical experience. Fault detection based on signal processing alone can be characterized as a "black box" approach, as the specific physics of the system are not explicitly considered, only matching of processed data with known fault patterns. Conversely, model-based approaches to condition monitoring, often referred to as "white-box" approaches, can in theory provide baseline data by subjecting the model to the same operating condition of the actual system. Fault detection is facilitated by comparing the model prediction with the measurement data acquired by the monitoring system. A Dynamic Gear Model (DGM) is a lumped parameter model based on first principles intended to capture the underlying physics of the interaction between gear teeth, bearings and shafts and simulate the vibration response of the physical unit. Hybrid techniques attempt to merge data-based and model-based approaches to add physical meaning to the statistical and numerical

Condition monitoring of rotating machinery has historically been performed on machines operating at constant speeds by processing vibration data in the frequency domain, but frequency-domain techniques are not well suited for analyzing non-stationary signals such as machinery with changing speeds like wind turbines and ship propulsion plants. This complication can be overcome by remaining in the time-domain

or by applying time-frequency techniques. Time-frequency domain analysis reveals the waveform energy distribution across both time and frequency, and can be used to identify transient events as well as fault patterns. Within the variety of time-frequency techniques, wavelet analysis has become increasingly important in signal processing, and specifically the Harmonic Wavelet Transform (HWT) has shown promise in identifying faults in non-stationary gear vibration signals.

The goal of this research is to explore the extent to which combining HWT and DGM can be used to characterize faults so they may be identified and their severity evaluated. The eventual goal is to run the DGM in real-time with the machine, matching speed and load, while changing faults (types, severity, location within system) to identify them (diagnosis) and project total failure (prognosis).

Motivation

When gears malfunction, repairing or replacing the machinery is expensive; unfortunately periodic preventive maintenance is also costly. Therefore much attention has been focused on gearbox Condition Monitoring (CM) with the goal of developing a diagnosis and prognosis method with sufficient reliability to delay maintenance until it is truly needed. Numerous and diverse CM methods have been proposed, developed and tested towards creating a reliable predictive technique for gearboxes (Heng et al, 2009). The majority of CM methods rely on measuring and interpreting gear vibration signals. An effective gearbox CM based on vibration must process measured data and be capable of identifying the existence of a fault, classifying that fault and estimating the extent of the fault.

Many data-based CM approaches rely on some form of pattern recognition to detect and classify faults (Kan et al, 2015). Two major issues of this type of approach are the large quantity of data required to initialize the libraries and the difficulty to extrapolate the data from them. Gearbox vibration signals contain a complex mixture of harmonic and sub-harmonic components of mechanically induced motion from gear meshing, bearing rolling and driver and load motion and random noise. Much of the important information needed for condition monitoring is hidden by the undesired components within the signal; unfortunately decomposing a measured signal by filtering often leads to removal of desired content.

Other drawbacks of data-based CM approaches include the lack of physical interpretation and specificity to a particular piece of machinery, requiring machinery experience for each kind of fault in order to distinguish the specific fault.

A gearbox vibration signal can theoretically be mimicked by a DGM and a gear fault simulated to populate a signal processing fault library. Unfortunately, a well-known weakness of most modeling efforts is the difficulty in achieving precise, or even acceptable, correlation to measured data, since DGMs only simulate the deterministic dynamic behavior. Existing DGM literature shows a relatively limited amount of experimental correlation for model validation. Many DGM studies rely upon the experimental data obtained by a few benchmark single-stage testbeds dating back as far as the early 1960's (Munro, 1962). Experimental test data from multi-stage gear testbeds is even more rare in the literature search, as are multi-stage DGMs; furthermore no validated models are found (Velex, 2012).

The motivation behind this research is to address the shortcomings of the data-based CM approaches by developing a lumped parameter DGM, experimentally validating it, and processing both experimental data and DGM results which will demonstrate that a hybrid CM approach is feasible – even for non-stationary gearboxes.

Objectives and Scope

The objective of this research is to develop a CM approach merging signal processing and first-principles modeling of a benchmark two-stage gearbox testbed with non-stationary operation. The research develops a DGM with sufficient degrees-of-freedom (DOFs) to capture the physical behavior of the testbed at locations and in directions corresponding to the instrumentation. DGM parametric investigations and testbed experimental investigations are performed in parallel to refine and validate the model. Fault models are developed and used to mimic seeded faults in the testbed and detailed comparisons are performed using HWT, as well as traditional spectral analysis, to work towards identifying faults. Fault types and fault severities are investigated in the testbed and mimicked in the DGM to assist in identifying, classifying and assessing individual gear tooth faults. A changing shaft

speed-time profile is used with the equipment and mimicked with the DGM to address the difficulty of monitoring non-stationary machinery. To facilitate effective data processing, HWT is employed to analyze the features of the vibration responses for both test equipment and DGM, bridging the gap between data-based and model-based CM approaches. Different HWT resolutions are used to characterize faults with both frequency features and time features. HWT differentials of healthy/faulty DGMs operating at the exact same speed-profile are used to isolate the distribution of energy due to fault types and severities without the influence of random noise and speed variation inherent in measured data.

Outline

This research is organized in the following way: Chapter 1 presents an extensive literature review is presented to discuss the relevant research that informed this effort, Chapter 2 presents the experimental setup and investigations for parameters and fault models are documented, Chapter 3 describes the thorough DGM development which covers both single-stage and two-stage models with increasing complexity is provided, and Chapter 4 provides a detailed analysis of the data and model results using the HWT is performed. This dissertation concludes with the vision for future work to build upon this research in Chapter 5 and a summary of what was achieved in Chapter 6.

Chapter 1 – Literature Review

Introduction

Early identification of faults in a power transmission system, especially gear train, is essential to avoid catastrophic failures of the entire system. Additionally, sufficiently reliable health monitoring holds the potential to reduce scheduled preventive maintenance in favor of as-needed maintenance (Jardine et al, 2006). There exist numerous studies which focus on developing condition monitoring techniques that hold promise for identifying gear faults (Heng et al, 2009). Much of the relevant work can be broadly categorized into two groups: gear modeling and signal processing. This literature review is organized accordingly, emphasizing material relevant to the present research as well as works considered historically important to assist unfamiliar researchers to approach the topics.

1.1 Dynamic Gear Modeling

Dynamic Gear Models (DGM) are built from first principles to mimic the behavior of physical gearboxes. A search of scientific literature on gear modeling leads to a significant number of papers dating back several decades and continuing to the present. The following literature review attempts to provide background into the progression of DGM development, highlight the seminal works, and convey the direction of current and future research in gearbox modeling.

1.1.1 Dynamic Gear Modeling Literature Reviews

Literature reviews describing the state-of-the-art of dynamic gear modeling often chronicle the history and uses of gear models up to the time of publication, as well as attempt to classify the variety of types of models. A comprehensive review of the mathematical models used in gear dynamics as of 1988 was presented by Özgüven and Houser of The Ohio State University (OSU). In that paper Özgüven and Houser estimate that the first gear models began in the 1950's, and they list the objectives/purposes/goals of dynamic modeling as the study of noise control, stability analysis, stresses, pitting and scoring, transmission efficiency, loads on bearings, reliability, life, natural frequencies, whiling of rotors and

vibratory motion of the system. Özgüven and Houser classify dynamic gear models by simple dynamic factor models, models with tooth compliance, models for gear dynamics, models for geared rotor dynamics and models for torsional vibration while summarizing the evolution of dynamic gear models with respect to complexity, represented features, degrees-of-freedom and diversity of objectives. This article has been cited over 500 times and is the jumping off point for many dynamic gear model studies (Özgüven and Houser, 1988).

Wang, Li and Peng created a survey of the progress in DGMs as of 2003 emphasizing non-linear behavior in models. They classified the types of models as a) single-degree-of-freedom models, b) multiple degree-of-freedom models of a single gear pair, c) multi-degree-of-freedom models with multi gear pairs without shafts and bearings, and d) multi-degree-of-freedom models that include shafts, bearings, house, etc., noting that the first three were a simplification of the fourth. Wang et al also classified the two ways DGMs were computationally solved as numerically and analytically, breaking these down into subcategories where numerical computation includes digital and analog simulation time-domain numerical integration methods while analytical methods include piecewise-linear techniques, harmonic balance method, modal analysis method, perturbation method and shooting method (Wang et al, 2003). Another literature review updating the Özgüven and Houser review is (Parey and Tandon, 2003) which documented inclusion of friction into models and modeling of wear and spall gear faults.

Hiroaki and Nader (2012) summarize the relevant concepts, features, techniques, and limitations of dynamic gear models as well as many fault models. This article is a primer on gearbox simulation and includes the key elements of transmission error, gear geometry error, effect of load, gear dynamics, modeling rolling elements, gearbox casing modeling, model solution techniques, gear crack fault models, gear spall fault models, and rolling element spall fault models. Amongst the conclusions is the need for improving the correlation between simulated and measured signal and the promise that simulated signals can aid in the machine learning process for fault diagnosis algorithms (Hiroaki and Nader, 2012).

An article by Velex in 2012 presents an overview of the modeling of spur and helical gear dynamic behavior including three-dimensional lumped parameter models, parametric excitation, dynamic behavior,

transmission errors, practical considerations and the move towards continuous models. This paper concludes that while there are many dynamic gear models, there is limited experimental data available and "there is an urgent need for validated models…especially for complex multi-mesh systems." (Velex, 2012)

There are multiple ways to categorize DGMs including by the features included or excluded within the model, as done by Özgüven and Houser. Other means of categorizing dynamic gear models are by the purpose of the model, by number of degrees-of-freedom (DOFs) or gear system type, such as single-stage, multi-stage, planetary, etc., as well as spur versus helical type. This literature review mostly focuses on spur gear single- and two-stage gear systems. Since many of the DGM categorization strategies overlap, the organization of the DGM literature review section is somewhat loose. The following subsections describe DGM purposes, papers featuring DGM experimental validation, multi-shaft DGMs, DGM parameter papers (especially mesh stiffness and bearing stiffness), and DGMs with fault models. Throughout the DGM literature review, the number of DOFs is noted as an indication of the model complexity and summarized at the end of the section. Where appropriate, the papers are described chronologically or grouped by associated authors.

1.1.2 Dynamic Gear Model Complexity and Purposes

The complexity DGMs and the purposes for creating them are often linked since the physical motion desired must be included as a DOF. Below is a list of the various lumped parameter single-stage DGM DOFs discussed throughout this literature review, followed by Table 1 which summarizes the papers using these DGMs. This table allows for a comparison of degrees-of-freedom used, which is also an indication of model complexity and features represented. One might conclude from this list and table that while a wide variety of choices for model complexity have been made, simple models are still deemed useful by researchers.

- 1-DOF: Transmission Error
- 2-DOF: Rotational DOF for each gear
- 3-DOF: Transmission Error + 1x1-DOF bearing per shaft

- 4-DOF Rotational DOF for drive, gears and load, including shaft torsional stiffness
- 6-DOF: 4-DOF + 1x1-DOF bearing per shaft
- 9-DOF: 6-DOF + 2xbearing foundations + plate location of accelerometer
- 10-DOF: 3-DOF + 2x2-DOF lateral shaft + 2x2-DOF (x & y) bearings per shaft
- 12-DOF: 3 Rotational DOF and 3 Translational DOF per gear
- 14-DOF: 12-DOF + drive and load rotational DOF
- 16-DOF: 4-DOF + 2x2-DOF (x & y) bearings per shaft, including shaft bending stiffness
- 34-DOF: 16-DOF + multi-DOF bearings

Table 1. Summary of single-stage DGM literature model DOFs

Paper	DOFs
(Özgüven and Houser, 1988)	1
(Comparin and Singh, 1989)	1
(Kahraman and Singh, 1990)	1
(Amabili and Fregolent, 1998)	1
(Bonori and Pellicano, 2007)	1
(Ding and Kahraman, 2007)	1
(Tamminana et al, 2007)	1
(Velex and Ajmi, 2007)	1
(Dion et al, 2009)	1
(Faggioni et al, 2011)	1
(Guilbault et al, 2012)	2
(Kahraman and Singh, 1991)	3
(Maliha et al, 2004)	3
(Lin et al, 1994)	4
(Özgüven, 1991)	6

Paper	DOFs
(Choy et al, 1993)	6
(Bartelmus, 2001)	6
(Parey et al, 2006)	6
(He, 2008)	6
(Wu et al, 2008)	6
(Zhou and Zuo, 2012)	6
(del Rincon et al, 2013)	6
(Inalpolat et al, 2015)	6
(Omar et al, 2011)	9
(Wan et al, 2014)	10
(Ma et al, 2015)	12
(Velex and Maatar, 1996)	14
(Zhou and Zuo, 2012)	16
(Sawalhi and Randall, 2008)	34

The number of degrees-of-freedom (DOFs) representing a two-stage gear set in a DGM can range from a minimum of two (in which the angular displacement difference – transmission error – of each shaft are the variables) to very large finite element models incorporating every physical parameter. The DOF quantity must be sufficiently complex to capture desirable features while being small enough for practical solution speeds. A partial list of two-stage DGM potential DOFs is the following:

- 2-DOF: Transmission Error for each gear pair
- 3-DOF: Rotational DOF for each shaft
- 6-DOF: Rotational DOF for drive, gears and load, including shaft torsional stiffness
- 9-DOF: 6-DOF + 1x1-DOF bearing per shaft,
- 9-DOF: 3-DOF + 1x2-DOF (x & y) bearings per shaft
- 12-DOF: 6-DOF + 2x1-DOF bearing per shaft
- 26-DOF: 6-DOF + 2x2-DOF (x & y) bearings per shaft, including shaft bending stiffness

This list is not inclusive, of course, since there are numerous other features that may be included and represented by DOFs and FEA models of the gear housing may be paired with multibody kinematic

models of the gears to create limitless model sizes. Table 2 summarizes the DOFs used in two-stage DGM in this literature review. A comparison to single-stage DGMs in Table 1 shows substantially fewer examples and more variety of model sizes.

Table 2. Summary of two-stage DGM literature model DOFs

Paper	DOFs
(Al-shyyab and Kahraman, 2005)	2
(Yang, 2013)	2
(Al-shyyab and Kahraman, 2007)	6
(Liu and Parker, 2008) (Note: idler gear DGM)	8
(Kubur and Kahraman, et al, 2004)	12
(Walha, 2012)	12
(Jia et al, 2003)	26

While modeling efforts share the goal of replicating the complex physics of power transmission through gear interaction, dynamic gear models have been created and studied for other purposes besides condition monitoring. These non-condition monitoring purposes include:

- Simulating the dynamic load factors for stress calculation
- Investigating the dynamic force response "jump phenomenon" at resonant frequencies
- Determining the influence of key system parameters

The dynamic load factor adjusts gear stress formulae to account for the effects of a dynamically applied loads rather than static loads (Shigley et al, 2014). Dynamic load factors have historically been entirely empirical estimates. DGMs have been useful in updating and refining the dynamic load factors, establishing a closer link to first principles. Tamminana et al used a single-degree-of-freedom model solved with Rung-Kutta numerical integration in 2007 to compare the relationship between dynamic factors and transmission error (Tamminana et al, 2007). Velex and Ajmi use a single-degree-of-freedom helical gear model to establish a set of generalized formulae for finding the dynamic factor for helical gears (Velex and Ajmi, 2007).

Among the most common uses of DGM for research is studying the "jump phenomenon" of gearboxes that occurs during acceleration or deceleration when passing through resonant frequencies. This behavior, often also referred to as "dynamic instability", is typical of a non-linear system in that it

might have two or more possible solutions for a given input parameter. In the case of gearboxes, the input parameter is speed and the measured solution is the root-mean-square of the dynamic transmission error. The region of overlap of speeds, where the solution might be one of two values, is most often dependent on whether the speed was approached by accelerating or decelerating to it; this state is described as "chaotic." A significant amount of work performed at OSU dealt with or used this jump phenomenon and many papers demonstrated its dependence on the backlash clearance-type non-linearity.

In 1988, the same year as their comprehensive literature review, Özgüven and Houser performed a dynamic analysis of a high speed gearset using a single-degree-of-freedom model that was condensed from two rotational degrees-of-freedom into the transmission error between gears as the motion variable. This model was solved with a FORTRAN Runge-Kutta-Verner method and the resulting dynamic factor versus rotation speed compared to results of Kubo's 1972 experiments which show trending agreement for peaks in and around the resonant speeds. This model demonstrated the loss of contact and back-side collision due to backlash causes the jumps (Özgüven and Houser, 1988).

A 1989 paper by Comparin and Singh, also of OSU, also used the single-degree-of-freedom model but solved with the harmonic balance method with comparisons to analog and digital solutions. The model was used to study the non-linear frequency response of "an impact pair" as a general issue of clearance non-linearity, drawing comparisons to the cubic non-linearity of Duffing's equation. The comparison serves to explain the non-linear nature of the behavior (Comparin and Singh, 1989).

A 1990 article by Kahraman and Singh of OSU describes the non-linear dynamics of a spur gear pair again using a single-degree-of-freedom model solved with the harmonic balance method. This paper also studied the non-linear "jump" phenomenon and compared the dynamic transmission error versus operating speed from experiments by (Munro, 1962). In 1991, the authors extended their study to two and three-degree-of-freedom models and performed a variety of parametric studies with and without backlash and linear or non-linear bearings. They also identified conditions for chaotic and subharmonic resonances and non-linear modal interactions. This study also uses Munro's 1962 experimental data for validation (Kahraman and Singh, 1990).

A 1991 paper by Özgüven describes a six degree-of-freedom model which includes a rotational degree-of-freedom for the drive, pinion, gear and load and translational DOFs at the pinion and at the gear to represent the bearings. This model includes torsional stiffness for each shaft. The six second-order differential equations-of-motion are re-written into twelve first-order equations and solved with a fifth order Runge-Kutta adaptive step size algorithm. Parameters for the model match Kubo's 1978 test rig as closely as possible, using estimations where information was unavailable. The model was not compared to Kubo's experimental results but instead used for a parametric study to investigate the effect of varying bearing stiffness and shaft stiffness on the dynamic factor versus pinion speed (Özgüven, 1991). Özgüven's paper is noteworthy because it has been cited by numerous subsequent modeling papers as the basis for their model. A relevant example is (Parey et al, 2006) followed by a book (Parey and Tandon, 2010), which form the basis of the single-stage model used in this research.

Involute gears are rarely, if ever, perfectly machined to the ideal involute profile shape, consistent pitch or geometry. These manufacturing errors produce gear noise and vibration. Furthermore, purposeful changes are made to the gear profile to correct for interference, allow for small amounts of misalignment and to more evenly distribute teeth loads by undercutting, profile modifications, crowning and tip relief, respectively. DGMs have been used to study the effect of these changes with a variety of modeling techniques (Lin et al, 1994; Velex and Maatar, 1996; Amabili and Fregolent, 1998; Bartelmus, 2001; Bonori and Pellicano, 2007; Liu and Parker, 2008; Inalpolat et al, 2015).

Dynamic gear models have been used for condition monitoring in the following ways:

- Assisting in the decomposition of gear vibration signals
- Trying out new diagnostic and prognostic detection algorithms in lieu of experiments
- Understanding the nature of gear faults

Since gearbox vibration signals are made up of many different frequencies and random noise, measured signals are often filtered to remove the unwanted frequencies, but choosing the right filter requires one to know what one is looking for prior to filtering. DGMs can assist to guide an engineer to filter out all but the frequency content relevant to diagnosing the machinery condition (Parey et al, 2006).

Endo et al (2009) used signal processing to filter a vibration signal into parts: inherent gear vibration, noise, and fault impulses. They used FEA models to characterize expected changes in mesh stiffness due to specific gear tooth faults, dubbed these changes "residual transmission error", and compared the second derivative to the filtered fault impulse portion of the processed signal. The approach of (Endo et al, 2009) could very well be considered hybrid, especially since their filter was autoregressive.

DGMs are useful for trying out new diagnostic and prognostic detection algorithms because a faulty signal can be simulated rather than waiting for a fault to naturally occur or fake a fault ("seed") in the experimental equipment. DGMs often incorporate gear fault models to investigate the nature of the fault vibratory signature to assist in its detection. The fault modeling literature review is described in detail in a later subsection.

1.1.3. Single-Stage Dynamic Gear Models and Experimental Comparisons

When developing any DGM, the primary concern is validating that the physics are accurately represented. A detailed review of the relevant DGM literature, which includes hundreds of research papers, shows a relatively limited amount of experimental data has been relied upon for model validation. Much of the experimental verification of dynamic gear models was based on the data available from (Munro, 1962) and (Kubo, 1978) until OSU in cooperation with General Motors published a series of experimental investigations in 1996 (Blankenship and Kahraman, 1996; Kahraman and Blankenship, 1996; Kahraman and Blankenship, 1997; Kahraman and Blankenship, 1997). These papers not only characterized the forced response of a gear pair but also sought to determine the influence and effect of contact ratio and tip relief on that response. Again, the jump phenomenon was a featured aspect of these investigations as most results demonstrated these in graphs of root-mean-square dynamic transmission error (DTE) magnitude versus machine operating speed (often non-dimensionalized by dividing by the principle resonant frequency) . The conference papers originally presenting these experimental results were later updated and published in journal articles. The conclusions drawn from these experiments were: 1.) forced response is highly dependent on torque, 2.) for any given tip relief there is a torque that

will yield minimum DTE, and 3.) spur gear pairs with integer contact ratios produce the minimum DTE. Accompanying these studies were single-degree-of-freedom models the authors found "adequate" to describe the effects the parameters had on DTE, although actual diagrams showing model results were not available and/or omitted from copies of the paper.

The data from OSU's 1996 papers has been used repeatedly in subsequent articles from that institution as well as by numerous other authors to validate their models. Maliha et al used OSU data as well as Kubo's data to validate their three-degree-of-freedom model which used finite elements and describing functions (Maliha et al, 2004). Faggioni et al used OSU's data to validate their model used to optimize gear teeth profile modification (Faggioni et al, 2011). Guilbault et al used the OSU data to validate their two-degree-of-freedom model used to investigate methods for calculating nonlinear damping (Guilbault et al, 2012).

Noting that the 1996 OSU has been used often is not to imply that institution has not produced any more data. In 2013 a paper by Hotait and Kahraman, the latter of OSU, presents more recent data to further study the relationship between DTE and dynamic stress factor in spur gears (Hotait and Kahraman, 2013). Numerous other OSU gearbox experiments have been conducted and published, including dissertations by (Liu, 2007) and (He, 2008). In 2004 Kubur et al, performed a dynamic analysis on a multi-shaft helical gear transmission, but used a twelve-degree-of-freedom single shaft model for experimental validation, while the multi-shaft model was used to compare key gearbox parameters such as secondary shaft length, shaft angle, gear hand configuration and bearing stiffness coefficients (Kubur et al, 2004). In 2007 Tamminana et al of OSU used their testbed to generate new data and study dynamic factors, as previously mentioned.

There exist other gear analyses and DGM studies that experimentally validate their models which rely on comparisons other than the jump phenomenon. These include work done in the early and mid-90's via NASA research grants by Oswald, Zakrajesek and Choy et al, who worked toward improving helicopter and tank transmission reliability (Lin et al, 1994; Choy et al, 1993). Baud and Velex investigated static and dynamic tooth loading of spur and helical gear systems using a finite element model with

experimental validation in 2002 that used strain gauges at the tooth fillet to compare stress and strain (Baud and Velex, 2002). Sawalhi and Randall, the latter being a significant contributor to the study of gear dynamics and vibration, wrote a two part paper in 2008 using a 34-degree-of-freedom model to simulate bearing faults in their experimental gearbox test rig (Sawalhi and Randall, 2008). Endo, Randall and Gosselin used the same gearbox rig in 2009 to compare FEA models of spalls and cracks along with an autoregressive-moving-average (ARMA) method (Endo et al, 2009) which was described by (Wang and Wong, 2002). Omar et al in 2012 used a single-stage experimental gearbox test rig and a nine-degree-of-freedom model (which included gearbox bearing foundation and the gearbox plate where the accelerometer was attached) to investigate different levels of gear tooth crack sizes (Omar et al, 2011). This study is notable as it is amongst the few that used a straight-forward spectrum analysis to compare model and experiment. A spall model and experimental comparison is done by (Ma et al, 2012) with time and spectrum analysis, though with tenuous correlation. A later study (Ma et al, 2015) used less direct means of comparison; instantaneous energy versus time are compared to their twelve-degree-of-freedom model with relatively weak correlation.

1.1.4 Multi-mesh Dynamic Gear Models

Experimental comparisons or validation are notably missing from the multi-shaft DGM papers which follow. Jia, Howard and Wang in 2003 present a 26-DOF DGM which includes friction and geometrical errors to represent a three shaft two-stage gearset. This model includes shaft bending stiffness to represent the flexibility of the translation of the gears on one the shaft relative to the bearings but does not account for gyroscopic motion (Jia et al, 2003). It is noteworthy that while this model is not the basis of the model used in the present research, the DGMs are quite similar. Their DGM was used in a subsequent paper (Jia and Howard, 2006) to compare vibrations due to spalling and crack damage by including faults in the mesh stiffness. There is no experimental result comparison in either study.

Two papers by Al-shyyab and Kahraman in 2005 using a three-DOF model reduced to a two-DOF model of a two-stage gearset solved with HBM and compared to numerical integration results (but not

experimental results) (Al-shyyab and Kahraman, 2005). The results were used to study the influence of mean load, damping ratio, stiffness parameter, meshing phase angle, period-one motions and subharmonic motions. In a subsequent paper in 2007 with similar purpose, the authors use a six-DOF model (Al-shyyab and Kahraman, 2007). In 2013 Yang used the two-DOF two-stage model described by Al-Shyyab and Kahraman to investigate the deterministic and random excitations under different loads using statistic linearization techniques and concluded that heavy load caused linear behavior while a light load caused nonlinear behavior, based on simulated results (Yang, 2013).

A paper by Walha, Fakhfakh and Haddar in 2012 uses a twelve-DOF model of a two-stage gear system that includes one bearing per shaft, each with x- and y-directions, and four rotational DOFs. The model is formulated using Lagrange and is solved by breaking down the non-linear system in to linear systems. The paper studies the influence of backlash in each gear pair but does no experimental comparison (Walha et al, 2012).

Referring back to the summary of two-stage DGMs in Table 2 and comparing to the single-stage DGMs summarized in Table 1, one can see there exist opportunities to create and refine multi-stage lumped parameter DGMs and, as stated by (Velex, 2012), an "urgent need for validated models…especially for complex multi-mesh systems."

1.1.5 Dynamic Gear Model Parameters

Varying parameters within a model to see their effect is referred to as a parametric study. When validating a model created from first principles and directly measured parameters (masses, stiffnesses and estimated damping), it is often necessary to perform parametric studies to confirm the degree-of-freedom choice and the lumped parameter strategy. To further complicate the parametric investigation / validation, stiffness and damping parameters are often nonlinear. For example, bearing stiffness is dependent on load, but load varies constantly while solving a DGM, so a reasonable linear approximation/compromise over the range of operation must be made. Somewhat ironically, this parametric investigation, needed to validate a model against experimental data, is also one of the useful traits of a DGM: its parameters can be changed to study the sensitivity to it within the physical unit.

1.1.5.1 Gear Mesh Stiffness Literature

There exist a variety of methods to develop mesh stiffness profiles, most often using finite element analysis (FEA) but also performed using energy methods. There are also proprietary software applications available that will produce gear mesh stiffness profiles, many of which use procedures described in ISO 6336-1:1996. Most of these mesh stiffness routines are only applicable to low contact ratio gear pairs (contact ratios less than 2.0).

Kuang and Yang (1992) developed equations based on FEA to be used to estimate torsional mesh stiffness for a variety of gears. Their routine is specific to 20^{o} pressure angle and requires some interpolation of stiffness constants used in several curved-fit polynomial equations. Addendum modification coefficients are used in the selection of these constants. Like many mesh stiffness papers, they begin with a single tooth stiffness and combine these into pairs and then combine multiple teeth pairs. Their single tooth stiffnesses are shown to be consistently less than those specified by ISO 6336.

Wang and Howard produced a 2004 paper describing a detailed analysis of the torsional stiffness of a pair of involute spur gears in mesh using FEA (Wang and Howard, 2004). This paper also looked at load sharing and contact stress with varied torsional loads. In 2005 the same authors contributed another

detailed paper on high contact ratio spur gear torsional stiffness using numerous FEA models (Wang and Howard, 2005). The same authors in 2006 investigated error in spur gear FEA models due to a variety of meshing and modeling choices (Wang and Howard, 2006). In a conference paper in 2007 and then a follow-on journal article in 2011, Kiekbusch and Howard and describe a common formula for the combined torsional mesh stiffness that include contributions of the gear body, teeth and contact stiffnesses (Kiekbusch and Howard, 2007; Kiekbusch et al, 2011).

Wu, Zuo and Parey in 2008 used an energy method to calculate time-varying mesh stiffness and also model linear tooth root crack growth in a single stage gear system. They used these in a six-DOF model to compare waveform, spectrum, kurtosis, and RMS amplitudes of simulation results for increasing crack level (Wu et al, 2008). Zhou and Zuo et al used the same method again in 2012 with both six-DOF and 16-DOF models to further study this relationship (Zhou and Zuo, 2012). Neither study featured comparison to experimental data.

A comparison of mesh stiffness modeling strategies by (Meagher et al, 2011) shows the sensitivity of a full gear pair modeled with FEA to mesh density, element type, and contact element tolerance. A 2013 paper by del Rincon et al presents a model for the study of gear meshing stiffness breaking the deformations down into local and global, noting that global deformations appear to be linear while local deformation, and therefore stiffness, appear to be non-linear and much more dependent on load (del Rincon et al, 2013). A 2014 paper by Wan et al features an "improved time-varying mesh stiffness algorithm" is used in conjunction with a ten-DOF DGM that includes rotor gyroscopic effects to investigate the effect of a modeled tooth root crack (Wan et al, 2014). This paper corrects a perceived flaw in the energy method described in 2008 by Wu et al where the energy from a portion of the tooth above or below the base circle was not consistently added or subtracted from the foundation energy when greater than or less than 42 teeth, respectively. This paper features experimental data but does not make a direct comparison to simulated results.

1.1.5.2 Bearing Stiffness and Influence of Housing

It is critical for dynamic gear models which feature translational degrees-of-freedom to accurately model the behavior of the bearings, especially the stiffness. Rolling element bearings, such as ball and roller bearings, have non-linear stiffness which varyies with load, pre-load and speed. However, most DGMs treat bearing stiffness as linear, selecting a single value so solving the model can be computationally practical.

Literature attempting to quantify ball bearing stiffness using both theoretical relationships and experimental results includes early work by (Palmgren, 1959) and (Jones, 1960). Further work to establish equations relating stiffness and load was published by (Harris, 1966; While, 1979; Gargiulo, 1980; Kramer, 1993). These books and papers agree that the radial stiffness of ball bearings varies by the cube-root with load. The non-linearity and complexity of bearing behavior were further investigated and a new matrix model developed by (Lim and Singh, 1990). Experimental and theoretical comparisons have been performed by (Dietl et al, 2000; Mourad et al, 2008; Ali and Garcia, 2010). Dietl and Ali pay particular attention to rolling-element bearing damping in their experiments and analysis. Guo and Parker in 2012 use FEA and a contact mechanic model to investigate the behavior of rolling-element bearings (Guo and Parker, 2012). Guo et al used this bearing model in 2014 to extend the investigation into the complete gear-bearing-housing vibration system for both vibration and acoustics (Guo et al, 2014). The gearbox housing plays an important role in the transmission of gear vibration to the accelerometers and some previous work performed to analytically and experimentally investigate the behavior of gearbox housing was performed by (Randall and Kelly, 1990; Choy et al, 1993).

1.1.5.3 Dynamic Gear Model Damping

Damping is an essential part of a DGM, but, similar to bearing stiffness it is non-linear in nature yet must be treated linearly and a single value estimated for model computational efficiency. Damping literature specific to gearbox systems is relatively sparse. The most basic method for estimating damping is to perform a hammer test, take the log decrement of the time history and calculate a damping ratio.

While this simple damping is only valid for the first/fundamental vibration mode, a similar procedure as described was followed by (Kraus et al, 1987) when investigating stiffness and damping by modal analysis of bearings. Dietl et al also investigated bearing damping in 2000 but in addition to the "classical" experimental approach demonstrated a new approach that does not use an external excitation (hammer or shaker) is employed that can identify damping for individual modes (Dietl et al, 2000). Guilbault et al in 2012 used a two-DOF DGM and OSU's 1996 non-linear jump phenomenon data to parametrically determine damping (Guilbault et al, 2012).

1.1.6 Gear Fault Modeling

Gear faults may be localized at individual teeth or distributed such as wear, eccentricity or geometric and manufacturer errors. Numerous authors have contributed to the development of localized gear fault models. Note that several papers discussed here regarding gear faults have already been cited in above discussions on mesh stiffness techniques and experimental validation.

Wear in gears is a necessary part of the machinery breaking-in process and initially will improve the gearbox vibration if performed with care. Eventually gear wear becomes a faulty condition that may cause excessive vibration. Gear wear has been simulated to show the predicted tooth face change in depth by (Flodin and Andersson, 1997), and its effect on the vibration spectrum simulated by (Kuang and Lin, 2001). Yesilyurt et al measured gear tooth stiffness reduction due to wear using modal analysis with experimental testbed and accelerated wear rate. This study concluded that the increases in vibration were linked more to the changed teeth profile shapes than the loss of teeth stiffness (Yesilyurt et al, 2003). Ding and Kahraman (Ding and Kahraman, 2007) also investigated changes to spur gear dynamics due to surface wear using a single-DOF DGM and a quasi-static wear model proposed by (Bajpai et al, 2003) which is based on the general wear model by (Archard, 1953).

Individual tooth faults, the focus of this paper, include tooth cracks, tooth face spalls, chipped teeth, and missing teeth. A tooth crack model was developed and demonstrated by Howard et al in 2001 first using FEA and then a modified stiffness profile in a DGM. This same technique has been employed by a

variety of researchers including (Wu, et al, 2008; Chaari, et al, 2009; Tian, et al, S. 2012; Zhou, et al, 2012; Wan, et al, 2014; Ma, et al, 2015; Guilbault, et al, 2015). Many of these papers investigated tooth crack severity and propagation. Papers that have investigated and compared different fault models include (Chaari, et al, 2008) which looked at tooth spalls, chipped teeth and missing teeth and (Jia and Howard, 2006) and (Endo, et al, 2009) which also described both tooth root cracks and tooth spalls. Research of gear fault models is ongoing and one of the most common applications of DGMs.

1.2 Gearbox Signal Processing for Condition Monitoring

Since the first rotating and oscillating machines were created, vibration has been used to evaluate the condition of machines. Features indicating the condition of a machine are disruptions to normal vibration patterns. Before the advent of complicated signal processing devices, it was quite common for an auto mechanic to place the tip of a large screw-driver onto an operating engine's block, place the handle to his ear, and listen for irregular vibration sounds to detect faults. This same principle is still applied, only with much more complex techniques to sift through the noise and variation of vibration to identify features indicating faults. Condition monitoring of rotating machinery has historically been performed by recording vibration data, processing it in some manner and comparing the results to an established healthy versus faulty threshold.

1.2.1 Gearbox Signal Processing and Condition Monitoring Literature Reviews

The state-of-the art of gearbox signal processing and condition monitoring has been the subject of many literature reviews. (Akerblom, 2001) performed a literature survey of research into transmission error, dynamic gear modeling and the measurement of gear noise and vibration. (Wang, 2003) described emerging gear fault detection techniques, categorizing the three most promising as auto-regressive (AR) model-based, wavelet analysis, and resonance demodulation schemes and selecting AR model-based as having the most potential as an automated diagnostic tool. (Randall, 2004), previously mentioned for his considerable contributions to gear vibration research, published a two part paper describing the state-of-the-art in rotating machinery condition monitoring and including case histories, although wavelet analysis was notably absent from the discussion. (Jardine et al, 2006) wrote a review of condition-based maintenance programs for diagnostics and prognostics, breaking them down into data acquisition, data processing and maintenance decision-making, and concluding that on-line approaches, among others, should be researched for the next generation of diagnostic and prognostic systems. (Heng et al, 2009) described the state-of-the-art in rotating machinery prognostics, breaking down the approaches into physics-based models and data-driven models, and noting that amongst the challenges inherent are the

changing operating conditions of machinery. (Sikorska et al, 2011) performed a thorough review of prognostic models for estimating remaining useful life, emphasizing data-driven models and the complexity of selecting from the wide variety of techniques most suited for particular applications. (Ahmadzadeh and Lundberg, 2014) reviewed remaining useful life estimation, breaking down the approaches into data-driven, model-based, experience-based, knowledge-based and hybrid-based, and concluding that when data is scarce the physics-based approach is advisable. Many of the literature reviews discussed here are not entirely gearbox specific. This includes (Lee et al, 2014) who presented a review of the methodologies and applications of prognostics and health management for rotary machinery systems (including bearings, gears, shafts, pumps and alternators) with a comprehensive list of algorithms, description of visualization tools and description of four industrial case studies. (Kan et al, 2015) reviewed prognostic techniques for non-stationary and non-linear rotating systems emphasizing data-driven statistical and artificial intelligence techniques, noting that all require relatively large amounts of historical data. The conclusions drawn from these reviews are that gearbox condition monitoring is of enormous interest, vast research has already performed and continues, the problem is highly complex and is not yet solved.

1.2.2 Gearbox Vibration Feature Extraction

Vibration data from machines is processed and analyzed for fault features in the time-domain, frequency domain, and time-frequency domain. Since vibration data contains random noise, identifying features indicating faults is quite challenging. A wide variety of analysis techniques and statistical methods have been developed to extract fault features. Examples include the work performed through NASA (Zakrajsek et al, 1993), (Choy et al, 1994) on helicopter transmission gears, developing a list of vibration features based on statistical parameters/metrics. The NASA parameters/metrics are summarized below with brief descriptions of those with alpha-numeric designations.

- Time-domain feature parameters
  - Mean
  - Standard Deviation
  - Root Mean Square
  - Peak
  - Skewness
  - Kurtosis
  - Crest Factor
  - Clearance Factor
  - Shape Factor
  - Impulse Factor
- Specially developed gear damage detection feature parameters
  - FM0 – Based on maximum peak-to-peak time and sum of harmonic amplitudes
  - FM4 – Based on kurtosis of the difference signal for each time record
  - FM4* - Based on tracking progression of FM4 over time records
  - MA6 – Similar to FM4 but with different exponents
  - M6A* - Based on MA6 but separating normal from faulty records
  - NA4 – Based on the residual signal of a time record
  - NA4* - An enhancement of NA4
  - NB4 – Envelope of bandpass filtered signal, indicating localized damage
  - NB4* - Based on NB4 but tracking damage progression
  - ER – (Energy Ratio) Based on shaft and meshing frequencies and harmonics and first-order sidebands
  - EOP – (Energy Operator) Based on kurtosis of the neighboring point comparisons
- Frequency-domain feature parameters
  - MF – Mean frequency
  - FC – Frequency center
  - RMSF – Root mean square of frequency
  - STDF – Standard deviation of frequency

The NASA feature parameters/metrics have been reviewed and summarized by (Samual and Pines, 2005) and (Sait and Sharef-Eldeen, 2012), who provide more detailed description of each in their work. It is notable that these parameters were developed for use on helicopter transmissions which are planetary gears, though some researchers have used them on single-stage and two-stage test gears. Examples of the NASA features applied include: (Li and Limmer, 2000) who used cracked and worn single-stage test gears and compared the NASA indices with an auto-regression model to track fault severity; (Mosher et al, 2002) who used real flight data to evaluate six of the metrics; (Lei and Zuo, 2009), (Feng et al, 2010) and (Lei et al, 2010) who demonstrated methods designed to combine the NASA indices on a two-stage

test rig with different types and levels of gear faults. These metrics require considerable historical data and are equipment specific so that fault identification may require previous faults to have occurred.

Non-statistical vibration evaluation is most often performed using the frequency domain, specifically the Fast Fourier Transform (FFT) applied to accelerometer data. The results of FFT are a spectrum which is usually analyzed with empirical comparisons between new and baseline frequency plots (Randall, 1987). When interpreting a spectrum plot, frequencies provide information about the sources of the vibration while amplitudes describe the severity. Additionally, harmonics of the frequencies and side-bands around them provide information about faults. A common method to analyze the repetition of harmonics and sidebands is to apply a second FFT to the spectrum resulting in a cepstrum analysis (Randall, 1982). Cepstrum analysis quantifies the reoccurrence of harmonics and side-bands and helps separate the effects of the source and transmission path effect on the spectrum (Randall, 1984).

1.2.3 Wavelets and the Harmonic Wavelet Transform

Condition monitoring is relatively straightforward when machinery operates at a constant rotational speed, as the frequency spectrum can be easily compared over time to identify changes that might indicate faults. However, when machinery's operating speed varies, the classical spectral analysis becomes less effective. FFT and other frequency-domain techniques are not well suited for analyzing non-stationary signals such as machinery with changing speeds (Peng and Chu, 2004). This complication can be overcome by remaining in the time-domain or by applying time-frequency techniques (Jardine et al, 2006; Lee et al, 2014; Kan et al, 2015). Time-frequency domain analysis reveals the waveform energy distribution across both time and frequency, and can be used to identify transient events as well as fault patterns. Examples of time-frequency distribution techniques are the short-time Fourier Transform (STFT), Wigner–Ville distribution (WVD) and wavelet transforms (WT). The STFT segments a signal into discrete time windows to find the frequency content in that window, but window size limits the resolution, making STFT only effective for analysis on slowly changing non-stationary signals (Jardine et al, 2006). While WVD does not segment time as STFT, it is susceptible to interference between "cross

terms" that can cause misleading results (Peng and Chu, 2004). WT can overcome the shortcomings of STFT and WVD in the time-frequency analysis.

Wavelets are short duration waves used to decompose a waveform via convolution, similar to performing the FFT with sine and cosine waves, except WT allows localized frequency information to be obtained specific to the time (or location) of occurrence. WT is used in numerous signal processing applications including non-stationary vibration signals (Newland, 1994) and has been established as an alternative to other analysis methods when speed changes are an issue since it captures both time and frequency information (Wang and McFadden, 1996).

The underlying wavelet function is dubbed the "mother wavelet," and there exist many kinds which have been assigned names based on their creator, some tribute, their origin or their shape. Popular wavelets include Daubechies, Meyer, Morlet, Harmonic and Mexican Hat (Newland, 1996). The Harmonic Wavelet Transform (HWT) is used in this research. Machine condition monitoring applications of WT were reviewed by (Peng and Chu, 2004) including time-frequency analysis, fault feature extraction, singularity detection, signal denoising, signal compression, and system parameter identification. A decade later, a thorough literature and application review of WT was performed by (Yan et al, 2014) which demonstrated the proliferation of WT uses for fault diagnosis of rotary machines.

Newland introduced HWT in 1993 (Newland, 1993), and it has shown promise in identifying faults in stationary and non-stationary gear vibration signals (Inoue and Sueoka, 2008; Lu et al, 2012). The resolution of time and frequency is always a compromise in time-frequency analyses due to the uncertainty principle, so selecting the correct balance, or "partition," is an important consideration. Newland's initial HWT was limited to octave frequency resolution but he later demonstrated freedom to select any frequency interval (Newland, 1994). An adaptive version of HWT was described by (Liu, 2003) which sought to optimize the partition by minimizing entropy. The adaptive HWT was used by (Lu et al, 2012) to identify faulty gears in the same two-stage test rig used in the current research. An approach introduced by (Yan and Gao, 2005) used a Discrete Harmonic Wavelet Packet Transform (DWPT) to diagnose bearing faults in a test bed. The same authors also used HWT as a filter to denoise

vibration signals and identify inner and outer bearing raceway defects in experimental data. A modified HWT was used by (Smallwood, 2011) to characterize a variety of non-stationary signals including mechanical shock.

1.2.4 Gearbox Hybrid Condition Monitoring Approaches

Condition monitoring strategies are often either data-driven or model-based. The distinction is often referred to as "black-box" versus "white-box." Data-driven methods are referred to as "black-box" since they process signals without regard to the underlying physical meaning and therefore what transpires between the input and output might be considered more mysterious. The "white-box" approaches use first-principle physics to describe the system which, in general, does not completely reconcile with real-world behavior. Since both strategies have their weaknesses, merging them is desirable and considered "gray-box" or hybrid approaches. Hybrid approaches are mentioned often in as a third category along with data-driven and model based approaches in literature reviews of condition monitoring methods, but few examples of hybrid gearbox diagnosis and prognosis are demonstrated.

In a non-gearbox-specific paper, (Park and Zak, 2003) describe gray-box approaches in terms of deterministic white-box and stochastic black-box with comparisons in terms of residuals which can be modeled via auto-regression or nonlinear neural networks, seeking anomalies to indicate faults in the system. They use a gas turbine shaft speed model as an example application. In several papers a "differential diagnosis" technique has been described by (Endo et al, 2004; Endo et al, 2009; Hiroaki and Nader, 2012) which uses DGMs, fault models, and AR filtered data to find residuals for gear cracks and spalls, missing gear teeth and bearing faults. This technique is not referred to as a hybrid approach by the authors but does combine modeling and data processing to diagnose faults, providing evidence of the feasibility of merging techniques. (Cheng et al, 2011) estimate pitting damage levels in planetary gears using models and "grey relational analysis" which is used to analyze systems where only partial information is available, such as the pitting fault model used by the authors. A model-based gear fault diagnosis method was proposed by (Leem and Choi, 2013) which uses a DGM, TSA, difference in model

and measured features, and regression model of FEA gear crack stiffness changes. This paper describes the proposed method but does not demonstrate it. Hybrid condition monitoring approaches are shown to be feasible and desirable in the literature.

1.3 Literature Conclusion

It is clear from the literature that gearbox condition monitoring has been and remains an important topic of research. The wide variety and continued development of condition monitoring approaches, including data-driven and model-based, demonstrates the difficulty of achieving a reliable and universal diagnostic and prognostic method. Combining modeling and signal processing is often suggested or included in the discussion of condition monitoring strategies, but seldom realized. The inevitable conclusion is there exists both need and opportunity for creating a condition monitoring approach that merges data processing and modeling.

Chapter 2 – Experimental Setup and Parameter Investigations

2.1 Experimental Setup Description

The testbed used in this research is comprised of a 3-HP motor driving a constant-torque magnetic brake load through a two-stage gearbox (SpectraQuest, 2009), shown in Figure 1, owned by The University of Connecticut's Structural Dynamics and Systems Lab (SDSL). The testbed is equipped with a variable speed controller and outfitted with multiple accelerometers and a digital tachometer.

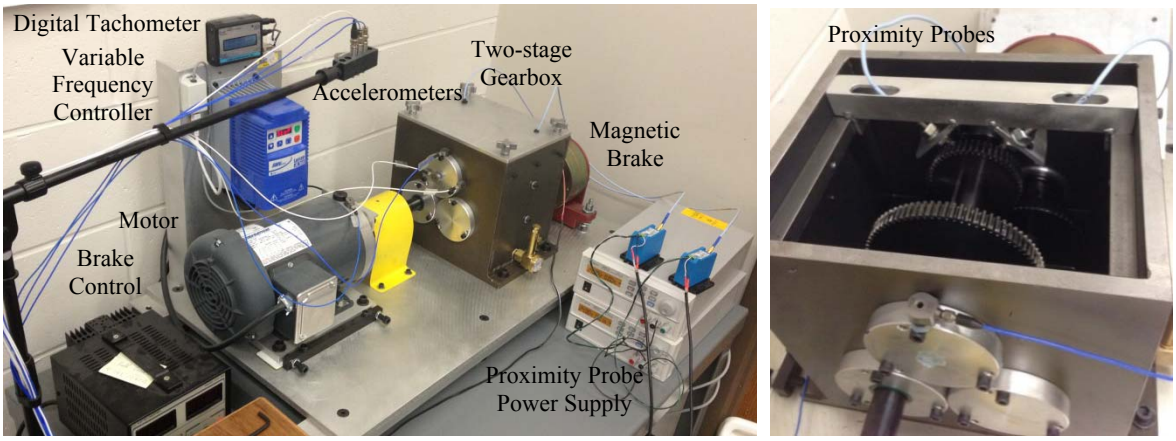

Figure 1. UConn SDSL Gearbox Test Bed

The SDSL gear-box transmission is made up of three 32-tooth pinions on the input shaft, one of which drives an 80-tooth gear on the intermediate shaft connected to a 48-tooth pinion driving a 64-tooth gear on the output shaft. As shown in Figure 2, the 80-tooth gear can be manually slid along the intermediate shaft to align with any of the three 32-tooth pinions. This arrangement allows one healthy and two faulty pinions to be investigated without complete removal of the shaft with each trial.

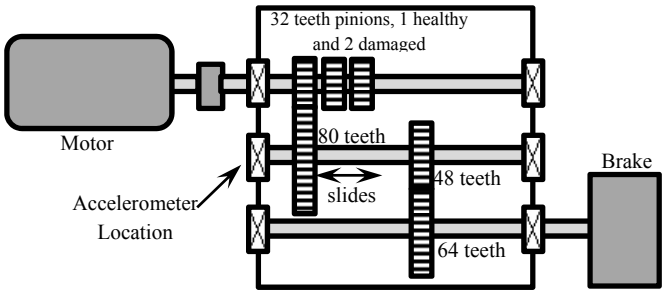

Figure 2. Gearbox Test Bed Arrangement

Speed control is achieved using a Lenze ACTech SMVector variable frequency drive which controls motor speed as directed by a computer program connected via USB. The speed profile used in this research is shown in Figure 3a, and the computer program interface in Figure 3b. The digital tachometer measures the rate at which a raised portion on the shaft interrupts a magnetic field. The pulses of this interruption are sent to the data acquisition system via a BNC cable as well as translated into revolutions per minute on the local display.

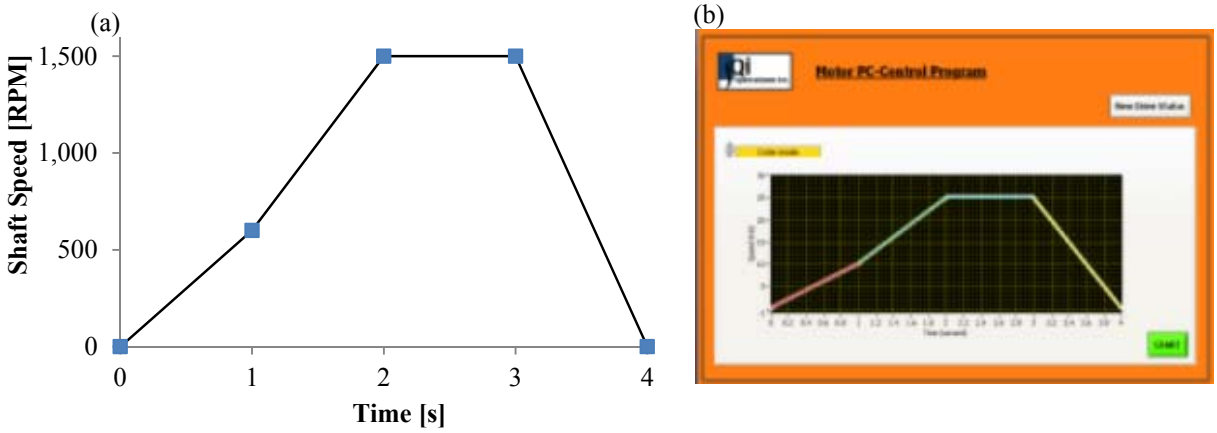

Figure 3. Speed-Time Profile Input

The Placid Industries B220 magnetic particle brake (placidindustries.com) maintains a constant torque when a set input current energizes a magnetic field. The torque is proportional to the power supply current and is constant regardless of shaft speed, adjustable from 4 to 220 in-lbs (0.45-24.9 Nm) .

Acceleration data is collected from accelerometers (Model 355B03, PCB Piezotronics Inc., Depew, NY) positioned on the intermediate shaft bearing hub in vertical, horizontal and axial orientations for data collection and on the motor for data collection triggering. Two Bentley Nevada 3300 8mm proximity probes are attached to the inside of the gearbox via a custom-made bracket, positioned 90^{o} apart, and held at a small gap away from the hub of the second stage pinion. These probes are connected through Bentley Nevada XL proximitor boxes to the data acquisition system. The acceleration, proximity and tachometer data are converted to digital signals at 20 kHz and recorded through a dSPACE data acquisition system (DS1006 processor board, dSPACE Inc., Wixom, MI) with a high speed ADC board (DS2004).

The gearbox internal arrangement is shown in Figure 4 in plan, section and exploded isometric views. The motor is connected to the input shaft by a Lovejoy L-type coupling with Buna N rubber spider. The input shaft is supported by two Rexnord MB ER16K ball bearings held in place by machined aluminum hubs which axially preload the bearings using two Bellville springs on each side. The intermediate and output shafts have similar bearing arrangements. Collars on the shafts are fastened into set positions so reassembly of the shafts will result in approximately the same Bellville spring compression and therefore preload. The input shaft can fit three 32-teeth first-stage pinions to minimize shaft removal and reinstallation when different faulty gears are to be tested. The 80-teeth first-stage gear can be slid along the intermediate shaft when its set screw is loosened. The three shafts are arranged in an equilateral triangle configuration.

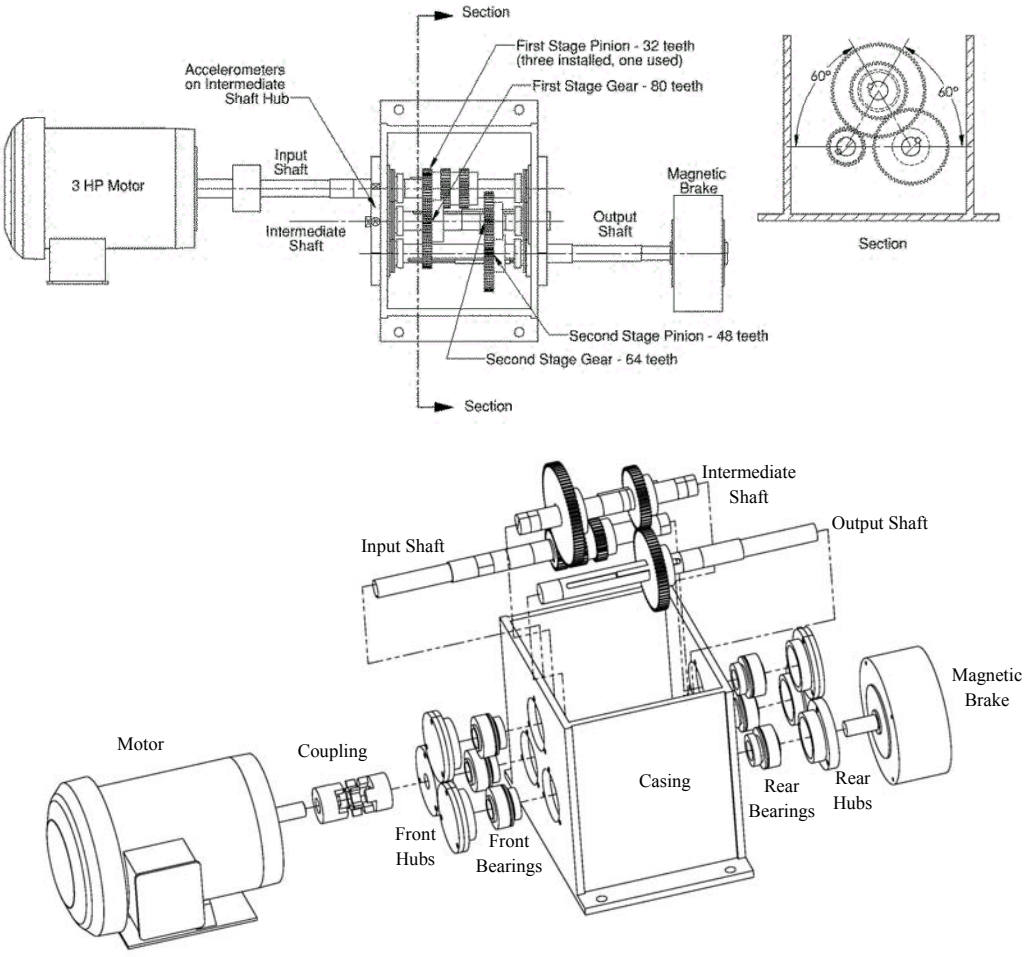

Figure 4. Gearbox Testbed Internal Arrangement

The gears used in the test bed have a 14.5° pressure angle and 16 teeth/inch diametral pitch (1.59 mm module). The contact ratio, the average quantity of teeth engaged during a mesh cycle, is calculated from equation (1) and is a function of pressure angle, diametral pitch and number of teeth (Shigley et al, 2015). The contact ratios for the 32/80 and 48/64 gear pairs are 2.12 and 2.16, respectively. These are considered high contact ratios since at least two gear teeth pairs are in contact at any given instant with three teeth pairs in contact periodically. The majority of published gearbox experimental test data comes from testbeds with contact ratios below 2. Table 1 summarizes gear parameters from the test beds used in various well-known studies. These include the often cited experimental data from the work of Munro in 1962, Kubo et al in 1972 and Kahraman and Blankenship of OSU in 1996. Other experimental gearbox research efforts using single-stage or two-stage spur gear test stands include work within NASA by Oswald, et al and Choy, et al in the early 1990s, (Baud and Velex, 2002), (Endo et al,2009), (Omar et al, 2011), (Ruiz et al, 2013) and (Ma, 2015).

$$m_c = \left(\sqrt{\left(\frac{d_p}{2}+a\right)^2-\left(\frac{d_p}{2}\cos\phi\right)^2}+\sqrt{\left(\frac{d_g}{2}+a\right)^2-\left(\frac{d_g}{2}\cos\phi\right)^2}-\left(\frac{d_p}{2}+\frac{d_g}{2}\right)\sin\phi\right)/(p_c\cos\phi) \qquad (1)$$

Where: p_c = diametral pitch, $p_c = 1/module$
N_p = number of pinion teeth
d_p = pitch diameter of pinion, $d_p = N_p/p_c$
ϕ = pressure angle
a = addendum, $a = 1/p_c = module$
N_g = number of gear teeth
d_g = pitch diameter of gear, $d_g = N_g/p_c$

Table 3. Comparison of Various Experimental Gearbox Test Equipment

	Pressure Angle [°]	Pinion Teeth	Gear Teeth	Module [mm]	Contact Ratio
Munro	21.5	32	32	6.35	1.60
Kubo	21.5	25	25	7	1.56
NASA (Oswald/Choy)	20	28	28	3.18	1.64
OSU (Blankenship)	20	50	50	3	1.76
Baud	20	26	157	4	1.76
UNSW (Endo)	20	32	32	3.08	1.67
Omar	14.5	15	15	1.59	1.67
Ma	20	55	75	2	1.79
Ruiz 1st Stage	20	18	26	2.5	1.57
Ruiz 2nd Stage	20	20	35	2	1.62
UConn SSDL 1st Stage	14.5	32	80	1.59	2.12
UConn SSDL 2nd Stage	14.5	48	64	1.59	2.16

The high contact ratios of the testbed is a consequence of the 14.5° pressure angle, which is a relatively rare and even described as obsolete by (Shigley, et al, 2015). Figure 5 presents the line-of-action and pressure angle for both stages and demonstrates the three-teeth-pair and two-teeth-pair engagement. High contact ratio gear pairs are typically less sensitive to individual faults, as adjacent undamaged teeth can share the additional load not carried by the faulty tooth. Using high contact ratio teeth pairs for this investigation increases the fault finding difficulty, making the demonstration of model sensitivity to fault type and severity more significant.

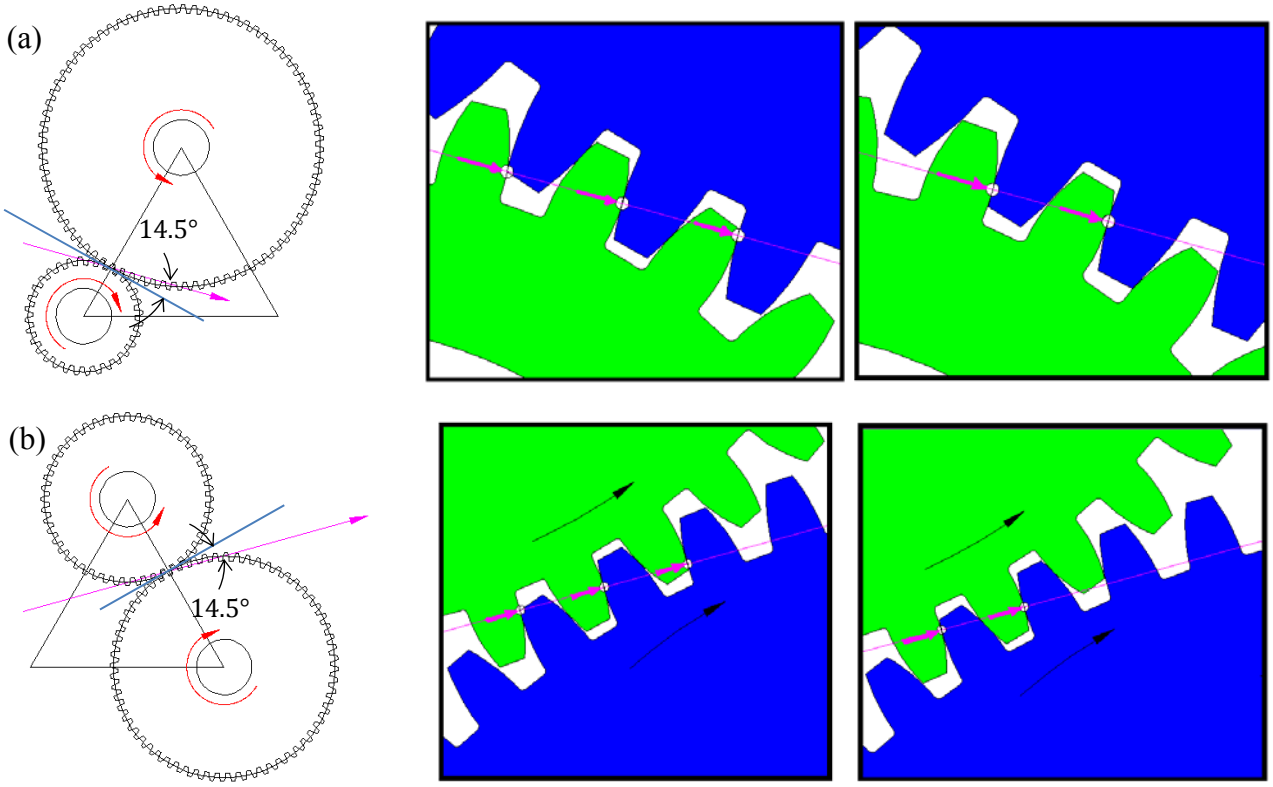

Figure 5. Testbed pinion and gear mesh arrangement and three- and two-teeth pair engagement for (a) first-stage and (b) second-stage.

2.2 Parametric Development

Dynamic gear models (DGMs) require stiffness, damping and inertia parameters to be gathered, calculated, measured, or estimated for each component associated with a DOF. Table 2 summarizes the parameter values identified for the gearbox testbed.

Table 4. Parameters Used in Dynamic Gear Model.

Degree of Freedom	Mass			Stiffness			Damping		
	Variable	Value	Units	Variable	Value	Units	Variable	Value	Units
1	I_D	7.51×10^{-3}	kg m^2	k_{t1}	247	N m/rad	c_{t1}	0.0926	N s/rad
2	I_1	3.86×10^{-4}	kg m^2						
3	I_2	2.69×10^{-3}	kg m^2	k_{t2}	39,900	N m/rad	c_{t2}	1.45	N s/rad
4	I_3	4.18×10^{-4}	kg m^2						
5	I_4	1.21×10^{-3}	kg m^2	k_{t3}	12,600	N m/rad	c_{t3}	0.507	N s/rad
6	I_L	6.64×10^{-5}	kg m^2						
7 and 8	m_1	0.743	kg	k	3.50×10^7	N/m	c	831	N s/m
9 and 10	m_2	0.748	kg	k_{b1}	1.83×10^8	N/m	c_{b1}	0	N s/m
11 and 12	m_3	0.643	kg	k	3.50×10^7	N/m	c	831	N s/m
13 and 14	m_4	0.443	kg	k	3.50×10^7	N/m	c	831	N s/m
15 and 16	m_5	1.466	kg	k_{b2a}	2.43×10^8	N/m	c_{b2a}	0	N s/m
17 and 18	m_6	0.550	kg	k_{b2}	1.32×10^8	N/m	c_{b2}	0	N s/m
				k_{b2b}	2.43×10^8	N/m	c_{b2b}	0	N s/m
19 and 20	m_7	0.443	kg	k	3.50×10^7	N/m	c	831	N s/m
21 and 22	m_8	0.651	kg	k	3.50×10^7	N/m	c	831	N s/m
23 and 24	m_9	0.942	kg	k_{b3}	3.49×10^8	N/m	c_{b3}	0	N s/m
25 and 26	m_{10}	0.648	kg	k	3.50×10^7	N/m	c	831	N s/m

Many of these parameters are found from first principles, but others require more in-depth investigations and side-studies. Side-studies include detailed finite-element-analysis (FEA) models, modal hammer response tests of the shafts both in-situ and removed from the testbed with comparisions to FEA modal results. Parameters such as bearing stiffness are non-linear but must be treated as linear in the DGM in order to solve the model efficiently. Consequently, a single stiffness value must be selected to best capture the operating behavior. Various DOF versions of the DGM are run with different parameters to quantify the effect of changes. The natural frequencies of the DGM and testbed are closely compared as part of these investigations. The following subsections give more detail about the sources and methods used to compile the above parameters.

2.2.1. Mass and Inertia

The masses of the shafts and gears were measured directly, while the mass moment of inertias were found from Solidworks models and confirmed with hand calculation estimations. While mass can be measured for most components, "lumping" the mass to a single DOF point of the shafts requires additional consideration. Figure 6 shows the DOF locations on the three shafts. The shaft mass is assumed to be split midway between DOF points, and the masses of the extra gears on the input shaft are allocated mostly to the adjacent gear representing a DOF.

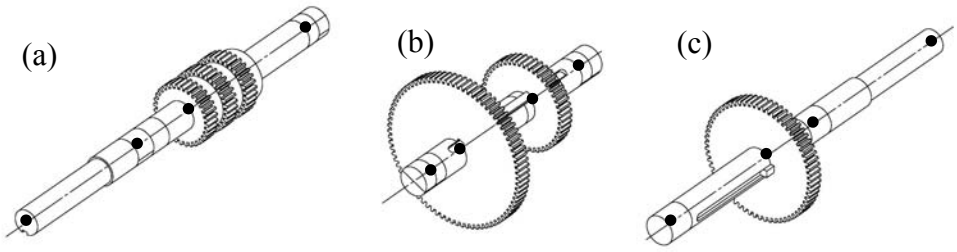

Figure 6. DOF locations for lumping mass for (a) input shaft, (b) intermediate shaft and (c) output shaft.

The mass moments of inertia for the shafts and gears are easily approximated as cylinders and hollow cylinders respectively and confirmed within Solidworks for each solid model and assembly. The mass moment of inertia of the moving parts of the magnetic brake is supplied by the manufacturer (placidindustries.com). The mass moment of inertia of the motor is estimated from equation (2) which is the weight moment of inertia approximation from NEMA MG 1-2014 14.46 (nema.org).

$$Wk^2 = \left[0.02 \cdot 2^{(poles/2)} \cdot HP^{(1.35-0.05 \cdot poles/2)}\right] \quad (2)$$

Where: Wk^2 =weight moment of inertia, $lb \cdot ft^2$
HP = rated motor power, horsepower
$poles$ = number of motor poles

The inertia parameters (mass and mass moment of inertia) for the individual components are summarized in Table 3.

Table 5. Inertia Properties

	Mass	mMoI
Shaft	kg	$kg \cdot m^2$
Input	0.8895	5.990E-05
Intermediate	0.7167	5.225E-05
Output	1.120	7.817E-05
Pinion 1 (32 teeth)	0.2492	9.353E-05
Gear 1 (80 teeth)	1.466	2.658E-03
Pinion 2 (48 teeth)	0.5497	3.833E-04
Gear 2 (64 teeth)	0.94179	1.108E-03
Motor rotor	-	7.507E-03
Brake	-	2.730E-05

2.2.2. Stiffness Parameter Development

Most of the components in the gearbox testbed have linear stiffness estimated from first principle relationships, confirmed or refined using FEA models. The two exceptions are the ball bearings, whose stiffness is dependent on load and speed, as well as the gear meshing stiffness which is dependent on number of teeth in contact and therefore time variant. The following sub-sections describe the methods used for establishing stiffness parameters.

2.2.2.1. Shaft Torsional Stiffness

Most DGMs include the torsional stiffness between rotational DOFs, including the shafts between driver, gears and load. The torsional stiffnesses of the three shafts, shown in Figure 7, are summarized in Table 4. Torsional stiffness is found from FEA since the long keyways influence the results, though these values compare favorably with approximation based on the relationship between torque and angular deflection for standard solid shafts. Note that the location of the first-stage pinion and first-stage gear on their respective shafts will change depending on which pinion is engaged. Different sets of values from those shown in Table 2 are used in the model when appropriate.

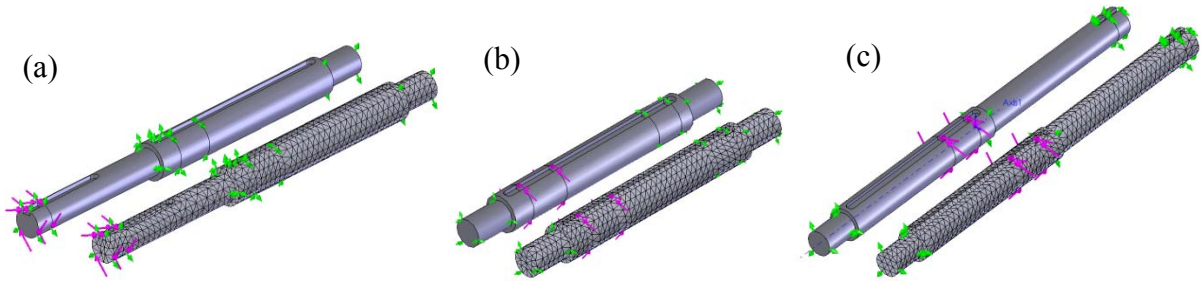

Figure 7. Solid models and meshed FEA models for (a) input shaft, (b) intermediate shaft, and (c) output shaft.

2.2.2.2. Shaft Bending Stiffness

The shaft bending stiffness must be determined for DGMs with DOFs representing bearings at each shaft end. Determining the bending stiffness of the shafts is relatively trivial as they are treated like simply-supported beams for which the load deflection relationship is readily available. A slight complication arises for the intermediate shaft, as it is loaded at two gear locations and a stiffness value is needed to represent the relationship between these points. The intermediate shaft bending stiffnesses are estimated by superimposing the individual local deflections due to a unit load at each location and finding the necessary off diagonal stiffness of a 2x2 matrix that causes the same deflections when unit loads are placed at both locations simultaneously. This relatively crude technique balances the reaction loads and is confirmed using FEA beam element comparisons.

The shafts are assumed to behave as simply supported beams, but since the ball bearings are not entirely flexible with respect to shaft angular deflection, this assumption is explored through in-situ natural frequency tests, described in a later section. The bending stiffnesses are summarized in Table 4. As previously noted, the position of the first-stage pinion and gear along the shaft can change when the gear is slid to any one of the three pinions. This is accounted for in the DGM.

Table 6. Shaft stiffness properties.

	Torsional Stiffness	Bending Stiffness		
Shaft	$N \cdot m/rad$	N/m		
Input	8,200	1.83E8		
Intermediate	39,900	2.43E8	1.32E8	2.43E8
Output	12,600	3.49E8		

2.2.2.3. Coupling Torsional Stiffness

The couple between drive motor and gearbox input shaft is a Lovejoy model L-090 HUB 7/8 KW (lovejoy-inc.com). The coupling, shown in Figure 10, features a Buna N rubber spider which has "high dampening capacity." The stiffness of the coupling is estimated based on the Shore harness, summarized in Table 5. The coupling torsional stiffness acts in series with the input shaft torsional stiffness, combining for a relatively low effective stiffness. The damping ratio used for the combined coupling and shaft is 15% based on (Zorzi and Walton, 1982).

Figure 10. Motor to input shaft coupling, (lovejoy-inc.com).

Table 7. Coupling parameters.

Spider Shore Hardness (Buna N)	80	type A
Equivalent Elastic Modulus	9.35	MPa
Single Leg Linear Stiffness	103	kN/m
Single Leg Torsional Stiffness	42	N-m/rad
Total Spider Torsional Stiffness	252	N-m/rad
Shaft torsional stiffness	11.4	kN-m/rad
Combined Input Shaft and Coupling Stiffness	247	N-m/rad

2.2.2.4. Mesh Stiffness

Gearbox vibration is predominantly caused by the periodic mesh stiffness variation. A variety of methods exist to develop mesh stiffness profiles, most often using finite element analysis (FEA), for example (Howard et al, 2001), but also using energy methods such as (Wan et al, 2014). Kuang and Yang (1992) and Kiekbush et al (2011) both developed equations and procedures based on FEA to estimate torsional mesh stiffness for a variety of gears. In order to modify the mesh pattern to simulate faults, a procedure similar to that described by (Wang and Howard, 2004) is used for this investigation, where the total mesh stiffness is assembled in parts based on the stiffness of individual teeth found from FEA.

The pinions and gears are created as solid models with the face of an individual tooth on each divided into discrete parallel area regions representing points of contact. The solid models are meshed, loaded, constrained, solved and post-processed in Solidworks Simulation FEA. A refined mesh is used around the face and base of the loaded tooth in each gear model. The FEA models are solved with unit loads placed at each region. Figure 11 shows two FEA result examples where the gear teeth are loaded on the topmost region. The average displacements of each region are used to develop the relationship of single tooth stiffness along the line of action.

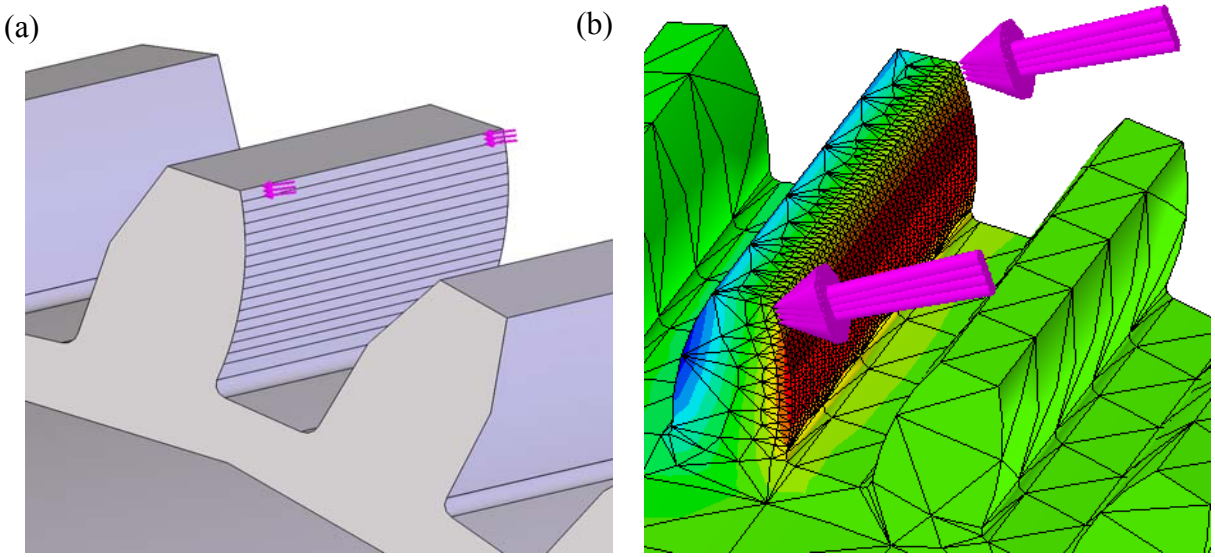

Figure 11. Gear Teeth (a) Solid model and (b) FEA model

The single tooth stiffness for each gear is shown in Figure 12 versus the angle with respect to the initial contact (IC) point. Note that the pinion becomes less stiff as it moves through the mesh cycle, but the gear stiffens due to the location of the contact point moving along the gear face during engagement. Also note that the larger gears are less stiff than the smaller pinions due to the body flexibility.

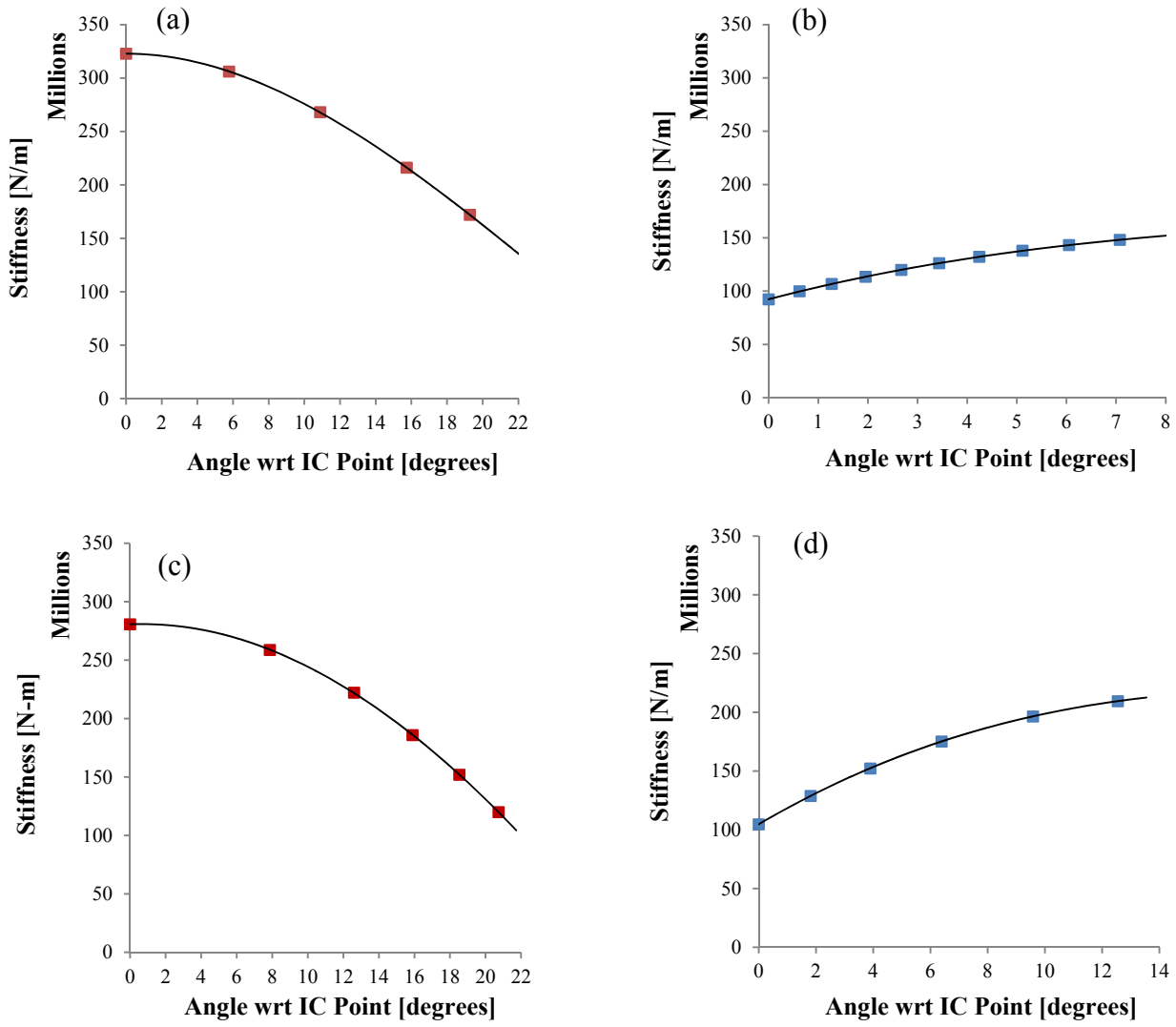

Figure 12. Individual gear teeth stiffness with respect to initial contact (IC) point. (a) 1st stage pinion, (b) 1st stage gear, (c) 2nd stage pinion, and (d) 2nd stage gear.

The individual teeth stiffnesses of Figure 12 are repeated in Figure 13(a) as dashed red lines representing the first stage pinion stiffness, $k_{p,i}$, while the blue dot-dash line represent the first stage gear

stiffness, $k_{g,i}$. Two angular positions, A and B, are shown on Figure 13(a) with points labeled to help describe the stiffness formulation. The combined stiffness of each gear pair, k_i, is given by Equation (3) since the two teeth act as springs in series. Contact stiffness is often included here as it also acts in series, however it is omitted here due to the relative light loading of the physical gearset. The total mesh stiffness is given by Equation (4) treating the teeth pairs as parallel springs.

$$k_i = \frac{k_{p,i} k_{g,i}}{k_{p,i} + k_{g,i}} \tag{3}$$

$$k_m = \sum_i k_i \tag{4}$$

At position A in Figure 13(a) two pairs are in contact, while three pairs touch at position B causing a periodic stiffness increase in the total mesh stiffness. The mesh stiffness for the second stage is shown in Figure 13(b), illustrating a different character to its mesh stiffness pattern due to the nature of the individual teeth stiffness curve.

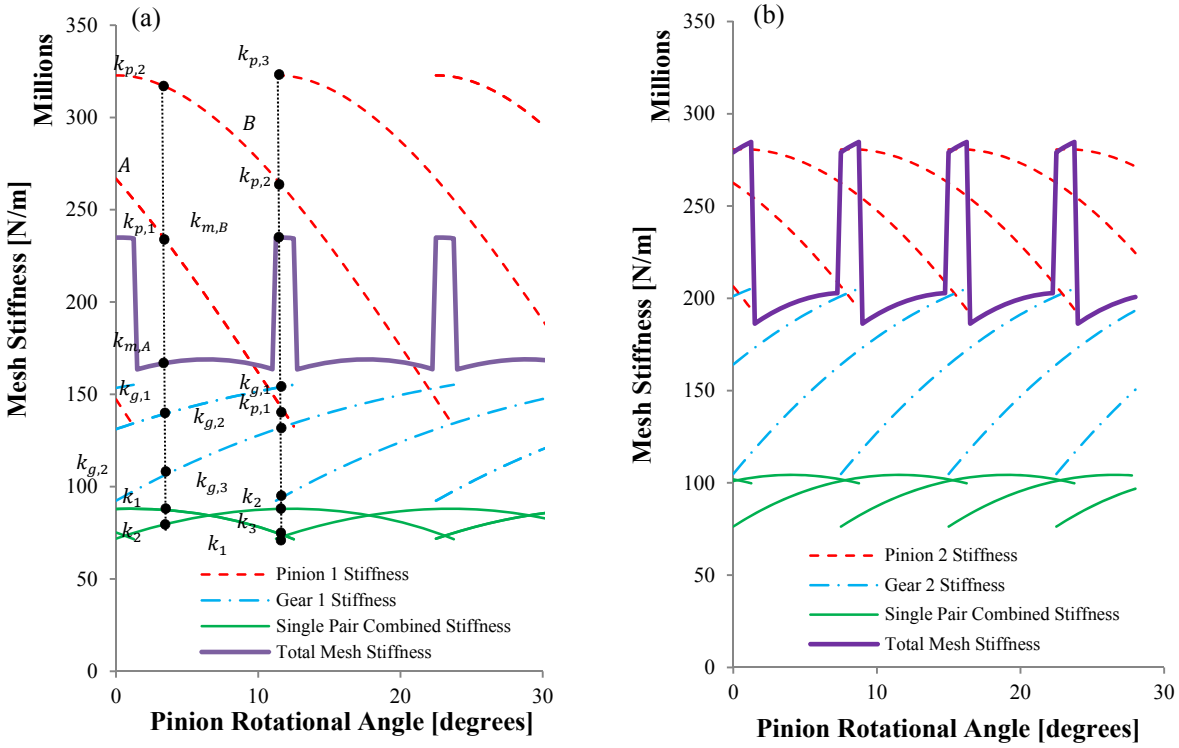

Figure 13. Gear Mesh Stiffness Formulation

The mesh stiffness formulation strategy employed on the first stage gear pair was compared to a variety of alternative methods. A full FEA model of both pinion and gear was created in Solidworks Simulation with some mesh density refinement around the teeth contact area as shown in Figure 14. Contact gap elements were automatically assigned by setting the boundary conditions to "no penetration". The gear was fixed at its bore and the pinion constrained in all directions except rotation about its centerline axis. A unit torque of on 1 Nm was applied about this axis and the model solved and post-processed in polar coordinates for angular displacement about the pinion centerline axis. The angular displacements of the pinion bore were averaged, inverted to obtain torsional stiffness, and multiplied by the base circle radius to obtain mesh stiffness along the line-of-action. The pinion and gear were rotated and the procedure repeated at 1^{o} increments for 20^{o}. Using this methodology, a crude mesh stiffness profile was obtained and plotted in Figure 15 along with the profile obtained by combining individual teeth stiffnesses as well as other mesh stiffness values obtained from literature. It is noted that a relatively course FEA mesh was used and the solid model, teeth profiles while near perfect involutes, showed interference when positioned precisely, suggesting the actual teeth have profile modifications, though none are indicated by the gear supplier.

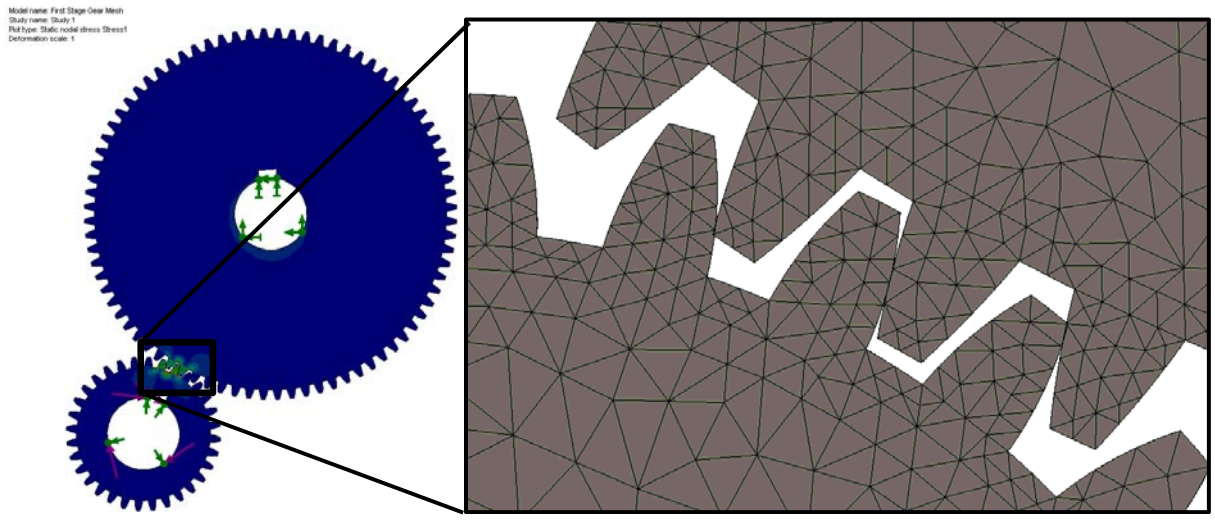

Figure 14. First-Stage Gear Pair FEA Full Model

Other mesh stiffness calculation techniques were performed for comparison. A trial version of a commercially available machine design software package, KissSoft (http://www.kisssoft.ch/), was obtained and used to calculate the mesh stiffness profile. The low and high values for two and three teeth pairs engaged, respectively, are plotted as square waves on Figure 15 with the other mesh stiffness methods. According to the product manual, the internal calculation procedure is based on ISO 6336 and DIN 3990, but calculations using ISO 6336 were performed and included in Figure 15 showing significant differences. Methods described by Kuang and Yang (1992) and Kiekbusch and Howard (2004) were also performed and are represented as square waves in Figure 15. Note the wide range of discrepancies among methods. The conclusion drawn is there remains some uncertainty as to the most accurate method for determining mesh stiffness. While the method for mesh profile generation used in this research has some inherent error, it is sufficiently comparable to other methods as well as particularly useful since it can be easily adapted to model gear faults, as described in a subsequent sub-section.

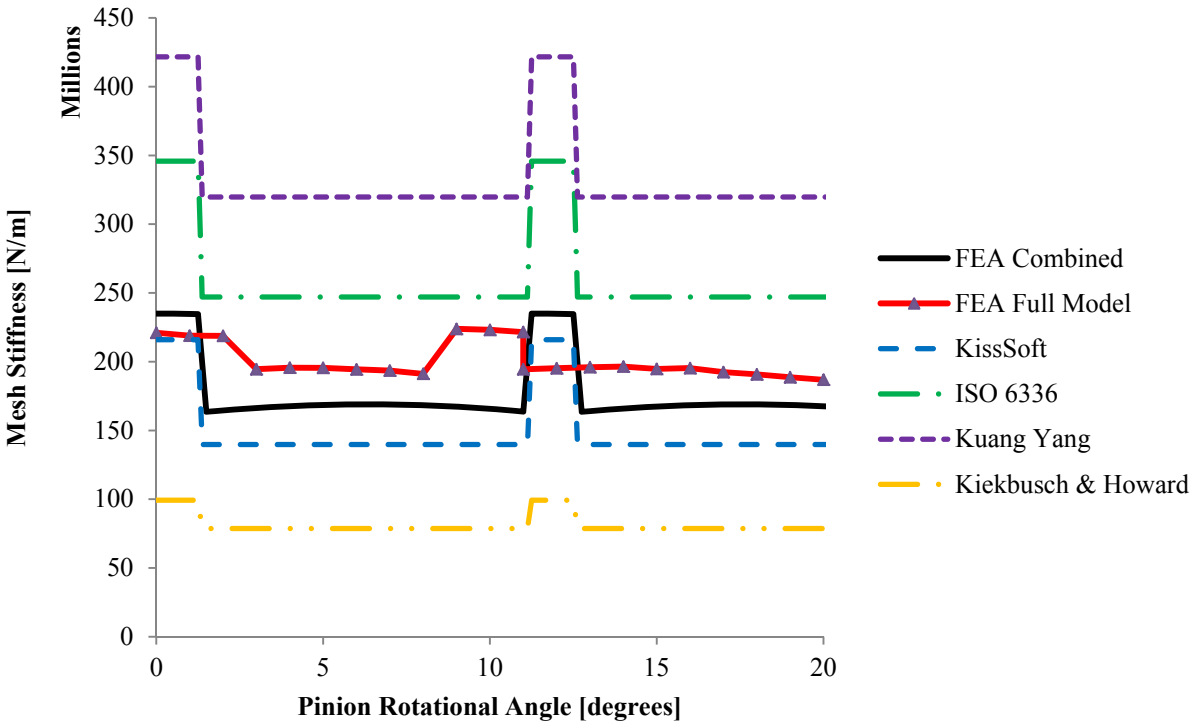

Figure 15. First-Stage Gear Mesh Stiffness Comparison

2.2.2.5. Mesh Stiffness Fault Type Models

One of the benefits of creating a DGM of the gearbox is the flexibility available in solving a wide variety of fault scenarios (Chaari et al, 2008). The most common gear faults are those that effect individual gear teeth, and these can be modeled as changes in the meshing stiffness. Figure 16 shows the solid models used to represent four different localized gear faults: missing tooth, root crack, spall and chipped tooth.

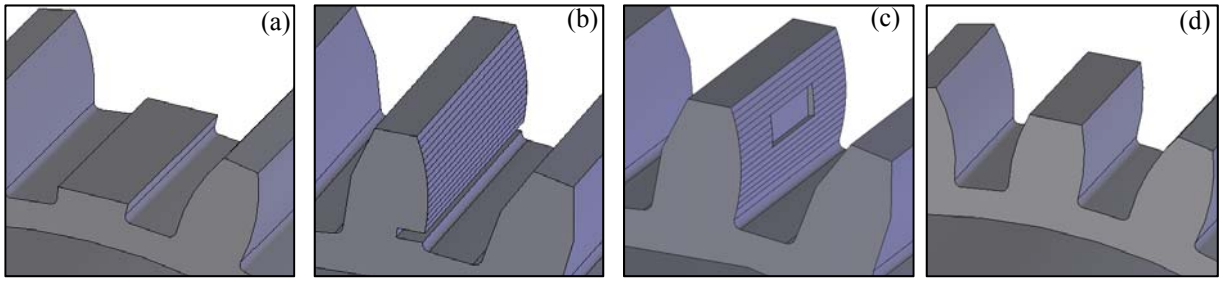

Figure 16. Model representations of (a) missing tooth, (b) root crack, (c) spall and (d) chip.

The FEA model of the pinion is slightly modified so a portion of one tooth is removed and the stiffness developed as previously discussed. Figs. 17-20 show the solid model, difference in single tooth stiffness due to the chip and resulting meshing stiffness function. This stiffness function is approximated within the DGM with linear and quadratic piece-wise changes to the stiffness step function to coincide with the engagement of the damaged tooth.

For the missing tooth, the formulation described above is repeated except the contribution of one pinion tooth is entirely omitted, dropping the mesh stiffness pattern to only one pair of teeth for two periods as seen in Figure 17. The cracked tooth and tooth spall, mesh patterns shown in Figures 18 and 19, respectively, are developed from the stiffness curves of FEA results using the modified solid models. The chipped tooth mesh stiffness pattern seen in Figure 20 is created by stopping short the stiffness contribution of one pinion tooth. These figures help to illustrate the influence and individuality of the local faults on the mesh stiffness patterns and explain why vibration signals can be used to identify faults.

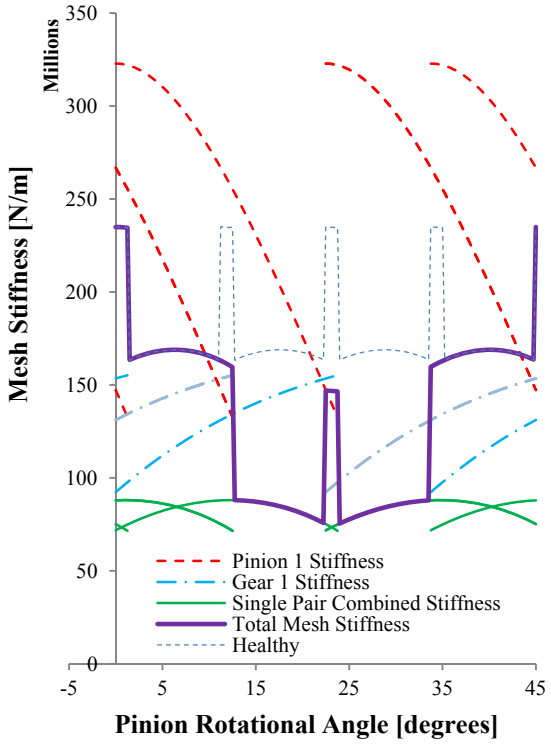

Figure 17. Missing Tooth Mesh Stiffness

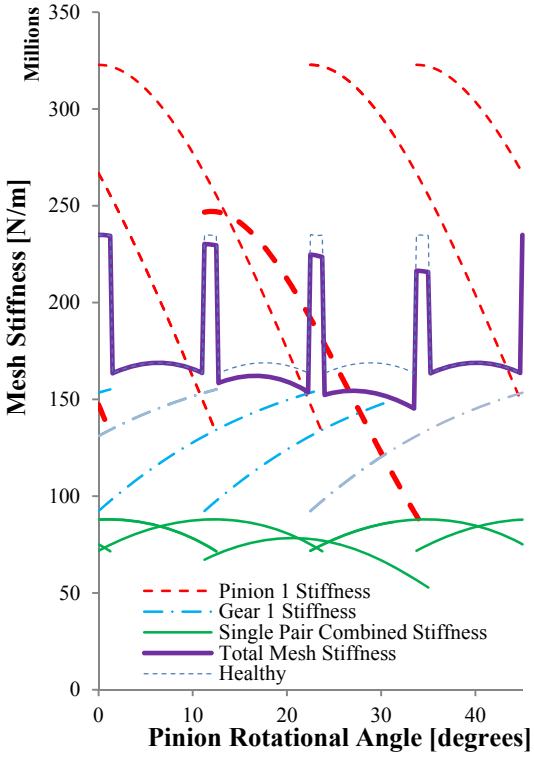

Figure 18. Cracked Tooth Mesh Stiffness

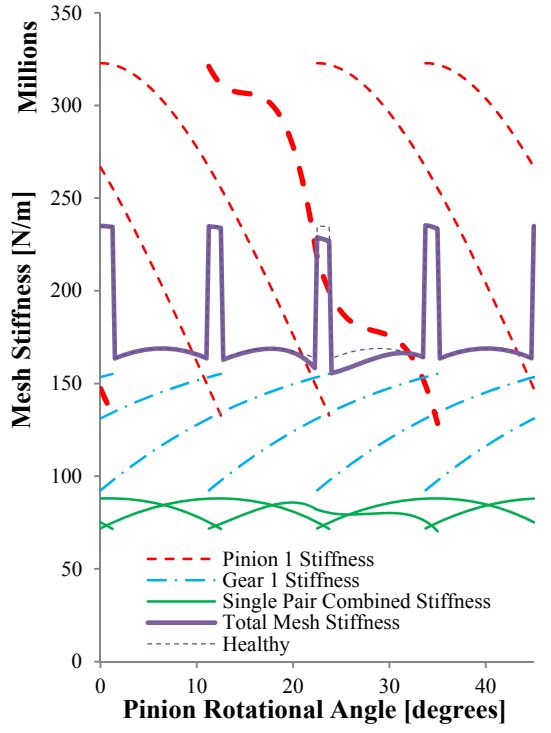

Figure 19. Tooth Spall Mesh Stiffness

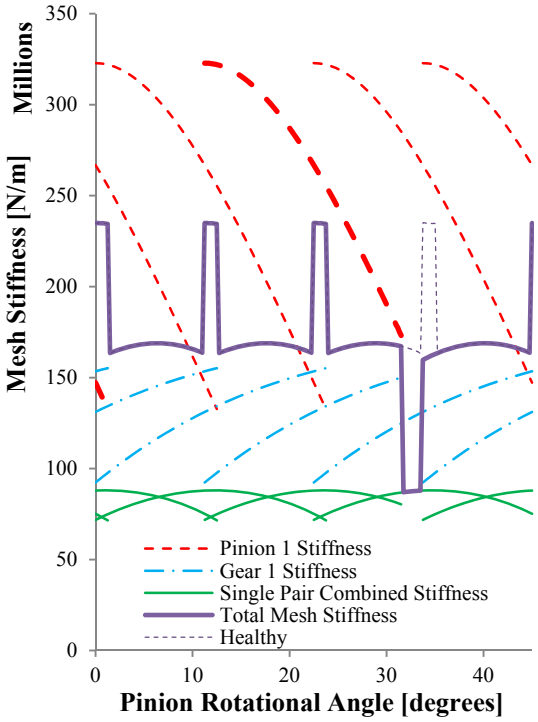

Figure 20. Chipped Tooth Mesh Stiffness

2.2.2.6. Mesh Stiffness Fault Severity Models

To demonstrate the ability of the proposed technique to distinguish the severity of a gear fault, the first-stage pinion is replaced for each test with progressively worse chipped gears. To simulate increasingly larger chips, the tip of a single tooth on each test pinion is filed down by an incrementally larger amount, as represented in Figure 21. The chip sizes are designated as chip one through five; noting that chip five, the largest, is the size used in the fault type comparison. The amount of material removed for chips one through five is 0.15 mm, 0.24 mm, 0.38 mm, 0.48 mm and 0.69 mm, respectively. Figure 22 shows the modeled effect of chip size on the mesh stiffness profile.

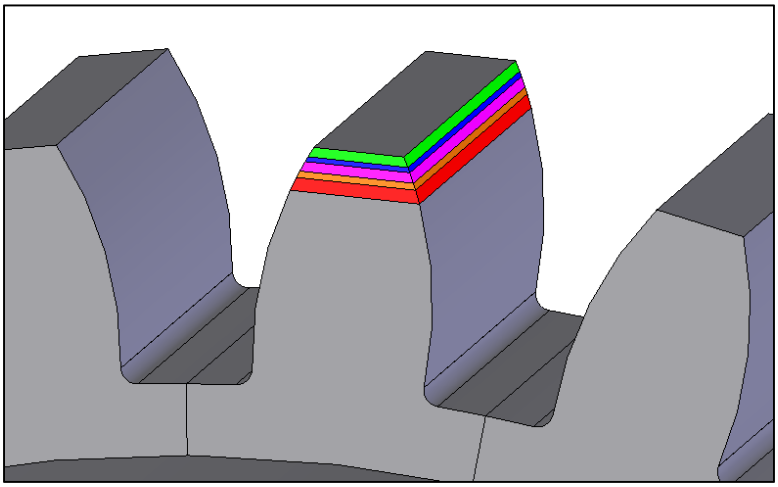

Figure 21. Model representation of chips with increasing size.

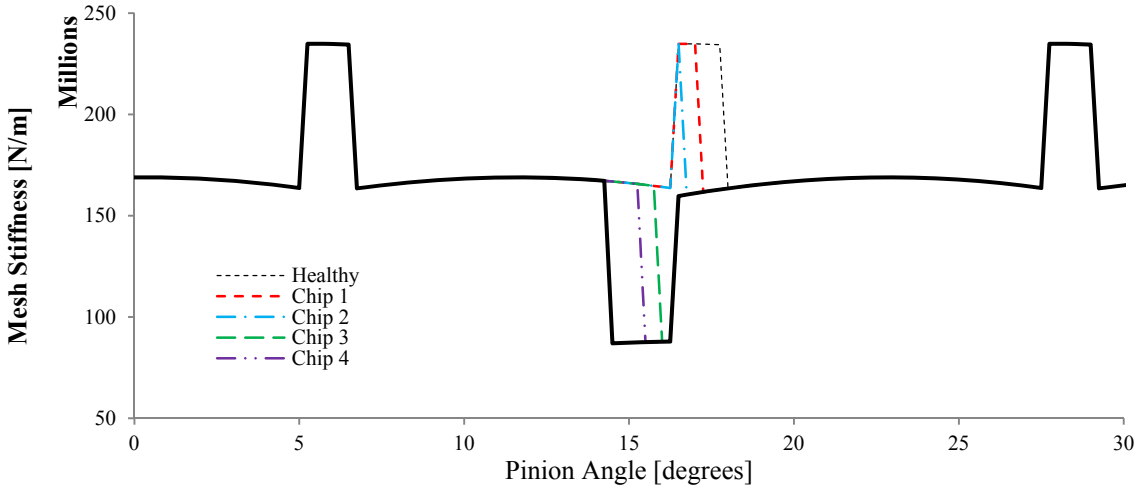

Figure 22. Stiffness profile of first stage gear with increasing chip size.

2.2.2.7. Bearing Stiffness

The gearbox is fitted with Rexnord MB radial ball bearings (rexnord.com), shown in Figure 23. It is necessary to include the bearing stiffness and damping in the DGM to produce representative DOF accelerations that coincide with experimentally obtained accelerometer data. Accurately representing the dynamic behavior of bearings in the DGM is particularly challenging due to their stiffness non-linearity with respect to pre-load, radial load and rotational speed. Many papers have discussed this challenge (Gargiulo,1980; Dietl et al, 2000; Mourad et al, 2008; Guo and Parker, 2012). While modeling of bearing behavior continues to advance, it is most advantageous for solution speed in a DGM to assume linear behavior by using a single value for stiffness. A series of investigations were performed to identify the most accurate single value for bearing stiffness. These investigations included comparing the load and displacement data supplied by the manufacturer against published estimation techniques, parametric sensitivity of the DGM to bearing stiffness and comparison to constant speed experimental data, and hammer test frequency response analysis comparison to FEA modal results where bearing stiffness was included between shaft and casing.

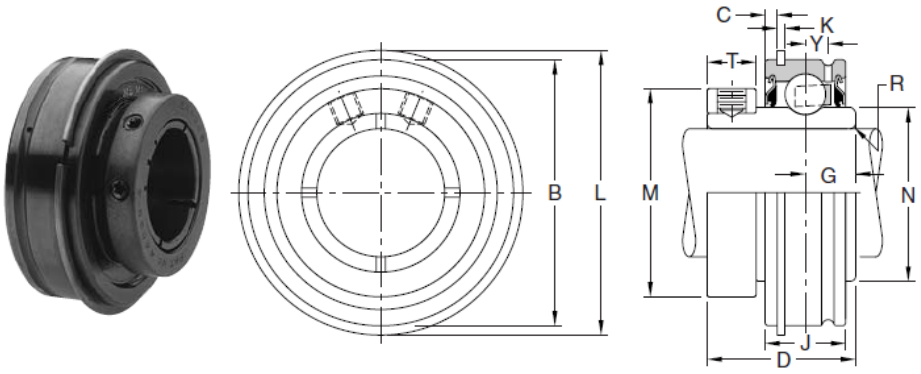

Shaft Dia. mm	Shaft Dia. Inches	Bearing Number	Basic Size	Bore Tolerance	B	C	D	G	J	K	L	N	R	S	T Width	T Tap Size	Y	Unit wt. (lbs/kg)
	1/2 5/8 3/4	ER8K ER10K ER12K	204	+.0007-.0000	1.8504	3/32	1 7/32	.405	.6240	3/64	2 1/16	.941	1 1/8 1 13/64 1 3/8	.040	9/32 9/32 11/32	#10-32 #10-32 1/4-28	.142	0.62 0.55 0.54
	1	ER16K	205		2.0472	3/32	1 3/8	.508	.7490	3/64	2 17/64	1.313	1 9/16	.040	11/32	1/4-28	.185	0.61

Figure 23. Bearing manufacturer catalog excerpt (rexnord.com).

The radial load and displacement data S supplied by the bearing manufacturer was curve-fit to a third-order polynomial with the intercept set to the origin as shown in Figure 24.

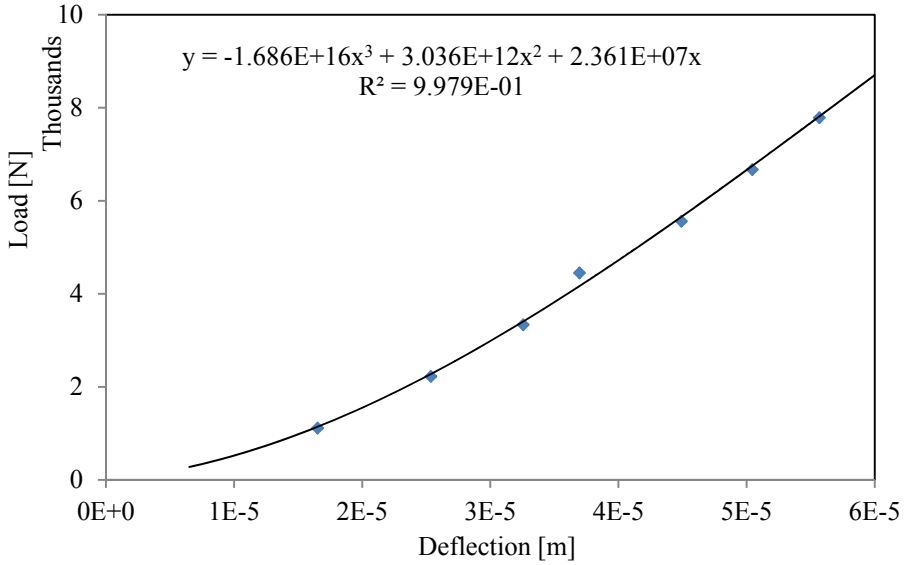

Figure 24. Bearing manufacturer supplied load and deflection data.

The first derivative of this polynomial with respect to deflection is the estimated stiffness (slope) at each load-deflection point. The stiffness values and corresponding loads are plotted in Figure 24 along with estimates made using the methods of (Garguilo, 1980) and (Krämer, 2013). Garguilo estimates the radial stiffness of deep-groove or angular-contact radial ball bearings by equation (5) and Kramer estimates bearing stiffness as equation (6).

$$K_r = (0.0325 \cdot 10^6)\sqrt[3]{DF_rZ^2 \cos^5 \alpha} \tag{5}$$

Where:
K_r = Radial bearing stiffness in lb/in.
D = Rolling-element diameter in inches
F_r = Radial external force in lbs
Z = Number of rolling elements
α = Contact angle (assumed to be zero)

$$k_r = \frac{3}{2}\frac{F}{(1.2\cdot 10^{-7})d^{1/3}Z^{2/3}F^{2/3}} \tag{6}$$

Where:
k_r = Radial bearing stiffness in N/m.
d = Rolling-element diameter in m
F = Radial load in N
Z = Number of rolling elements

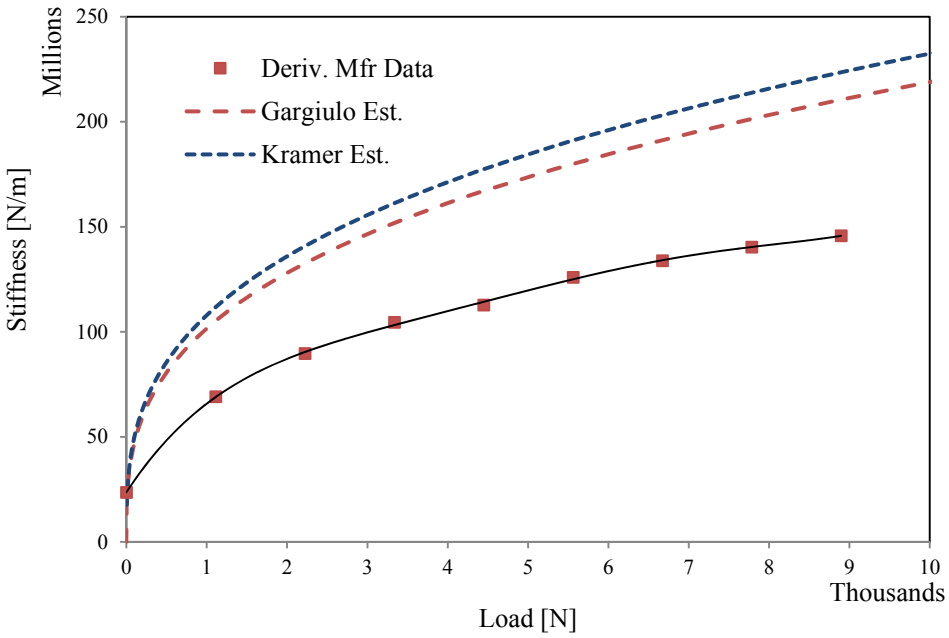

Figure 25. Bearing radial stiffness versus load

Figure 25 demonstrates that the manufacturer supplied data matches the trends from both Garguilo and Kramer even though the magnitudes do not agree. More recent work by (Guo and Parker, 2012), (Parker et al, 2012) and (Guo et al, 2014) using more complex bearing models compared their bearing stiffness curves to Garguilo's estimate and were also lower in magnitude.

While the above comparison supports the data supplied by the manufacturer, the resulting stiffness relationship is load dependent whereas the DGM requires a single value. To help identify the most appropriate single bearing stiffness value to use in the DGM, an investigation of the frequency response of the shafts in-situ is performed. This investigation identifies the bearing stiffness in a model that most closely replicates the measured frequency response. The hammer test results are compared to FEA modal analysis, DGM modal analysis, and preliminary DGM healthy results with varied bearing stiffness values.

The in-situ tests are performed without the gears engaged and without oil in the gearbox to allow for better model comparisons. The arrangement for the in-situ frequency response hammer test of the intermediate shaft is shown in Figure 26. Compared to other hammer tests performed with various

accelerometer positions, striking locations and shaft orientations, the arrangement shown is deemed the most representative.

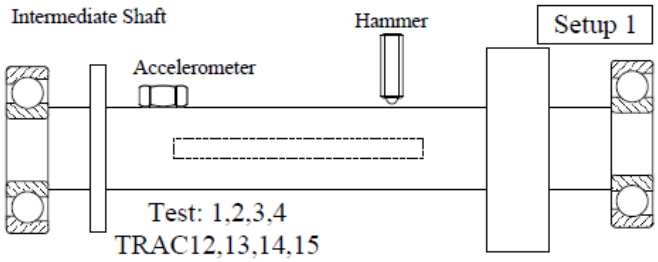

Figure 26. In-situ intermediate shaft hammer test orientation and accelerometer arrangement

A representative frequency response plot from the hammer tests is shown in Figure 27, revealing three significant peaks believed to correspond with the first three bending natural frequencies of the intermediate shaft. As stated, multiple hammer tests were performed, and some variation was experienced, but peaks at approximately 500 Hz, 1300 Hz and 1550 Hz appeared repeatedly.

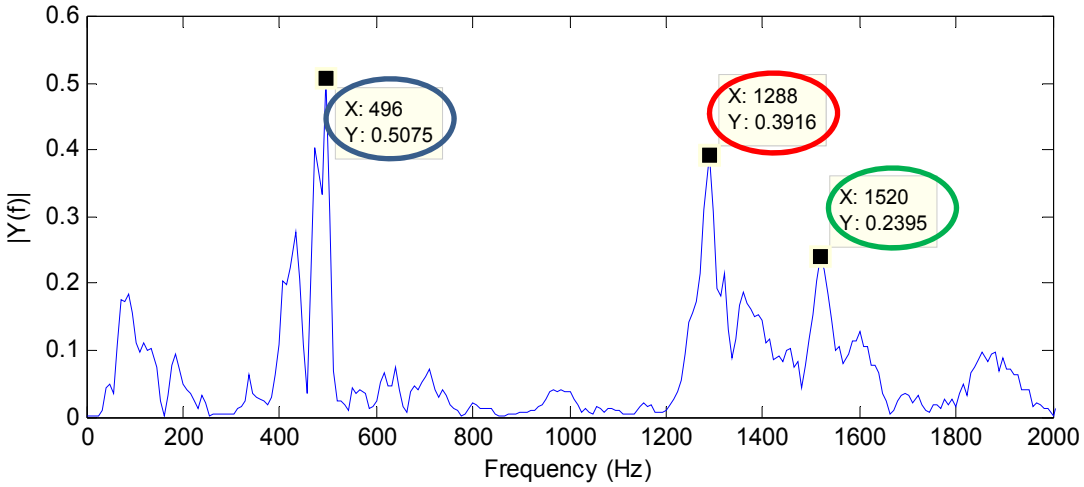

Figure 27. Hammer test frequency response from impacts on the intermediate shaft, gears disengaged.

A Solidworks Simulation FEA model of the shaft and housing assembly is shown in Figure 28. Spring elements between housing and shaft represent the bearings. The first three meaningful, non-repeated natural frequencies from modal analyses of this assembly with varying spring element stiffnesses are plotted in Figure 29.

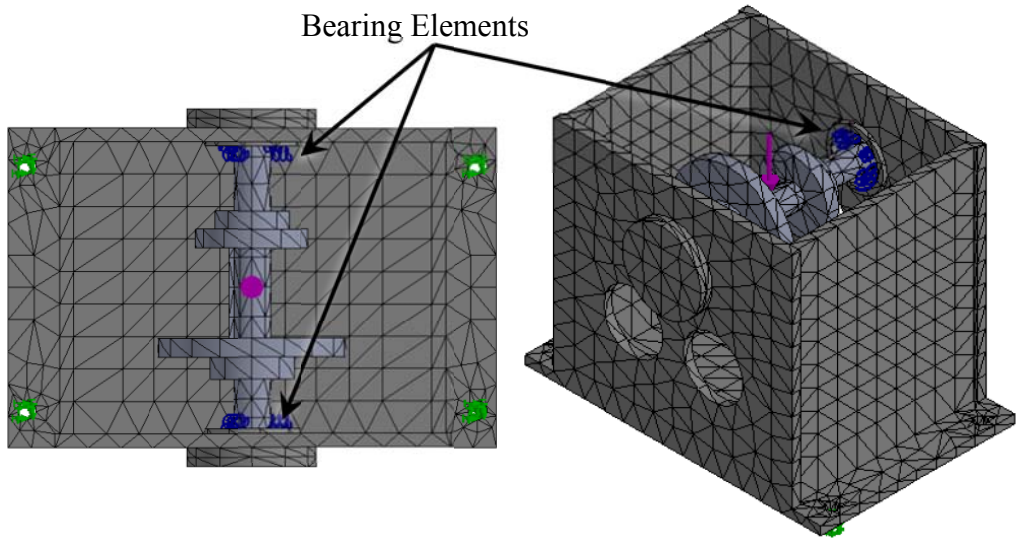

Figure 28. Intermediate shaft, casing and bearing stiffness FEA model.

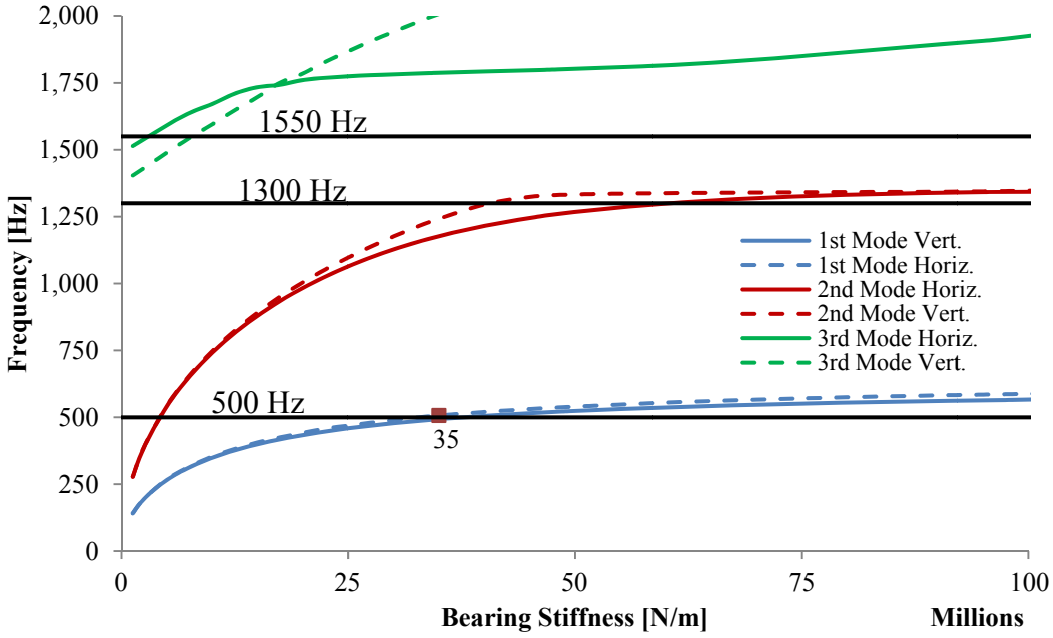

Figure 29. Natural frequency results from FEA modal analysis with varying bearing stiffness.

The mode shapes from the FEA results are used to determine which natural frequencies corresponded to shaft bending motion and therefore meaningful. The vertical and horizontal natural frequencies shown in Figure 28 are in relatively close agreement with each other for the first and second modes, but the third mode natural frequency tends to vary with direction, especially with larger spring stiffness. The results of

the first and second natural frequencies also tend to flatten out and almost converge onto the measured values (indicated with a horizontal black line), which is considered good validation of the modeling approach. Since the first and second frequencies do not intersect with their respective measured frequency at the same bearing stiffness, the intersection of the first natural frequency, approximately 35 MN/m, was used in the DGM. This value is also used in the matrix form of the DGM to determine the model eigenvalues/natural frequencies.

2.2.3. Damping

Damping is estimated from the log decrement of hammer tests on the in-situ intermediate shaft. Several hammer tests are performed in various accelerometer and hammer striking positions similar to the arrangement shown in Figure 26. Figure 30 presents an example hammer test time history with points indicating peaks of the signal. Equation (7) is applied to these points to obtain the log decrement, and equation (8) to estimate the damping ratio. Based on the data points shown here, and several other hammer test data sets, the global damping ratio, ζ, is estimated at 6.5%. This is relatively high damping but not unreasonable compared to papers by (Guilbault et al, 2012), who set the global damping from 0.5 % to 5.5%, (Dietl et al, 2000), who used between 0.7% and 4%, and (Parker et al, 2000) who used 7%.

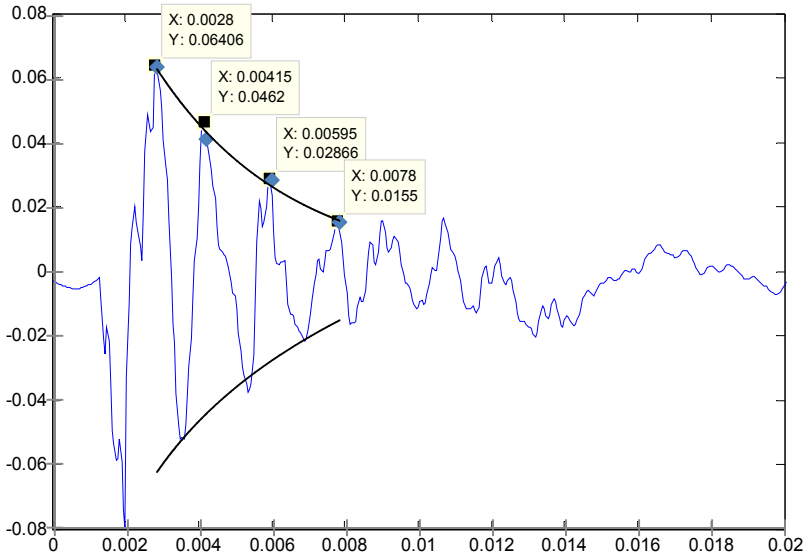

Figure 30. Damping determined from impact decay on intermediate shaft.

$$\delta = \frac{1}{N} \ln \frac{x_n}{x_{n+1}} \tag{7}$$

$$\zeta = \frac{\delta}{\sqrt{4\pi^2 + \delta^2}} \tag{8}$$

Gear teeth damping, C_m, includes both structural damping and viscous damping, and is most often simplified to a single damping ratio value, ζ, which is applied to the equivalent mass of the gear pair, m_e, and mesh stiffness. The equivalent mass is obtained from equation (9) and the damping coefficient from equation (10) in the same method used by (Özgüven, 1991).

$$m_e = \frac{I_1 I_2}{I_1 {R_1}^2 + I_2 {R_2}^2} \tag{9}$$

$$C_m = 2\zeta \sqrt{k_m m_e} \tag{10}$$

The 6.5% estimated damping ratio is applied to the torsional and bearing inertia and stiffness values, treating damping as linear, to establish a damping coefficient for each using equation (10).

Chapter 3 – Dynamic Gearbox Modeling

The previous chapter described the experimental setup and methodology used to quantify key system parameters in the gearbox test bed. This chapter describes the development of the dynamic gear model (DGM) in detail. The development includes single-stage DGMs with increasing degrees-of-freedom (DOF) and validation comparisons to benchmark data to demonstrate the modeling technique and explore the effect of number of DOF. Two-stage DGMs with increasing DOFs are then described and validation of the model with constant speed experimental data from the gearbox test bed, using the parameters developed in the previous chapter, is performed. This thorough treatment of the stages of modeling is intended to not only document what was performed in this research, but also to provide a record for future researchers to assist in their modeling efforts.

A dynamic gear model is developed from the equations-of-motion for the system, lumping parameters of components to representative degrees of freedom (DOF). The number of equations-of-motion equals the number of DOFs in the DGM. How many DOFs are included the DGM may vary by the intended purpose of the model, what features are included in the DGM, and the method of solving. There are many aspects of a real gear system that can be represented in a DGM. Historically the following gearbox physical features have frequently been incorporated into DGMs (in the order of most commonly included feature):

- Time-varying mesh stiffness
- Backlash / loss of contact / back side impact
- Damping
- Bearing stiffness
- Shaft inertia and stiffness
- Drive and load inertia
- Lateral and transverse bearing DOF's

Many of these features are discussed in later sections as they are incorporated into the higher DOF DGMs. Two features in particular, time-varying mesh stiffness and backlash, are included in every DGM and are therefore especially important. Time-varying mesh stiffness is the result of the quantity of teeth in contact at any given moment and differing location of contact along the profile of individual teeth

during engagement. This feature is described in more detail within the mesh stiffness development in previous chapter. Backlash is the clearance between mating gears, easily demonstrated by holding one shaft in place and rotating the other shaft back and forth to open and close the gaps between teeth pairs. A gear pair without backlash is impractical and may bind during operation. Backlash, however, may generate loss of contact in teeth during operation, especially during sudden changes in shaft speed. The backside of the gear pairs may even collide during these transient conditions. The loss-of-contact and backside collisions result in the clearance-type non-linearity discussed in the literature review Section 1.1.2. Time-varying mesh stiffness and backlash are responsible for much of the vibration in real gears and are therefore necessary to include in every DGM.

The features of the increasingly complex DGMs build upon each other, so this chapter is organized as a narrative in which the simplest single-stage DGM (2-DOF) is developed incrementally to a 6-DOF DGM and then compared to a benchmark test data. The simplest two-stage DGM (3-DOF) is developed incrementally to a 26-DOF DGM and validated with constant speed test data collected from the UConn Structural Dynamics and Systems Lab gearbox testbed.

3.1 Single-Stage Dynamic Model Formulation.

As described in the literature review in Chapter 1, there exists much more literature on single-stage DGMs than literature on multi-stage DGMs. To develop a two-stage DGM methodically, a single-stage DGM is first created and the results compared to benchmark experimental data while exploring the effect of DOF size on results. This section first describes several single-stage DGMs with increasing DOF and then compares each to 1996 OSU data for validation. Many early studies of dynamic models, and even some detailed recent studies, use simplified single DOF models with the angular position difference as the only variable. It is also common for the single DOF equation to be non-dimensionalized and solved for more generalized relationships. This approach has the advantage of computational simplicity and is well suited for a variety of solution methods such as the harmonic balance method. Unfortunately the output of this approach only represents rotational vibration. A DGM with a translational DOF representing the bearing location where an accelerometer is placed allows for more direct comparison of behavior. Below is a list of single-stage DGM DOFs modeled in this section, followed by a table from the literature review chapter summarizing single-stage DGMs discussed in literature and repeated here for ease of comparison:

- 2-DOF: Rotational DOF for each gear
- 4-DOF: Rotational DOF for each gear, including shaft torsional stiffness
- 6-DOF: 4-DOF + 1x1-DOF bearing per shaft

Table 8. Summary of single-stage DGM literature model DOFs

Paper	DOFs
(Özgüven and Houser, 1988)	1
(Comparin and Singh, 1989)	1
(Kahraman and Singh, 1990)	1
(Amabili and Fregolent, 1998)	1
(Bonori and Pellicano, 2007)	1
(Ding and Kahraman, 2007)	1
(Tamminana et al, 2007)	1
(Velex and Ajmi, 2007)	1
(Dion et al, 2009)	1
(Faggioni et al, 2011)	1
(Guilbault et al, 2012)	2
(Kahraman and Singh, 1991)	3
(Maliha et al, 2004)	3
(Lin et al, 1994)	4
(Özgüven, 1991)	6

Paper	DOFs
(Choy et al, 1993)	6
(Bartelmus, 2001)	6
(Parey et al, 2006)	6
(He, 2008)	6
(Wu et al, 2008)	6
(Zhou and Zuo, 2012)	6
(del Rincon et al, 2013)	6
(Inalpolat et al, 2015)	6
(Omar et al, 2011)	9
(Wan et al, 2014)	10
(Ma et al, 2015)	12
(Velex and Maatar, 1996)	14
(Zhou and Zuo, 2012)	16
(Sawalhi and Randall, 2008)	34

3.1.1. Two Degree-of-Freedom Single-Stage Dynamic Model Formulation.

Each single-stage DGM has at least two rotational degrees of freedom: one for the pinion and one for the driven gear. Figure 31 is a typical representation of a single-stage two DOF DGM.

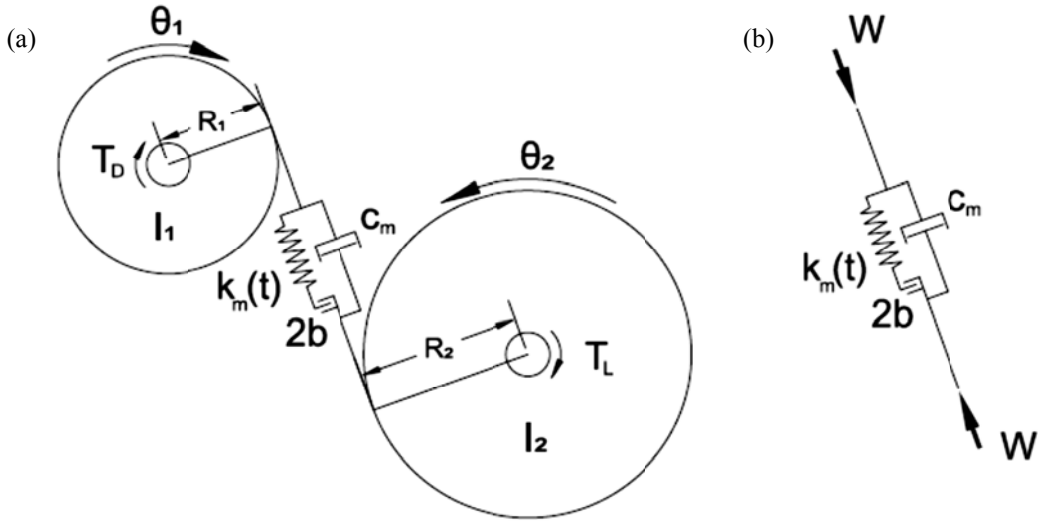

Figure 31. (a) Single-Stage Two-DOF DGM and (b) Dynamic Mesh Force Represented as a Spring, Damper and Gap

The fundamental relationship between these DOFs is the dynamic transmission error (DTE), defined as the tangential displacement along the line-of-action between the teeth in contact; it is most easily understood when described as the difference between perfect conjugate action and reality. DTE is the most often modeled parameter in numerous investigations and is expressed by equation (1).

$$DTE = R_1\theta_1 - R_2\theta_2 \tag{1}$$

Note that an error term, to represent random excitation as well as profile errors, is often included in the definition of DTE (Lin et al, 1994; Velex and Maatar, 1996; Amabili and Fregolent, 1998; Bartelmus, 2001; Bonori and Pellicano, 2007; Liu and Parker, 2008; Inalpolat et al, 2015). The DTE applied to the mesh stiffness, k_m, equals the undamped dynamic mesh force in equation (2).

$$W = k_m(R_1\theta_1 - R_2\theta_2) \tag{2}$$

Mesh stiffness is treated as a spring along the line of action whose stiffness varies with position, depending on the number of teeth pairs in contact, and interacts with the DTE. A detailed description of the mesh stiffness development is included in Chapter 2. A simplified mesh stiffness representation is used in this single-stage model, as limited information is available about the benchmark testbed. Figure 32 shows the mesh stiffness modeled as a square wave, with the larger value representing two teeth pairs in contact and the lower a single teeth pair in contact.

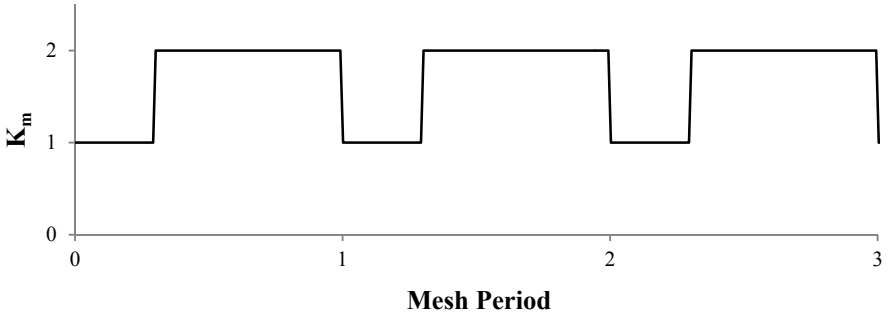

Figure 32. Simplified Time-varying Mesh Stiffness.

Backlash, $2b$, is the clearance within the gear pair which may cause momentary loss of contact between teeth pairs or even backside impact. Backlash is a source of non-linear behavior in gear systems and has been investigated as part of numerous gear studies, especially those focusing on "jumps" of DTE magnitude with increasing versus decreasing operating speed. Backlash is often represented as a "dead zone" in the meshing stiffness [10] as shown in Figure 3, and modeled as equation (3).

$$W = \begin{cases} k_m(DTE - b), & DTE > b \\ 0, & -b < DTE < b \\ k_m(DTE + b), & DTE < -b \end{cases} \tag{3}$$

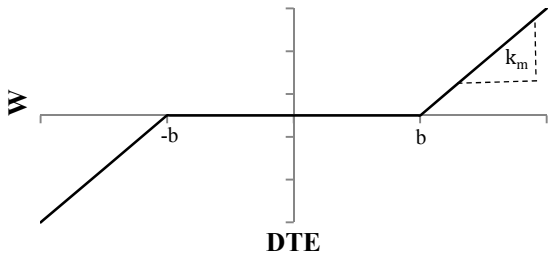

Figure 33. Backlash loss of contact

The equations of motion, (4) and (5), for each rotational DOF, $\theta_1$and θ_2, are balanced by the driving torque, T_D, and load torque, T_D, and the damped dynamic mesh force, W, which acts along the line of action on each gear in opposing directions, applied to the respective pitch radius, R, moment arm.

$$I_1\ddot{\theta}_1 = -WR_1 + \alpha T_D \tag{4}$$

$$I_2\ddot{\theta}_2 = WR_2 - T_D \tag{5}$$

$$W = k_m(t)(R_1\theta_1 - R_2\theta_2) + c_m\left(R_1\dot{\theta}_1 - R_2\dot{\theta}_2\right) \tag{6}$$

The variable α represents a multiplier, referred to here as torque factor, which is used to control the speed of the DGM by changing the balance between drive and load torques. The torque factor was described in more detail in the previous chapter and is used to simulate the ramp up and ramp down for the single-stage DGM comparison to benchmark data and, later, in the two-stage DGM to explore non-stationary behavior.

3.1.2. Four Degree-of-Freedom Single Stage Dynamic Model Formulation.

Figure 34 shows the four-DOF DGM which adds the rotations of the drive motor and the load to the two-DOF DGM. The moment of inertia of the motor and load are included in this model, as are the two shaft torsional stiffnesses and damping.

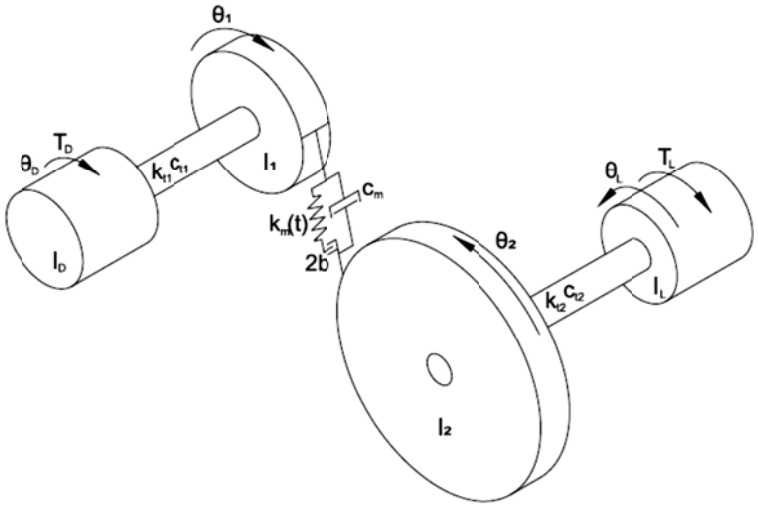

Figure 34. Single-Stage 4-DOF DGM

Equations (7) through (10) are the four equations-of-motion for the model which are coupled by the dynamic mesh force of equation (11).

$$I_D\ddot{\theta}_D + c_{t1}\left(\dot{\theta}_D - \dot{\theta}_1\right) + k_{t1}(\theta_D - \theta_1) = \alpha T_D \tag{7}$$

$$I_1\ddot{\theta}_1 - c_{t1}\left(\dot{\theta}_D - \dot{\theta}_1\right) - k_{t1}(\theta_D - \theta_1) + WR_1 = 0 \tag{8}$$

$$I_2\ddot{\theta}_2 + c_{t2}\left(\dot{\theta}_2 - \dot{\theta}_L\right) + k_{t2}(\theta_2 - \theta_L) - WR_2 = 0 \tag{9}$$

$$I_L\ddot{\theta}_L - c_{t2}\left(\dot{\theta}_2 - \dot{\theta}_L\right) - k_{t2}(\theta_2 - \theta_L) = -T_L \tag{10}$$

$$W = k_m(t)(R_1\theta_1 - R_2\theta_2) + c_m\left(R_1\dot{\theta}_1 - R_2\dot{\theta}_2\right) \tag{11}$$

3.1.3. Six Degree-of-Freedom Single Stage Dynamic Model Formulation.

The six-DOF model is based on the model described by (Ozguven, 1991) and includes all of the features of the four-DOF, plus translational DOFs on each shaft to represent the bearings. Figure 35 is a representation of the model showing a single bearing supports each shaft. The bearings act in only one direction, aligned with the line of action. The MATLAB code developed for this model (and heavily modified for all other models in this research) builds upon code documented by (Parey and Tandon, 2010) which was based on (Ozguven, 1991).

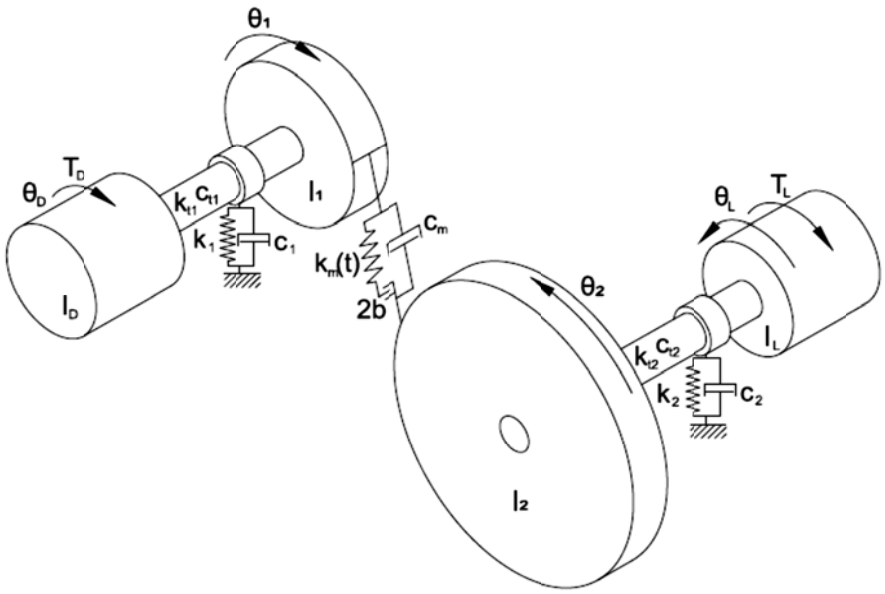

Figure 35. Single Stage 6-DOF DGM

The six-DOF model presented in equations (12-17) adds two translational DOFs to the four-DOF model. These translational DOFs are coupled to the four rotational DOFs via the dynamic mesh force of equation (18). The accelerations found from solving the model bearing translational DOFs, $\ddot{y}_1$ and $\ddot{y}_2$, can be compared to measured bearing accelerations of a physical testbed's accelerometers.

$$I_D\ddot{\theta}_D + c_{t1}\left(\dot{\theta}_D - \dot{\theta}_1\right) + k_{t1}(\theta_D - \theta_1) = \alpha T_D \tag{12}$$

$$I_1\ddot{\theta}_1 - c_{t1}\left(\dot{\theta}_D - \dot{\theta}_1\right) - k_{t1}(\theta_D - \theta_1) + WR_1 = 0 \tag{13}$$

$$I_2\ddot{\theta}_2 + c_{t2}\left(\dot{\theta}_2 - \dot{\theta}_L\right) + k_{t2}(\theta_2 - \theta_L) - WR_2 = 0 \tag{14}$$

$$I_L\ddot{\theta}_L - c_{t2}\left(\dot{\theta}_2 - \dot{\theta}_L\right) - k_{t2}(\theta_2 - \theta_L) = -T_L \tag{15}$$

$$m_1\ddot{y}_1 + c_1\dot{y}_1 + k_1y_1 - W = 0 \tag{16}$$

$$m_2\ddot{y}_2 + c_2\dot{y}_2 + k_2y_2 + W = 0 \tag{17}$$

$$W = k_m(t)(R_1\theta_1 - R_2\theta_2 - y_1 + y_2) + c_m\left(R_1\dot{\theta}_1 - R_2\dot{\theta}_2 - \dot{y}_1 + \dot{y}_2\right) \tag{18}$$

3.1.4. Single-Stage DGM Solution Method.

The single-stage DGMs described in the previous sections are written as MATLAB code functions and solved using Runge Kutta time marching with time steps matching the experimental data sampling frequency, 20 kHz.

A generalized form of the DGM equations can be written in matrix notation as Equation 19 and expanded to Equations (20) through (23).

$$\mathbf{M}\ddot{\mathbf{z}} + \mathbf{C}\dot{\mathbf{z}} + \mathbf{K}\mathbf{z} = \mathbf{F} \tag{19}$$

where

$$\mathbf{M} = \begin{bmatrix} I_1 & 0 & 0 & \cdots & 0 \\ 0 & I_2 & 0 & \cdots & 0 \\ 0 & 0 & I_3 & \cdots & 0 \\ \vdots & \vdots & \vdots & \ddots & 0 \\ 0 & 0 & 0 & 0 & m_{10} \end{bmatrix} \tag{20}$$

$$\mathbf{K} = \begin{bmatrix} k_{t1} & -k_{t1} & 0 & \cdots & 0 \\ -k_{t1} & k_{t1} + k_{m1}{R_1}^2 & -k_{m1}R_1R_2 & \cdots & 0 \\ 0 & -k_{m1}R_1R_2 & k_{t2} + k_{m1}{R_2}^2 & \cdots & 0 \\ \vdots & \vdots & \vdots & \ddots & 0 \\ 0 & 0 & 0 & 0 & k + k_{b3} \end{bmatrix} \tag{21}$$

$$\mathbf{C} = \begin{bmatrix} c_{t1} & -c_{t1} & 0 & \cdots & 0 \\ -c_{t1} & c_{t1} + c_{m1}{R_1}^2 & -c_{m1}R_1R_2 & \cdots & 0 \\ 0 & -c_{m1}R_1R_2 & c_{t2} + c_{m1}{R_2}^2 & \cdots & 0 \\ \vdots & \vdots & \vdots & \ddots & 0 \\ 0 & 0 & 0 & 0 & c + c_{b3} \end{bmatrix} \tag{22}$$

$$\mathbf{F} = [T_D \quad 0 \quad \cdots \quad T_L \quad \cdots \quad 0]^T \tag{23}$$

This expansion is performed for each DGM for several uses. The stiffness and applied load matrices are used to find the initial displacement conditions for solving the DGMs. These displacements reduce the model's tendency to "hunt" at the beginning of the solution when starting at zero displacement. The initial velocity conditions are set to the desired shaft speed or just above or just below depending on it being a constant speed solution or a solution used to demonstrate the non-linear jump phenomenon. The matrix forms of the equations DGM are also used to determine the model eigenvalues, which are used to explore the effects of parameter variation on the natural frequencies of the system. Lastly, the matrices are used to find the Modal Space solution to the DGM for comparison to the linear solution found when keeping the time-varying mesh stiffness constant and removing the backlash term. The latter is a check on the performance of the DGM as well as the sign conventions used.

The purpose of running the single-stage models is to validate the solution technique, namely the Runge Kutta time marching, which has been described by many DGM articles (and written in MATLAB code within (Parey and Tandon, 2010)) but rarely fully and thoroughly demonstrated. Performing these checks also assists developing the two-stage DGMs for comparison to the experimental gearbox test bed.

3.2. Single Stage Model Validation to Benchmark Test Data

Many previous gear modeling efforts have used the results of only a few published gear test results for comparison, establishing these as benchmarks, including the work of (Kahraman and Blankenship, 1996) from OSU. This benchmark data is plotted as root-mean-squared DTE versus input shaft speed. The data demonstrates the non-linear "jump" phenomenon wherein the steady state DTE resolves to one of two values at various speeds depending on whether the machine accelerated up to or decelerated down to each speed. Parameters for the OSU testbed are compiled from a variety of works (Tamminana et al, 2007), (Faggioni et al, 2011) and (Ding, 2007) and presented in Table 9.

Table 9. Parameters Used in Models of Benchmark

Parameter	Value	Units
No. Gear Teeth, N_1, N_2	50, 50	
Module	3	mm
Pressure Angle	20	degrees
Pitch Radius, R_1, R_2	70.5, 70.5	mm
Contact Ratio, λ_1	1.5, 1.4, 1.75	
Drive Torque, T_D	85, 170, 340	N-m
Moment of Inertia, I_D, I_1, I_2, I_L	$5.75x10^{-3}$, $7.875x10^{-3}$, $7.875x10^{-3}$, $1.15x10^{-2}$	kg-m^2
Mass, m_1, m_2	2.8	kg
Shaft Stiffness, k_{t1}, k_{t2}	168,294, 25,244	N-m/rad
Bearing Stiffness, k_1, k_2	$2x10^{10}$	N/m
Average Mesh Stiffness, k_m	$4.62x10^8$	N/m
Shaft Damping, k_{t1}, k_{t2}	2.43	N-s/rad
Bearing Damping, c_1, c_2	4,733	N-s/m
Damping Ratio, ζ	0.01	
Backlash, 2b	$4x10^{-4}$	m

The matrix forms of the two-, four-, and six-DOF DGMs described in the previous sections are populated with the parameters in Table 9, including the average mesh stiffness and the natural frequencies solved that are presented in Table 10. The first natural frequency of each is zero which coincides with

rotational rigid body motion since the unloaded models have no rotational constraints. The 2nd natural frequency of the 2-DOF DGM is associated with the mesh stiffness and shifts to the 4th natural frequency of the 4- and 6-DOF DGMs. The 2nd and 3rd natural frequencies of the 4-DOF DGM are due to the shaft torsion, since these are the only differences from the 2-DOF DGM, and remain the same for the 6-DOF DGM. The 5th and 6th natural frequencies of the 6-DOF DGM are therefore associated with the bearing stiffness. This natural frequency breakdown of incrementally larger DGMs demonstrates one method to determine the influence of each parameter on the model behavior. According to (Tamminana et al, 2007), who had access to the OSU '96 testbed, "…the measured primary resonance is 3100 Hz and the first two superharmonic resonances near 1550 Hz and 1000 Hz…" As the measured frequencies were no doubt used to develop some of the parameters, the agreement of the 2nd natural frequency of the 2-DOF DGM of the present to this primary resonance is simply confirmation the modeling technique.

Table 10. Natural Frequencies of Benchmark DGMs

Mode	2-DOF	4-DOF	6-DOF
1	0	0	0
2	3139	290	290
3		1,003	1,003
4		3,886	3,795
5			13,451
6			13,784

The DGMs are solved repeated for multiple speeds at increments matching the published benchmark data points. Each model is solved by "running up to" or "running down to" the steady state speed. Figures 36 through 38 show comparisons of the DGM results to OSU '96 data. The trends of the model results follow well with those of the test results. Note the six DOF model resolved to low values and high values at speeds that overlap, in the same manner as the test data. These are the "jumps" that are expected from non-linear behavior where two or more solutions exist for the same dependent parameter. In other words, the modeling technique appears to capture this physical phenomenon even though there are notable differences between model and data. Some of these differences are attributed to the lack of

available parameters directly from the original testbed, as some of the sources acknowledge the parameters they're using are estimated. Other modeling efforts using these data for comparison, such as (Maliha et al, 2004), achieve the same or even less trend correlation as the present research. Based on capturing the jump behavior and similarity to published data, the single-stage modeling approach is considered validated and suitable for extension to the two-stage DGM.

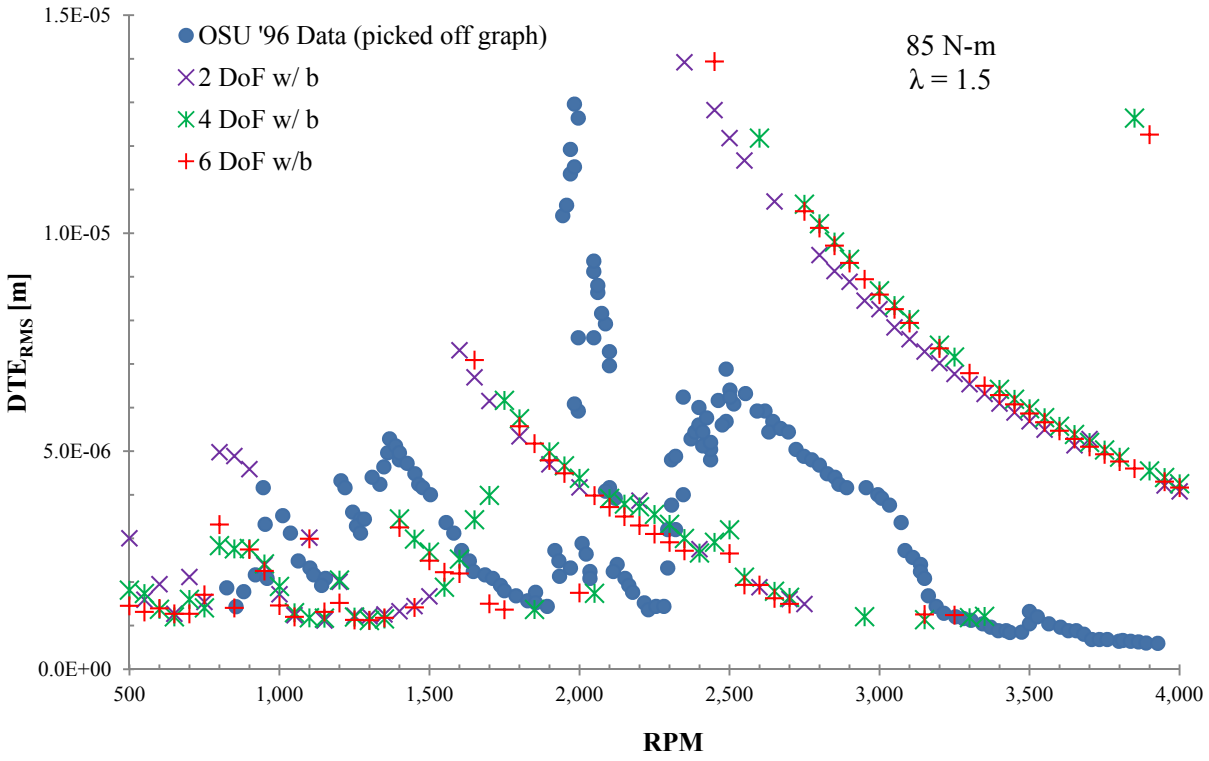

Figure 36. Two-, Four- and Six DOF DGM Results Comparison and Benchmark Data; 85 N-m Torque and 1.5 Contact Ratio

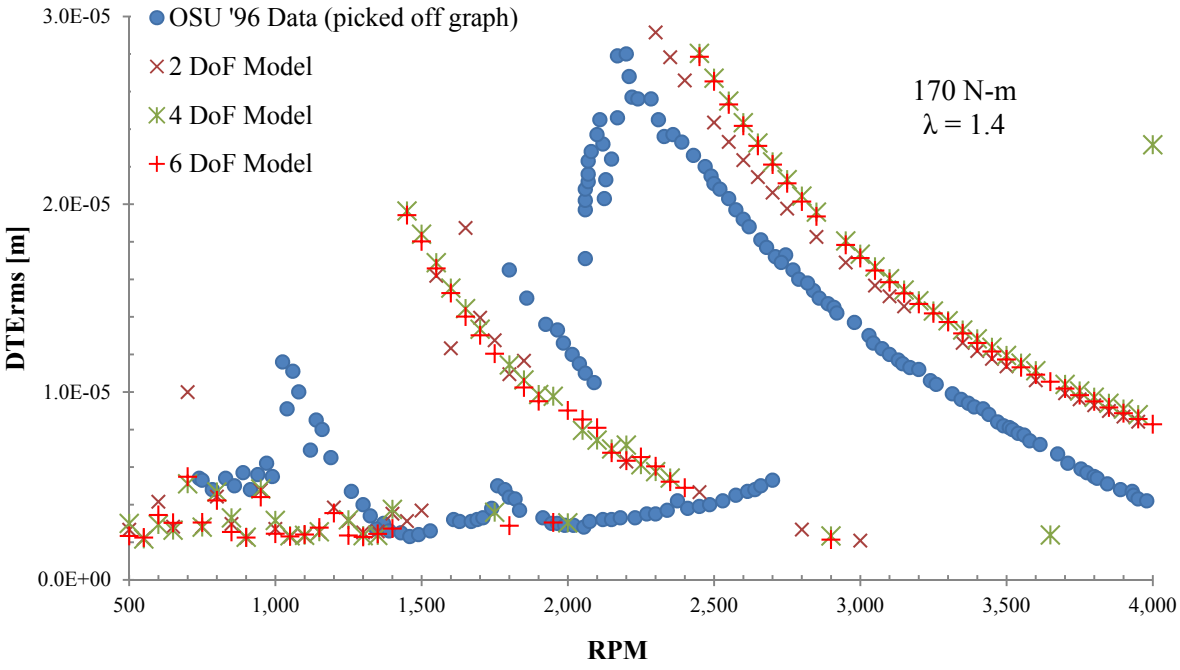

Figure 37. Two-, Four- and Six DOF DGM Results Comparison and Benchmark Data; 170 N-m Torque and 1.4 Contact Ratio

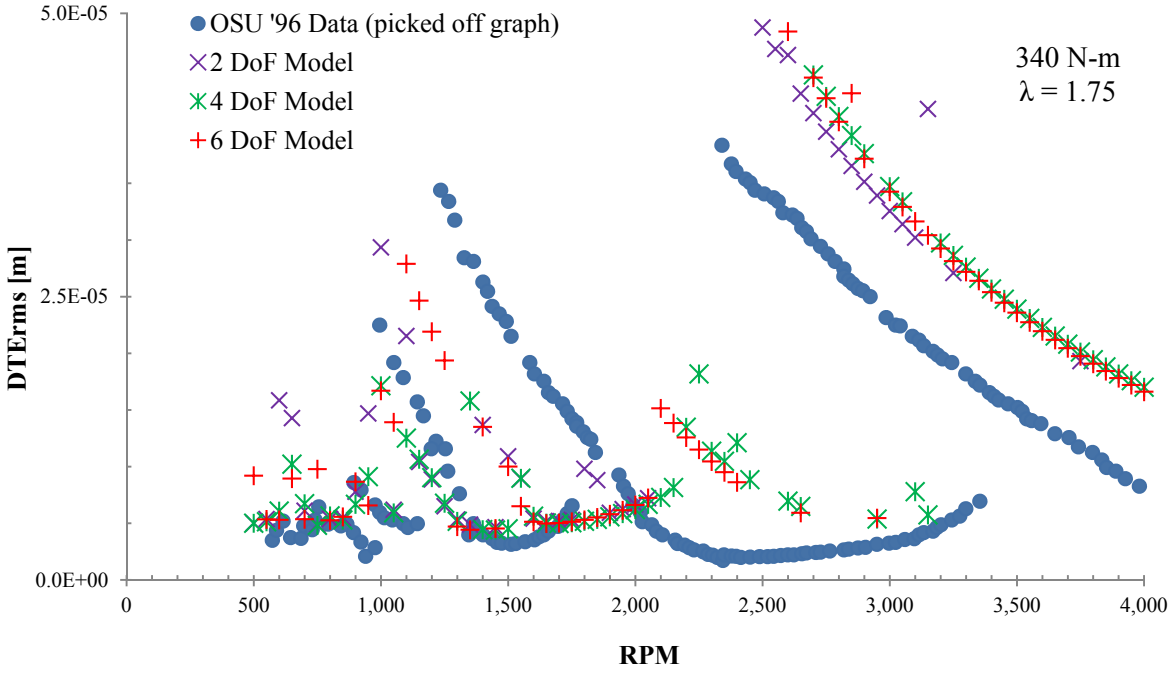

Figure 38. Two-, Four- and Six DOF DGM Results Comparison and Benchmark Data; 340 N-m Torque and 1.75 Contact Ratio

3.3 Two Stage Dynamic Model Formulation.

The modeling strategies used in the single-stage DGMs are now extended to a two-stage gear testbed. The testbed described in Chapter 2 is used as the focus of this discussion. Figure 39 demonstrates the arrangement of the three shafts and two gear pairs in an equilateral triangle. The pressure angle of the gears used in the testbed, 14.5°, is shown along with the resulting angle to horizontal due to the arrangement. This will be useful later to break down the force components. Figure 40 similarly shows the orientation of the DGM forces which are dependent on relative angular position, time-varying mesh stiffness, damping and backlash gap.

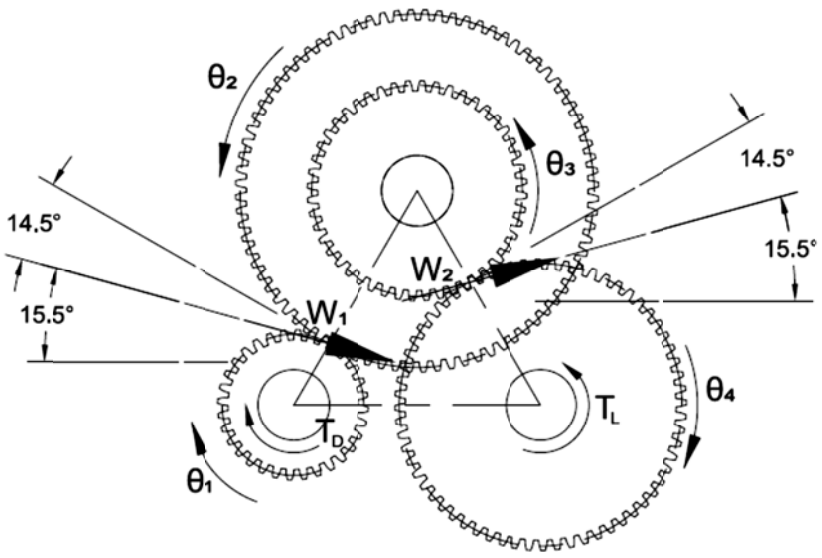

Figure 39. Two-Stage Gear Set Force Arrangement

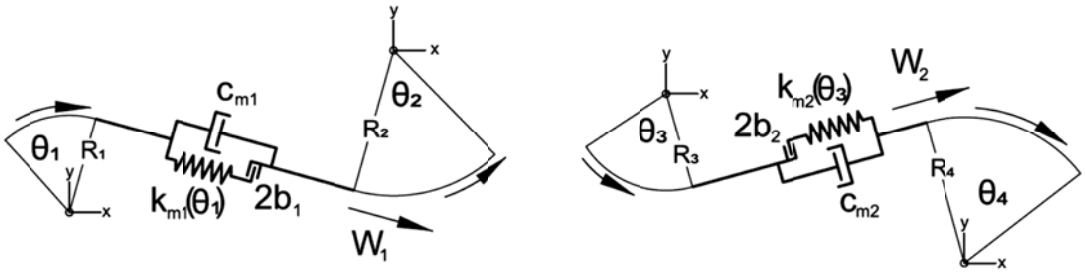

Figure 40. Two-Stage DGM Force Arrangement

The number of degrees-of-freedom (DOFs) representing a two-stage gear set in a DGM can range from a minimum of three (in which the angular displacement of each gear is modeled) to very large finite element models that attempt to incorporate all the local details. In general, a model must be sufficiently complex to capture the desired physical features while being small-scale enough for practical computational solving speeds.

The following is a list of two-stage DGM DOFs modeled in this section:

- 3-DOF: Rotational DOF for each shaft
- 6-DOF: Rotational DOF for drive, gears and load, including shaft torsional stiffness
- 9-DOF: 6-DOF + 1x1-DOF bearing per shaft,
- 9-DOF: 3-DOF + 1x2-DOF (x & y) bearings per shaft
- 12-DOF: 6-DOF + 2x1-DOF bearing per shaft,
- 26-DOF: 6-DOF + 2x2-DOF (x & y) bearings per shaft, including shaft bending stiffness

These models represent a progression of included features whose effects will be discussed in a later section on two-stage DGM validation against constant speed test data. Table 11 is a repeat of a table from the literature review chapter summarizing two-stage DGMs discussed in literature for comparison to the models described in this chapter.

Table 11. Summary of two-stage DGM literature model DOFs

Paper	DOFs
(Al-shyyab and Kahraman, 2005)	2
(Yang, 2013)	2
(Al-shyyab and Kahraman, 2007)	6
(Liu and Parker, 2008) (Note: idler gear DGM)	8
(Kubur and Kahraman, et al, 2004)	12
(Walha, 2012)	12
(Jia et al, 2003)	26

More DOFs are possible as are more modeled features. Features included in other DGMs but omitted in these models include manufacturing indexing errors (Inalpolat et al, 2015), gear profile and runout errors (Bonori and Pellicano, 2007), gear teeth friction (Howard et al, 2001), gyroscopic effects (Wan et al, 2014), and the influence of the gearbox housing (Parker et al, 2012). These omitted features will be included in future research.

3.3.1 Three Degree-of-Freedom Two-Stage Dynamic Model Formulation.

The simplest two-stage DGM used in this research is the 3-DOF model shown in Figure 11 which consists of the angular position of each shaft. Note that it is possible to create a 2-DOF DGM if the transmission error of each gear pair is used as has been done by (Al-shyyab and Kahraman, 2005) and (Yang, 2013). The three rotational equations-of-motion, (24) through (26), are coupled by the two dynamic mesh forces, Equations (27) and (28).

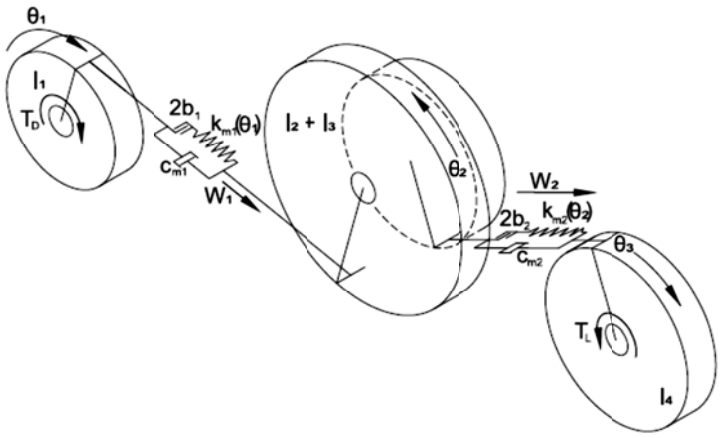

Figure 41. Two-Stage 3-DOF DGM

$$I_1\ddot{\theta}_1 = \alpha \cdot T_D - W_1R_1 \tag{24}$$

$$(I_2 + I_3)\ddot{\theta}_2 = W_1R_2 - W_2R_3 \tag{25}$$

$$I_4\ddot{\theta}_3 = W_2R_4 - T_L \tag{26}$$

$$W_1 = k_{m1}(\theta_1) \cdot DTE_1 + C_{m1}\left(\dot{\theta}_1R_1 - \dot{\theta}_2R_2\right) \tag{27}$$

$$W_2 = k_{m2}(\theta_2) \cdot DTE_2 + C_{m2}\left(\dot{\theta}_2R_3 - \dot{\theta}_3R_4\right) \tag{28}$$

The Dynamic Transmission error (DTE) is defined as, for each respective gear pair as Equations (29) and (30).

$$DTE_1 = \begin{cases} (R_1\theta_1 - R_2\theta_2) - b & (R_1\theta_1 - R_2\theta_2) > b \\ 0 & b \le (R_1\theta_1 - R_2\theta_2) \le b \\ (R_1\theta_1 - R_2\theta_2) + b & (R_1\theta_1 - R_2\theta_2) < b \end{cases} \tag{29}$$

$$DTE_2 = \begin{cases} (R_3\theta_2 - R_4\theta_3) - b & (R_3\theta_2 - R_4\theta_3) > b \\ 0 & b \le (R_3\theta_2 - R_4\theta_3) \le b \\ (R_3\theta_2 - R_4\theta_3) + b & (R_3\theta_2 - R_4\theta_3) < b \end{cases} \quad (30)$$

As previously discussed in the single-stage DGM section, DTE is a loss-of-contact non-linear function with the inclusion of backlash, $2b$, the clearance between gear-pair teeth along the line-of-action. The torque factor, α, applied to the drive torque, was previously mentioned in the single-stage DGMs, but was not used in the solutions for run-up and run-down jump phenomenon. This factor will be used to control the speed of the DGM to match the non-stationary operation in Chapter 4.

3.3.2. Six Degree-of-Freedom Two Stage Dynamic Model Formulation.

The 6-DOF two-stage DGM shown in Figure 42 separates the 1st stage gear and 2nd stage pinion of the 3-DOF DGM, adds drive and load rotational DOFs, and includes shaft torsional stiffnesses. This added complexity, though not necessarily helpful in making the 3-DOF better representative of the physical testbed, is useful as a bridge from the simple 3-DOF DGM to the larger DGMs, allowing an analysis of the effect of inclusion of these features.

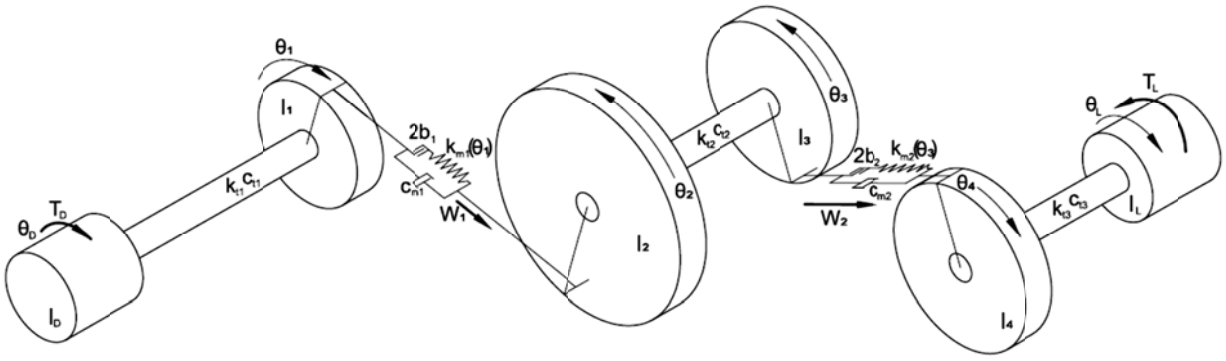

Figure 42. Two-Stage 6-DOF DGM

The equations of motion for the two-stage 6-DOF DGM are Equations (31) through (36) which are coupled by the dynamic mesh forces of Equations (37) and (38).

$$I_D\ddot{\theta}_D = \alpha \cdot T_D - c_{t1}(\dot{\theta}_D - \dot{\theta}_1) - k_{t1}(\theta_D - \theta_1) \quad (31)$$

$$I_1\ddot{\theta}_1 = -W_1R_1 + c_{t1}(\dot{\theta}_D - \dot{\theta}_1) + k_{t1}(\theta_D - \theta_1) \quad (32)$$

$$I_2\ddot{\theta}_2 = W_1R_2 - c_{t2}(\dot{\theta}_2 - \dot{\theta}_3) - k_{t2}(\theta_2 - \theta_3) \quad (33)$$

$$I_3\ddot{\theta}_3 = -W_2R_3 + c_{t2}(\dot{\theta}_2 - \dot{\theta}_3) + k_{t2}(\theta_2 - \theta_3) \quad (34)$$

$$I_4\ddot{\theta}_4 = W_2R_4 - c_{t3}(\dot{\theta}_4 - \dot{\theta}_L) - k_{t3}(\theta_4 - \theta_L) \quad (35)$$

$$I_L\ddot{\theta}_L = -T_L + c_{t3}(\dot{\theta}_4 - \dot{\theta}_L) + k_{t3}(\theta_4 - \theta_L) \quad (36)$$

$$W_1 = k_{m1}(\theta_1) \cdot DTE_1 + c_{m1}(R_1\dot{\theta}_1 - R_2\dot{\theta}_2) \quad (37)$$

$$W_2 = k_{m2}(\theta_3) \cdot DTE_2 + c_{m2}(R_3\dot{\theta}_3 - R_4\dot{\theta}_5) \quad (38)$$

3.3.3. Nine Degree-of-Freedom Two Stage Dynamic Model Formulation.

The 9-DOF DGM shown in Figure 43 builds upon the 6-DOF model by adding a single-direction bearing on each of the three shafts. This bearing (although shown vertically in the figure) is aligned with the line-of-actions and assumes both line-of-actions are also aligned. Figure 44 shows another arrangement of this DGM to emphasize the configuration necessary to have the three bearings and the two lines-of-action aligned, though the drive, shafts and load are not shown.

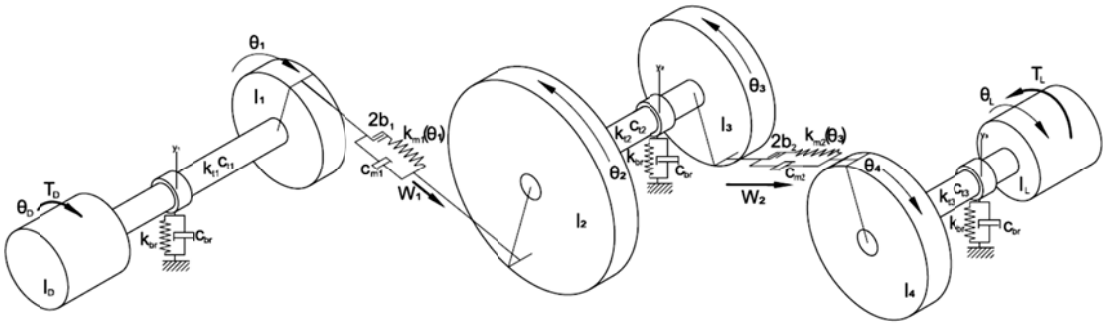

Figure 43. Two-Stage 9-DOF DGM

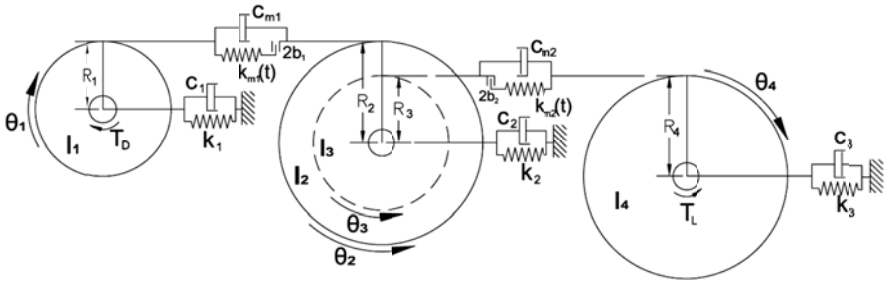

Figure 44. Two-Stage 9-DOF DGM Aligned Arrangement

One can see from this awkward arrangement that the acceleration results from solving this DGM are unlikely to replicate the dynamic behavior of the physical testbed. It is nonetheless worthwhile to solve this model and compare the results to the lesser DOF and greater DOF DGM results.

The rotational equations-of –motion are Equations (39) through (44), the translational are Equations (45) through (47), and these are all coupled together by the dynamic mesh forces of Equations (48) and (49).

$$I_D\ddot{\theta}_D = \alpha \cdot T_D - c_{t1}\left(\dot{\theta}_D - \dot{\theta}_1\right) - k_{t1}(\theta_D - \theta_1) \tag{39}$$

$$I_1\ddot{\theta}_1 = -W_1R_1 + c_{t1}\left(\dot{\theta}_D - \dot{\theta}_1\right) + k_{t1}(\theta_D - \theta_1) \tag{40}$$

$$I_2\ddot{\theta}_2 = W_1R_2 - c_{t2}\left(\dot{\theta}_2 - \dot{\theta}_3\right) - k_{t2}(\theta_2 - \theta_3) \tag{41}$$

$$I_3\ddot{\theta}_3 = -W_2R_3 + c_{t2}\left(\dot{\theta}_2 - \dot{\theta}_3\right) + k_{t2}(\theta_2 - \theta_3) \tag{42}$$

$$I_4\ddot{\theta}_4 = W_2R_4 - c_{t3}\left(\dot{\theta}_4 - \dot{\theta}_L\right) - k_{t3}(\theta_4 - \theta_L) \tag{43}$$

$$I_L\ddot{\theta}_L = -T_L + c_{t3}\left(\dot{\theta}_4 - \dot{\theta}_L\right) + k_{t3}(\theta_4 - \theta_L) \tag{44}$$

$$m_1\ddot{y}_1 = -c\dot{y}_1 - ky_1 + W_1 \tag{45}$$

$$m_2\ddot{y}_2 = -c\dot{y}_2 - ky_2 - W_1 + W_2 \tag{46}$$

$$m_3\ddot{y}_3 = -c\dot{y}_3 - ky_3 - W_2 \tag{47}$$

$$W_1 = k_{m1}(\theta_1) \cdot DTE_1 + c_{m1}\left(R_1\dot{\theta}_1 - R_2\dot{\theta}_2\right) - k_{m1}(y_1 - y_2) - c_{m1}(\dot{y}_1 - \dot{y}_2) \tag{48}$$

$$W_2 = k_{m2}(\theta_3) \cdot DTE_2 + c_{m2}\left(R_3\dot{\theta}_3 - R_4\dot{\theta}_5\right) - k_{m2}(y_2 - y_3) - c_{m2}(\dot{y}_2 - \dot{y}_3) \tag{49}$$

3.3.4. Alternative Nine Degree-of-Freedom Two Stage Dynamic Model Formulation.

A different 9-DOF DGM is possible where driver, load and shafts are removed and a bi-directional bearing is added at each gear center (where shafts would be located), with the 1st stage gear and 2nd stage pinion sharing a gear center. This 9-DOF DGM, represented by Figure 45, is the 3-DOF DGM with the addition of the bi-directional bearings. Using bearings with vertical and horizontal directions allows correct alignment of the line-of-actions with respect to the physical testbed (see Figure 9). The three rotational equations-of-motion, (50) through (52) and six translational equations-of-motion (53) through (58), are coupled by the two dynamic mesh forces equations, (59) and (60). Note that sines, cosines and sign conventions are carefully selected for correct orientation and interdependency. A critical check of

the sign conventions occurs when solving the eigenvalues of the matrix form of these equations, as they are easily reversed. Some of the drawbacks of this configuration are the sharing of the 1st stage gear and 2nd stage rotational DOF and the omission of shaft compliance. This shortcoming is resolved using the 12-DOF DGM.

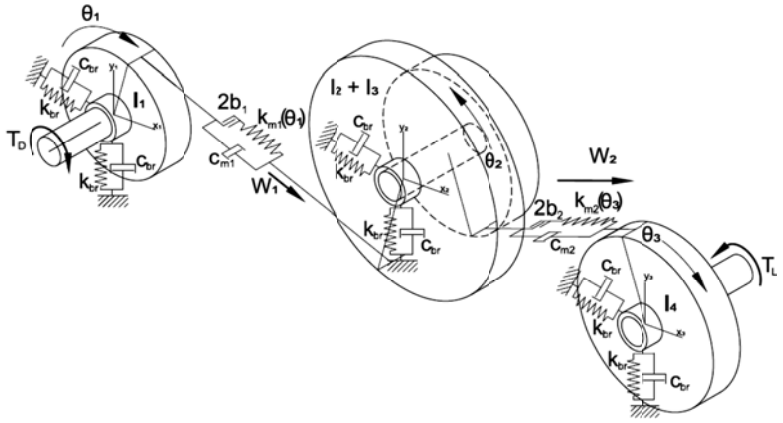

Figure 45. Alternative Two-Stage 9-DOF DGM

$$I_1\ddot{\theta}_1 = \alpha \cdot T_D - W_1R_1 \quad (50)$$

$$(I_2 + I_3)\ddot{\theta}_2 = W_1R_2 - W_2R_3 \quad (51)$$

$$I_4\ddot{\theta}_3 = W_2R_4 - T_L \quad (52)$$

$$m_1\ddot{x}_1 = -c\dot{x}_1 - kx_1 - W_1 \cdot \cos(15.5) \quad (53)$$

$$m_1\ddot{y}_1 = -c\dot{y}_1 - ky_1 + W_1 \cdot \sin(15.5) \quad (54)$$

$$m_2\ddot{x}_2 = -c\dot{x}_2 - kx_2 + W_1 \cdot \cos(15.5) - W_2 \cdot \cos(15.5) \quad (55)$$

$$m_2\ddot{y}_2 = -c\dot{y}_2 - ky_2 - W_1 \cdot \sin(15.5) - W_2 \cdot \sin(15.5) \quad (56)$$

$$m_3\ddot{x}_3 = -c\dot{x}_3 - kx_3 + W_1 \cdot \cos(15.5) \quad (57)$$

$$m_3\ddot{y}_3 = -c\dot{y}_3 - ky_3 + W_2 \cdot \sin(15.5) \quad (58)$$

$$W_1 = k_{m1}(\theta_1) \cdot DTE_1 + c_{m1}\left(R_1\dot{\theta}_1 - R_2\dot{\theta}_2\right) + cos(15.5)\,[k_{m1}(x_1 - x_2) + c_{m1}(\dot{x}_1 - \dot{x}_2)] - sin(15.5)\,[k_{m1}(y_1 - y_2) + c_{m1}(\dot{y}_1 - \dot{y}_2)] \quad (59)$$

$$W_2 = k_{m2}(\theta_2) \cdot DTE_2 + c_{m2}\left(R_3\dot{\theta}_2 - R_4\dot{\theta}_3\right) + cos(15.5)\,[k_{m2}(x_2 - x_3) + c_{m2}(\dot{x}_2 - \dot{x}_3)] + sin(15.5)\,[k_{m2}(y_2 - y_3) + c_{m2}(\dot{y}_2 - \dot{y}_3)] \quad (60)$$

3.3.5. Twelve Degree-of-Freedom Two- Stage Dynamic Model Formulation.

The 12-DOF two-stage DGM, shown in Figure 46, adds a bi-directional bearing to each shaft of the 6-DOF DGM. This model was used in (Diehl et al, 2012) to introduce the condition monitoring approach discussed in the present research. The six rotational equations-of-motion, (61) through (66), are coupled to the six translational equations-of-motion, (67) through (72), by the two dynamic mesh forces, equation (73) and (74).

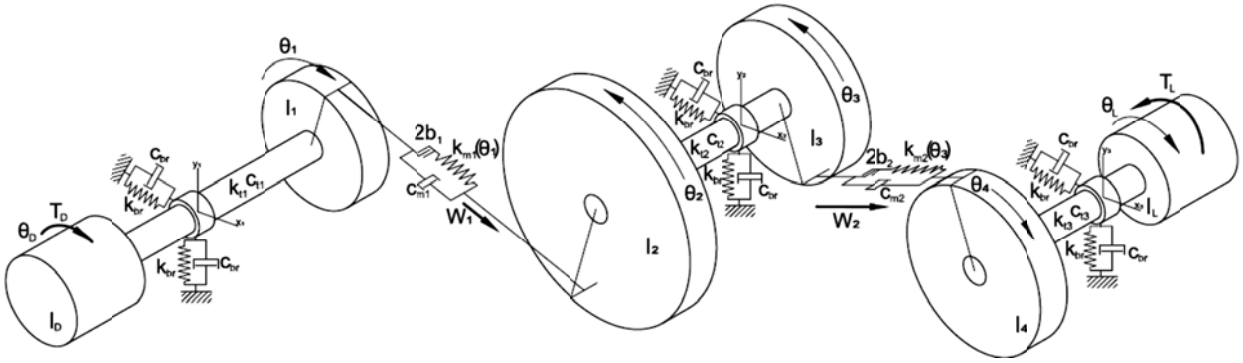

Figure 46. Two-Stage 12-DOF DGM

$$I_D\ddot{\theta}_D = \alpha \cdot T_D - c_{t1}(\dot{\theta}_D - \dot{\theta}_1) - k_{t1}(\theta_D - \theta_1) \quad (61)$$

$$I_1\ddot{\theta}_1 = -W_1R_1 + c_{t1}(\dot{\theta}_D - \dot{\theta}_1) + k_{t1}(\theta_D - \theta_1) \quad (62)$$

$$I_2\ddot{\theta}_2 = W_1R_2 - c_{t2}(\dot{\theta}_2 - \dot{\theta}_3) - k_{t2}(\theta_2 - \theta_3) \quad (63)$$

$$I_3\ddot{\theta}_3 = -W_2R_3 + c_{t2}(\dot{\theta}_2 - \dot{\theta}_3) + k_{t2}(\theta_2 - \theta_3) \quad (64)$$

$$I_4\ddot{\theta}_4 = W_2R_4 - c_{t3}(\dot{\theta}_4 - \dot{\theta}_L) - k_{t3}(\theta_4 - \theta_L) \quad (65)$$

$$I_L\ddot{\theta}_L = -T_L + c_{t3}(\dot{\theta}_4 - \dot{\theta}_L) + k_{t3}(\theta_4 - \theta_L) \quad (66)$$

$$m_1\ddot{x}_1 = -c\dot{x}_1 - kx_1 - W_1 \cdot \cos(15.5) \quad (67)$$

$$m_1\ddot{y}_1 = -c\dot{y}_1 - ky_1 + W_1 \cdot \sin(15.5) \quad (68)$$

$$m_2\ddot{x}_2 = -c\dot{x}_2 - kx_2 + W_1 \cdot \cos(15.5) - W_2 \cdot \cos(15.5) \quad (69)$$

$$m_2\ddot{y}_2 = -c\dot{y}_2 - ky_2 - W_1 \cdot \sin(15.5) - W_2 \cdot \sin(15.5) \quad (70)$$

$$m_3\ddot{x}_3 = -c\dot{x}_3 - kx_3 + W_1 \cdot \cos(15.5) \quad (71)$$

$$m_3\ddot{y}_3 = -c\dot{y}_3 - ky_3 + W_2 \cdot \sin(15.5) \quad (72)$$

$$W_1 = k_{m1}(\theta_1) \cdot DTE_1 + c_{m1}\left(R_1\dot{\theta}_1 - R_2\dot{\theta}_2\right) + cos(15.5)\,[k_{m1}(x_1 - x_2) + c_{m1}(\dot{x}_1 - \dot{x}_2)] - sin(15.5)\,[k_{m1}(y_1 - y_2) + c_{m1}(\dot{y}_1 - \dot{y}_2)] \quad (73)$$

$$W_2 = k_{m2}(\theta_3) \cdot DTE_2 + c_{m2}\left(R_3\dot{\theta}_3 - R_4\dot{\theta}_4\right) + cos(15.5)\,[k_{m2}(x_2 - x_3) + c_{m2}(\dot{x}_2 - \dot{x}_3)] + sin(15.5)\,[k_{m2}(y_2 - y_3) + c_{m2}(\dot{y}_2 - \dot{y}_3)] \quad (74)$$

By separating the bearing directions, accelerations found from solving the model are more comparable to the accelerometer orientations on the physical testbed. The data collected for this research was obtained from accelerometers placed on the forward bearing hub of the intermediate shaft in vertical and horizontal orientations. The drawback to this DGM is the unrealistic arrangement of having a single bearing per shaft; this is especially true of the intermediate shaft which is acted upon by both dynamic mesh forces but treated as if at one point. The testbed intermediate shaft is, of course, three dimensional, and the dynamic mesh forces act at different locations along the shaft length and cause motions at the bearings strongly influenced by location and proximity. It is therefore necessary to create separate bearings at each shaft end for improved comparisons to accelerometer motion. The result is a 26-DOF DGM described in the next section.

3.3.6. Twenty-Six Degree-of-Freedom Two Stage Dynamic Model Formulation.

The 26-DOF DGM shown in Figure 47 includes translational DOF representations of bearings at the each end of each shaft instead of a single bearing per shaft at each gear center as in the 12-DOF DGM. This model also includes vertical and horizontal motion at each gear. These additional DOFs allow shaft bending stiffness to be represented. The DOFs at the bearings can more closely represent the measured output of horizontally and vertically oriented accelerometers placed on the bearing housing of the gearbox testbed. Another benefit of the increased DOFs is the ability to represent shaft displacement at the gears for comparison to proximity probes installed in the gearbox. This 26-DOF DGM was used in (Diehl and Tang, 2016) to demonstrate the ability of the condition monitoring approach discussed in the present research to characterize a missing gear tooth fault in non-stationary operation.

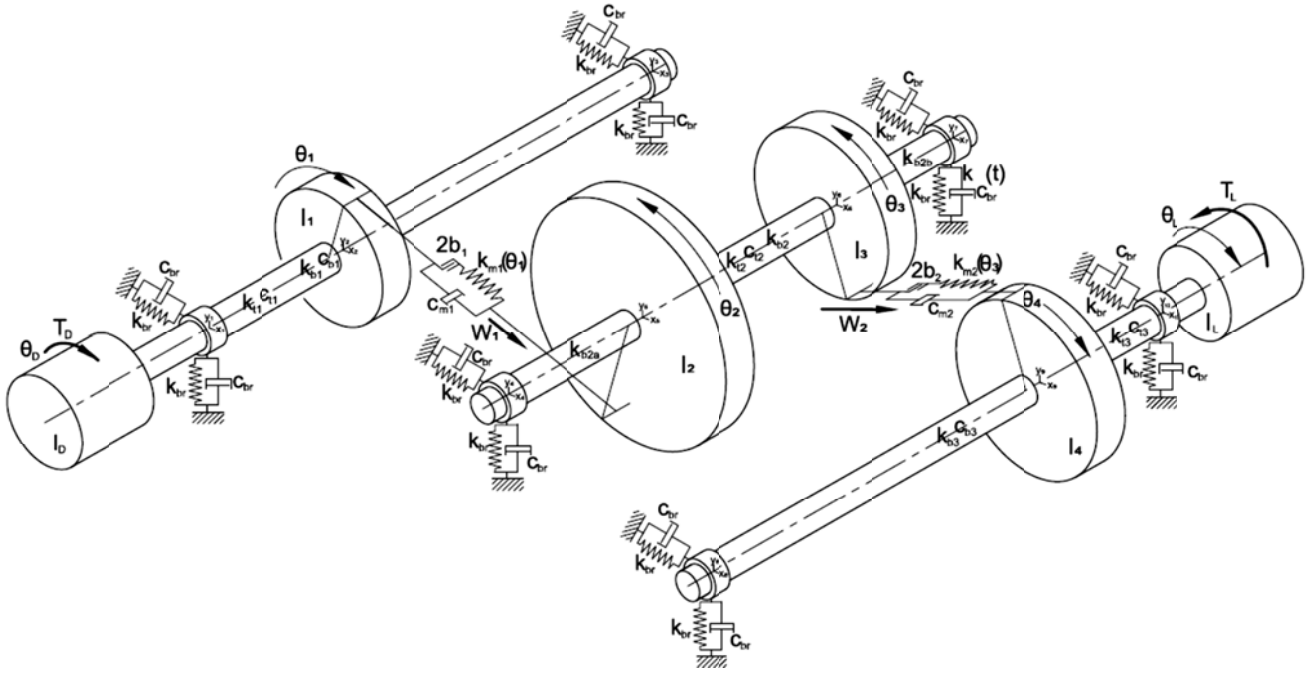

Figure 47. Two Stage 26-DOF Model

A necessary complication of including bearings at each shaft end is balancing the dynamic mesh forces, bearing reaction forces and shaft stiffness on the intermediate shaft. This issue is explained in more detail in Chapter 2 in the section discussing shaft bending stiffness.

The 26-DOF DGM is mathematically represented by the six rotational equations-of-motion, (75) through (80),and twenty translational equations-of-motion, (81) through (100), which are coupled by the two dynamic mesh forces, equation (101) and (102).

Equations of rotational DOFs are as follows:

$$I_D\ddot{\theta}_D = \alpha \cdot T_D - c_{t1}\left(\dot{\theta}_D - \dot{\theta}_1\right) - k_{t1}(\theta_D - \theta_1) \tag{75}$$

$$I_1\ddot{\theta}_1 = -W_1R_1 + c_{t1}\left(\dot{\theta}_D - \dot{\theta}_1\right) + k_{t1}(\theta_D - \theta_1) \tag{76}$$

$$I_2\ddot{\theta}_2 = W_1R_2 - c_{t2}\left(\dot{\theta}_2 - \dot{\theta}_3\right) - k_{t2}(\theta_2 - \theta_3) \tag{77}$$

$$I_3\ddot{\theta}_3 = -W_2R_3 + c_{t2}\left(\dot{\theta}_2 - \dot{\theta}_3\right) + k_{t2}(\theta_2 - \theta_3) \tag{78}$$

$$I_4\ddot{\theta}_4 = W_2R_4 - c_{t3}\left(\dot{\theta}_4 - \dot{\theta}_L\right) - k_{t3}(\theta_4 - \theta_L) \tag{79}$$

$$I_L\ddot{\theta}_L = -T_L + c_{t3}\left(\dot{\theta}_4 - \dot{\theta}_L\right) + k_{t3}(\theta_4 - \theta_L) \tag{80}$$

Equations of the translational DOFs are as follows:

$$m_1\ddot{x}_1 = -c\dot{x}_1 - kx_1 - k_{b1}(x_1 - x_2) \tag{81}$$

$$m_1\ddot{y}_1 = -c\dot{y}_1 - ky_1 - k_{b1}(y_1 - y_2) \tag{82}$$

$$m_2\ddot{x}_2 = +k_{b1}(x_1 - x_2) - k_{b1}(x_2 - x_3) + W_1 \cdot \cos(15.5) \tag{83}$$

$$m_2\ddot{y}_2 = +k_{b1}(y_1 - y_2) - k_{b1}(y_2 - y_3) - W_1 \cdot \sin(15.5) \tag{84}$$

$$m_3\ddot{x}_3 = -c\dot{x}_3 - kx_3 + k_{b1}(x_2 - x_3) \tag{85}$$

$$m_3\ddot{y}_3 = -c\dot{y}_3 - ky_3 + k_{b1}(y_2 - y_3) \tag{86}$$

$$m_4\ddot{x}_4 = -c\dot{x}_4 - kx_4 - k_{b2a}(x_4 - x_5) \tag{87}$$

$$m_4\ddot{y}_4 = -c\dot{y}_4 - ky_4 - k_{b2a}(y_4 - y_5) \tag{88}$$

$$m_5\ddot{x}_5 = -k_{b2}(x_5 - x_6) + k_{b2a}(x_4 - x_5) - W_1 \cdot \cos(15.5) \tag{89}$$

$$m_5\ddot{y}_5 = -k_{b2}(y_5 - y_6) + k_{b2a}(y_4 - y_5) + W_1 \cdot \sin(15.5) \tag{90}$$

$$m_6\ddot{x}_6 = +k_{b2}(x_5 - x_6) - k_{b2b}(x_6 - x_7) - W_2 \cdot \cos(15.5) \tag{91}$$

$$m_6\ddot{y}_6 = +k_{b2}(y_5 - y_6) - k_{b2b}(y_6 - y_7) - W_2 \cdot \sin(15.5) \tag{92}$$

$$m_7\ddot{x}_7 = -c\dot{x}_7 - kx_7 + k_{b2b}(x_6 - x_7) \tag{93}$$

$$m_7\ddot{y}_7 = -c\dot{y}_7 - ky_7 + k_{b2b}(y_6 - y_7) \tag{94}$$

$$m_8\ddot{x}_8 = -c\dot{x}_8 - kx_8 - k_{b3}(x_8 - x_9) \tag{95}$$

$$m_8\ddot{y}_8 = -c\dot{y}_8 - ky_8 - k_{b3}(y_8 - y_9) \tag{96}$$

$$m_9\ddot{x}_9 = +k_{b3}(x_8 - x_9) - k_{b3}(x_9 - x_{10}) + W_2 \cdot \cos(15.5) \tag{97}$$

$$m_9\ddot{y}_9 = +k_{b3}(y_8 - y_9) - k_{b3}(y_9 - y_{10}) + W_2 \cdot \sin(15.5) \tag{98}$$

$$m_{10}\ddot{x}_{10} = -c\dot{x}_{10} - kx_{10} + k_{b3}(x_9 - x_{10}) \tag{99}$$

$$m_{10}\ddot{y}_{10} = -c\dot{y}_{10} - ky_{10} + k_{b3}(y_9 - y_{10}) \tag{100}$$

$$W_1 = k_{m1}(\theta_1) \cdot DTE_1 + c_{m1}\left(R_1\dot{\theta}_1 - R_2\dot{\theta}_2\right) + cos(15.5)\,[k_{m1}(x_2 - x_5) + c_{m1}(\dot{x}_2 - \dot{x}_5)] - sin(15.5)\,[k_{m1}(y_2 - y_5) + c_{m1}(\dot{y}_2 - \dot{y}_5)] \quad (101)$$

$$W_2 = k_{m2}(\theta_3) \cdot DTE_2 + c_{m2}\left(R_3\dot{\theta}_3 - R_4\dot{\theta}_4\right) + cos(15.5)\,[k_{m2}(x_6 - x_9) + c_{m2}(\dot{x}_6 - \dot{x}_9)] + sin(15.5)\,[k_{m2}(y_6 - y_9) + c_{m2}(\dot{y}_6 - \dot{y}_9)] \quad (102)$$

3.3.7. Two-Stage Dynamic Gear Model Solution Method.

The same solution method employed for the single-stage DGMs, namely Runge Kutta time marching, is used for the two-stage DGM. The two-stage DGMs are written as MATLAB code functions with a call-out function for the 1st stage time-varying- mesh stiffness which is modified to include different fault models when appropriate. A separate mesh stiffness call-out function is used for the 2nd stage. The two-stage DGM is used to simulate non-stationary operation in this research, so the torque factor applied within the DGM code calls out to a torque factor function which changes the torque balance thereby accelerating or decelerating the model speed. The DGMs are solved using 20 kHz time steps which match the experimental data sampling rate.

As in the single-stage DGMs, matrix versions of the two-stage DGM equations-of-motion are used to (1) find initial displacements due to the torque load, (2) obtain eigenvalues/natural frequencies of the model, and (3) compare and/or trouble-shoot the linearized DGM with a modal space solution of the matrix version.

The natural frequencies found from the matrix code for all of the two-stage DGMs discussed are summarized in Table 12. Similar to the single-stage DGM natural frequency comparisons, the incrementally increasing DOF models assist in identifying or associating frequencies with modeled features. Again, the first natural frequency of mode is zero due to rotational rigid body motion. The 2nd and 3rd natural frequencies of the 3-DOF DGM are associated with the mesh stiffness and shift to the 4th and 5th natural frequencies of the 6-DOF DGM, implying that the shafts are relatively flexible and/or the drive and load relatively large inertia. These two frequencies appear to shift to the 7th and 8th natural frequencies in the 9-DOF DGM and then split to the 7th and 9th in the alternative 9-DOF DGM. They

appear in the 10th and 11th natural frequencies in the 12-DOF, but are more difficult to estimate in 26-DOF where many other frequencies appear in the same range. Additional analyses were performed to identify associated parameters with natural frequencies by changing values of stiffness and comparing results. This technique was used as a tool to troubleshoot as well as tune the model during parametric development.

Table 12. Natural Frequencies of Two-stage DGMs based on UConn SDSL Testbed

Mode	3-DOF	6-DOF	9-DOF	9a-DOF	12-DOF	26-DOF
1	0	0	0	0	0	0
2	2,377	540	521	1,391	531	75
3	4,334	1,060	946	1,628	1,021	117
4		2,237	1,200	1,868	1,613	677
5		4,273	1,396	2,080	1,759	744
6		6,271	1,466	2,108	1,962	841
7			2,239	2,344	1,972	859
8			4,826	3,387	2,004	882
9			6,721	4,932	2,054	901
10					2,242	2,150
11					4,878	2,260
12					6,737	2,320
13						2,820
14						2,820
15						3,620
16						3,870
17						3,870
18						4,430
19						4,460
20						4,480
21						4,660
22						5,430
23						5,630
24						5,740
25						6,070
26						8,250

3.4. Two-Stage Model Validation with Constant Speed Experimental Data

The following section serves to validate the various DOF models using collected data from the testbed run at constant speed as well as to evaluate the effect of the number of DOF. Since the most damage detection methods are performed on machinery running at constant speeds, comparing healthy and faulty model results and testbed data at constant speed is considered a logical means of validation. The various DOF DGMs are solved for a short duration while running at a constant 820 rpm and loaded at 6.6 Nm to match gearbox test data collected at those conditions. Both healthy and missing tooth fault are modeled and measured for comparison.

Plots of accelerometer data and model acceleration versus time are shown in Figure 48 for healthy and damaged gear (missing tooth) conditions. While the acceleration magnitude range is not the same, the relative increase in magnitude due to the fault and the fault duration are quite similar. The shape of the blip, which is likely an impulse due to the fault, is also similar. The presence of noise in the signal and likelihood of variation make this a somewhat anecdotal comparison, yet still informative.

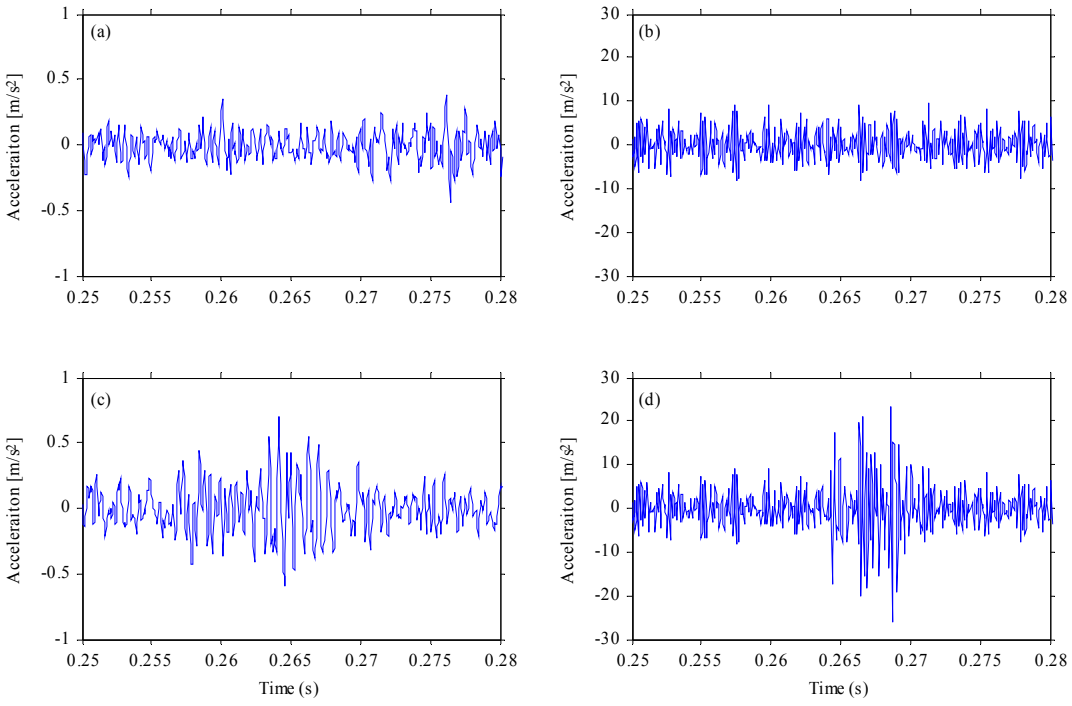

Figure 48. Experimental data and model results for 820 rpm constant speed test: (a) healthy data, (b) healthy model, (c) missing tooth data, and (d) missing tooth model.

When the experimental data and model results are processed with a basic spectrum analysis (i.e., FFT), the Gear Mesh Frequencies (GMF) equal to the shaft speed times number of teeth are expected to be produced (Scheffer and Girdhar, 2004). As such, the first stage gear mesh frequency (GMF1) is expected to be 437 Hz and the second stage gear mesh frequency (GMF2) 262 Hz. These expected frequencies and their integer multiples are listed in Table 13.

Table 13. Expected frequencies (Hz) from gearbox operating at 820 r/min.

Δ GMF[a]	GMF2 ②	GMF1 ①	2x GMF2	GMF1 + Δ GMF	3x GMF2	2x GMF1	4x GMF2	3x GMF1 and 5x GMF2	4x GMF1
175	262	437	525	612	787	875	1050	1312	1750

GMF: gear mesh frequency
[a]The difference between gear mesh frequency of the first and second gear pairs.

The spectrum results of unfiltered experimental data and various DOF DGM results are presented in Figures 49 through 54. Peak frequencies are labeled and show many of the same frequency changes and features indicating gear damage.

While simple models are desirable because they are solved more quickly, the number of DOFs affects the frequency content and relative frequency magnitudes as seen in these spectrum plots. It is also desirable to have DOFs within the models that are closely analogous to the positions, motions and directions of the measured locations of the physical gearbox. Additionally, for the purposes of this research, GMF1 and multiples are prioritized since the first stage pinion is the location of the seeded faults and therefore the frequencies of expected changes.

The spectrum plot of the 3 -DOF DGM shown in Figure 49 is based on the rotation of the intermediate shaft. The 4^{th} multiple of GMF1 of this model is exaggerated compared to the other frequencies below 2000 Hz, and GMF2 frequencies are barely present. The fewer DOFs lack the flexibility to respond to the second stage meshing forces which are smaller than the first stage dynamic mesh forces since the second stage mesh stiffness is less. The 6-DOF DGM adds shaft flexibility and additional rotational inertias which results in more frequency content than the 3-DOF DGM as shown in

Figure 20, including exaggerated 4th multiple of GMF2 rather than the 4th multiple of GMF1. Both the 9-DOF (Figure 51) and alternative 9-DOF (Figure 22) DGMs have translational DOFs which more closely reflect the physical motion of the accelerometers than the purely rotational DGMs. The 9-DOF DMGs also show relative frequency distributions more similar to the measured frequency distribution, with the exception of exaggerated 2nd multiple of GMF2. The 12-DOF DGM in Figure 53 shows reduced 2xGMF2 and increased 3xGMF2, 2xGMF1, 4xGMF2 and 3xGMF1 content. The 26-DOF DGM in Figure 24 captures the large 3xGMF2 and 2xGMF1 found in the actual data, as well as reducing 2xGMF2 which is also closer to the actual data. As noted, the key frequencies for this investigation are multiples of GMF1, especially 2xGMF1 and 3xGMF1. These are captured by the 26-DOF DGM as are the prominent GMF2 frequencies. There remain some frequencies out of proportion in the 26-DOF DGM, especially in high frequencies. An interesting but unusable result was achieved when the shaft bending stiffnesses were magnified by several orders of magnitude. The frequency distributions were much closer to the actual measured data, but the models were extremely "stiff" and incredibly slow to solve. This is an area worthy of further investigation into other numerical solution methods and strategies for increasing solution speeds. For this investigation the 26-DOF DGM is considered sufficiently complex to capture the dynamic behavior of the physical gearbox and, as will be demonstrated, a platform for gear fault models.

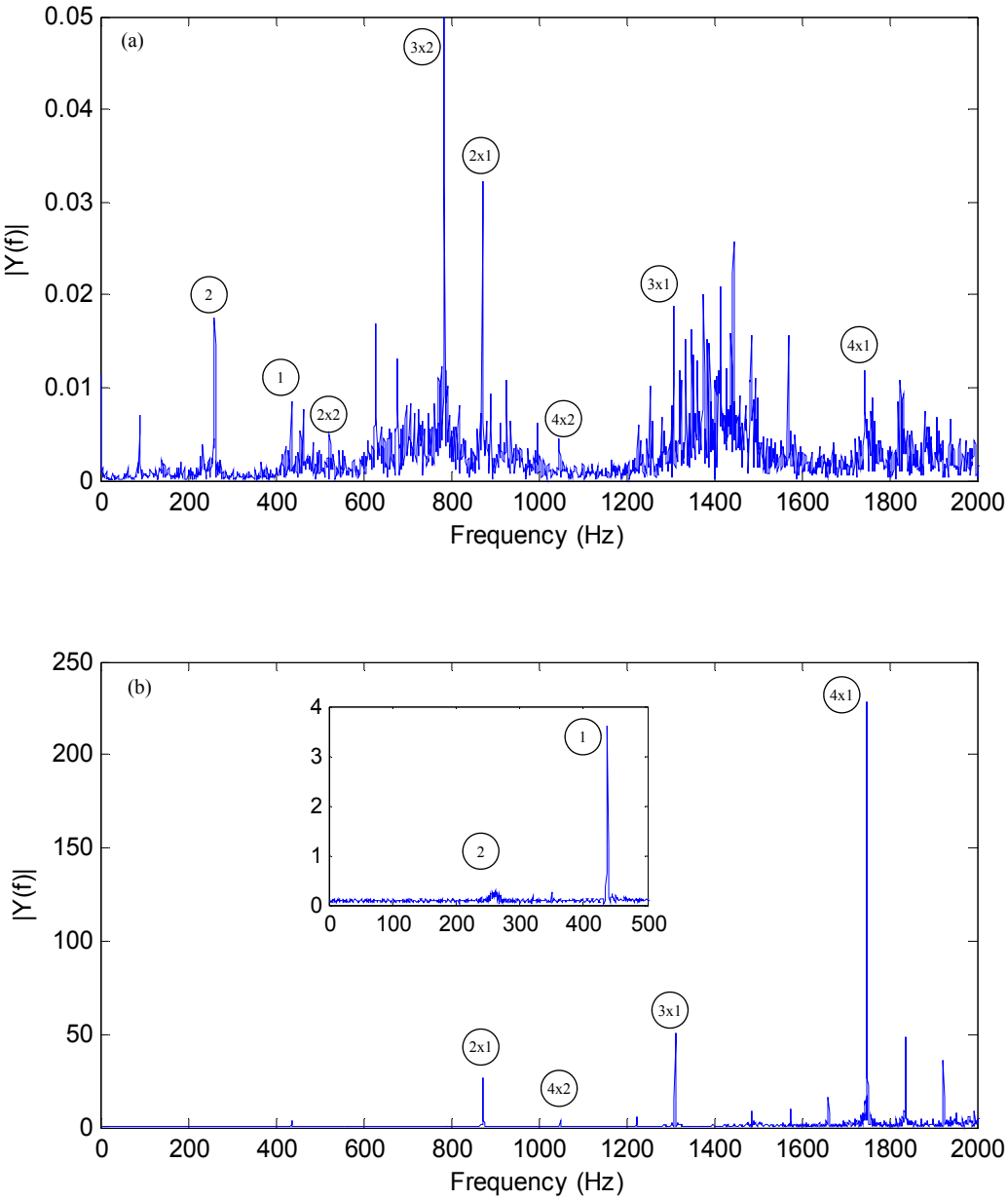

Figure 49. Spectrum analysis of experimental data and 3 DOF DGM results for 820 rpm constant speed test: (a) healthy data,(b) healthy model. ① - 1st stage gear mesh frequency, ② - 2nd stage gear mesh frequency.

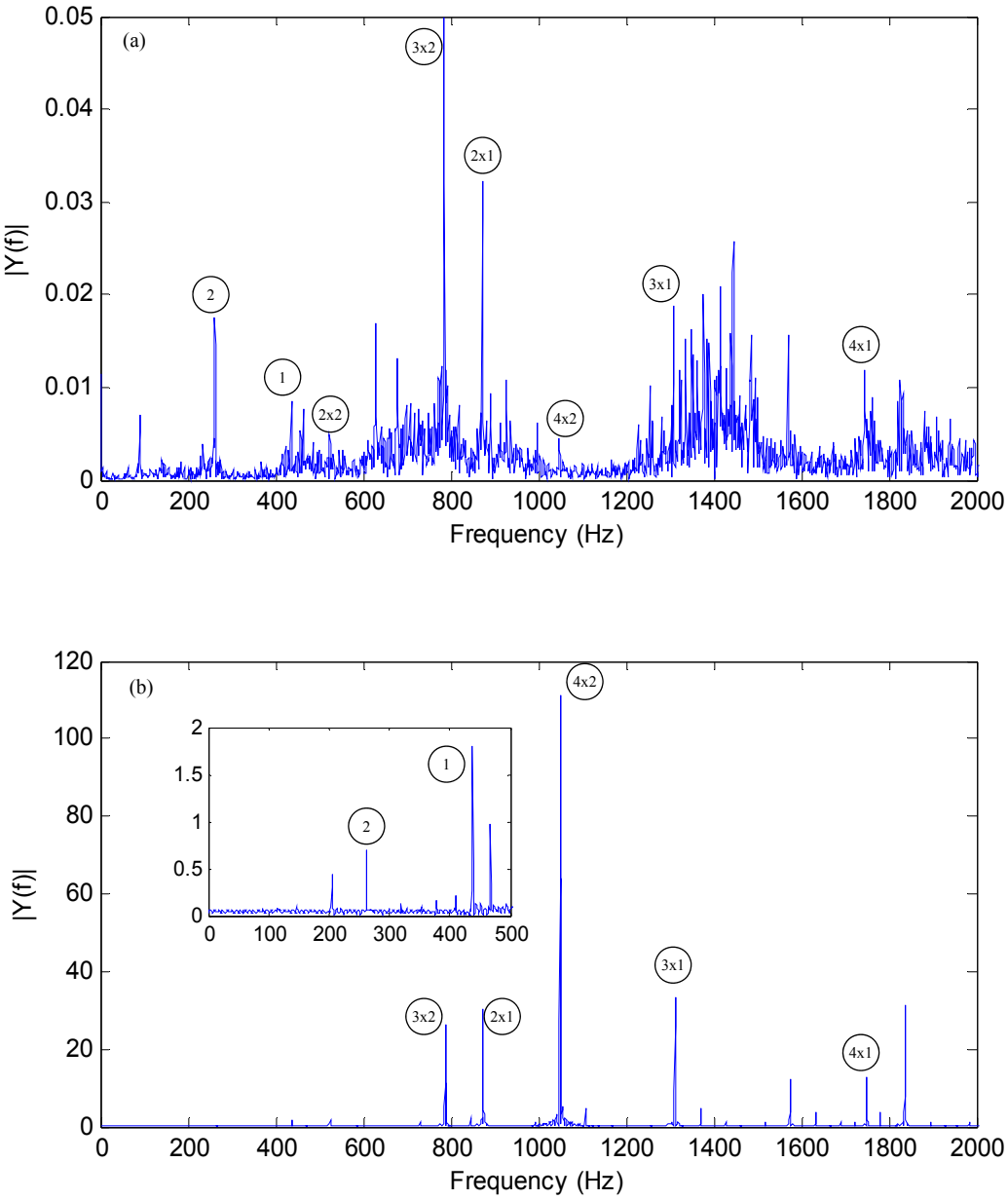

Figure 50. Spectrum analysis of experimental data and 6 DOF DGM results for 820 rpm constant speed test: (a) healthy data,(b) healthy model. ① - 1st stage gear mesh frequency, ② - 2nd stage gear mesh frequency.

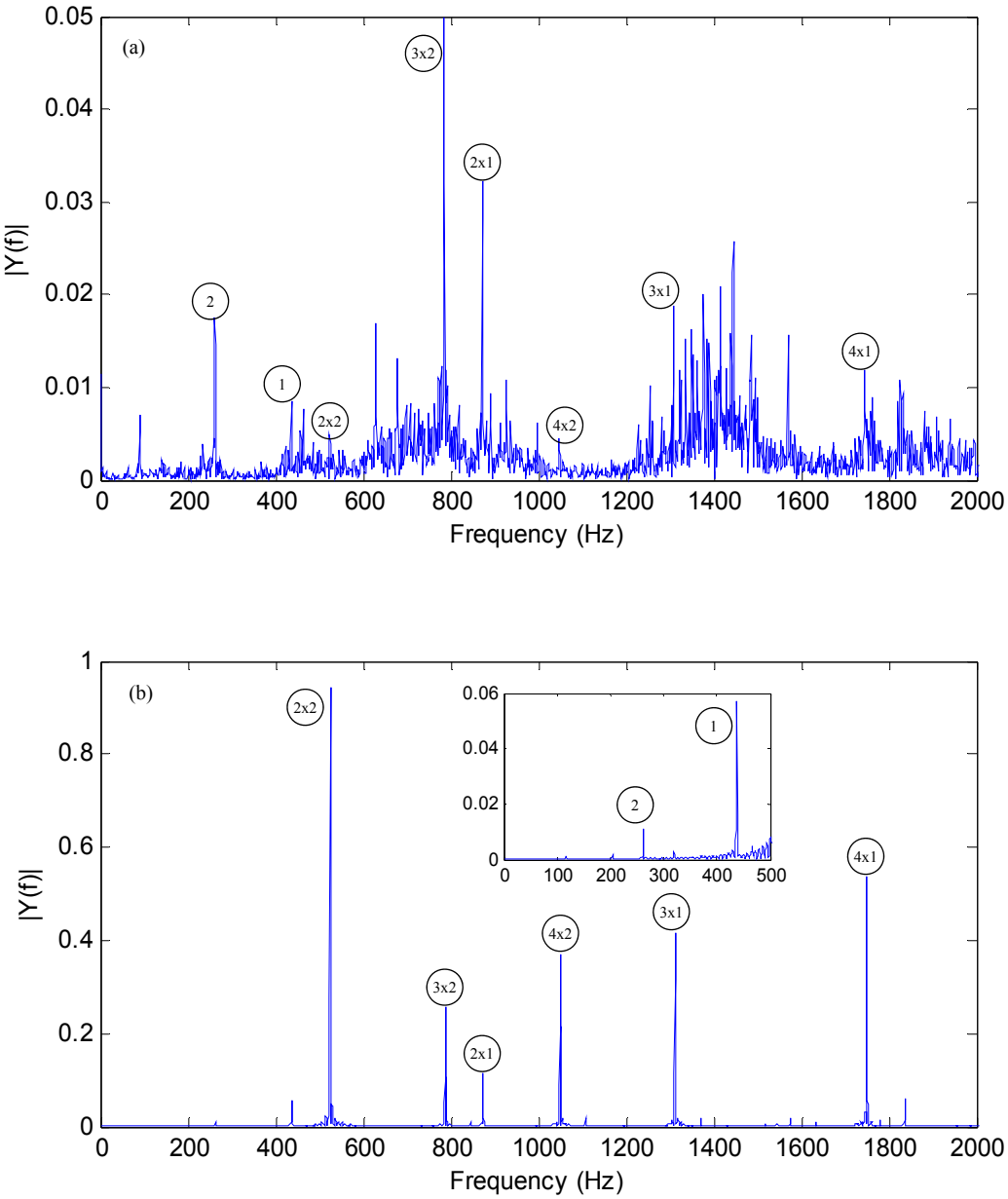

Figure 51. Spectrum analysis of experimental data and 9 DOF DGM results for 820 rpm constant speed test: (a) healthy data,(b) healthy model. ① - 1st stage gear mesh frequency, ② - 2nd stage gear mesh frequency.

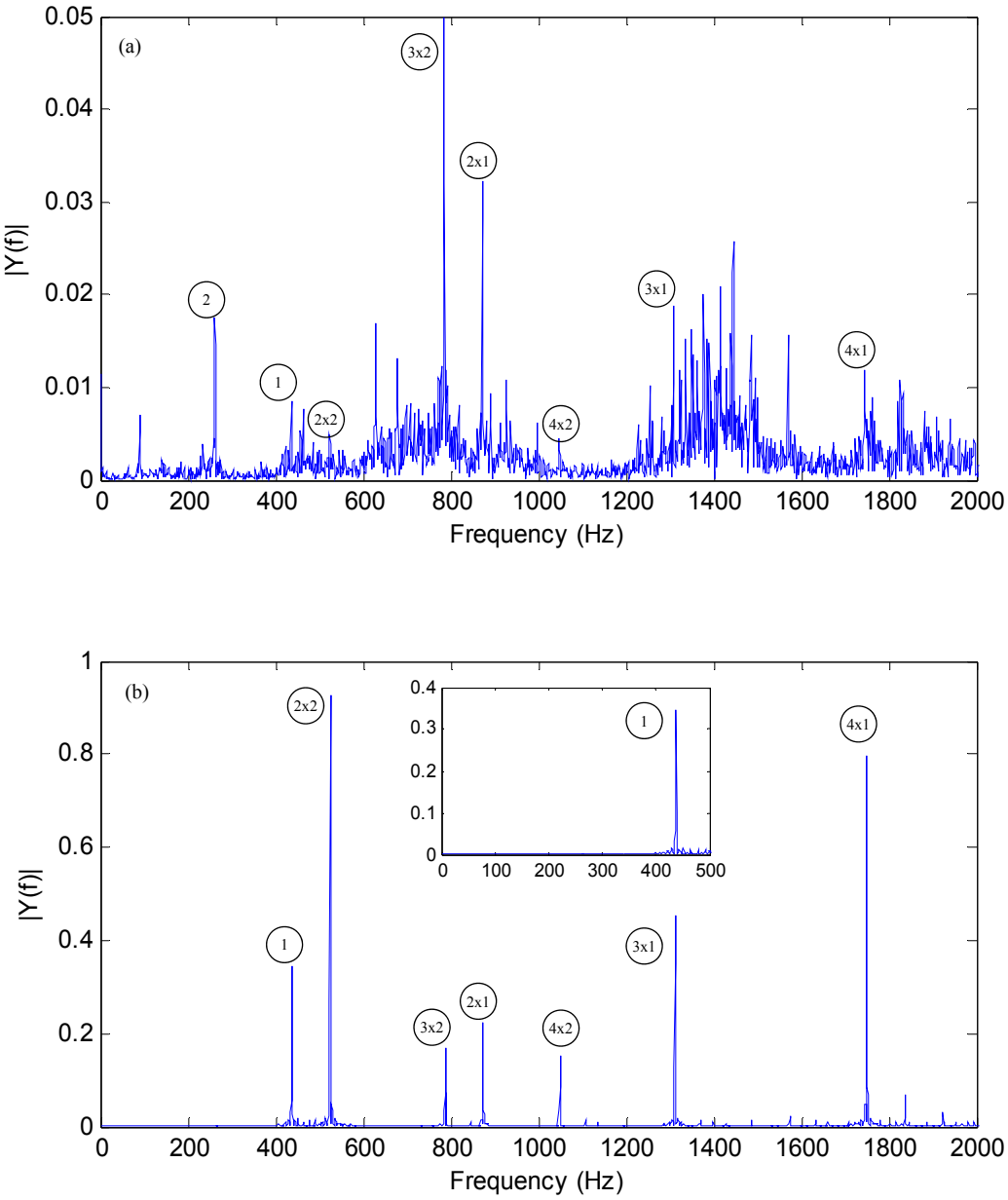

Figure 52. Spectrum analysis of experimental data and alternative 9 DOF DGM results for 820 rpm constant speed test: (a) healthy data,(b) healthy model. ① - 1st stage gear mesh frequency, ② - 2nd stage gear mesh frequency.

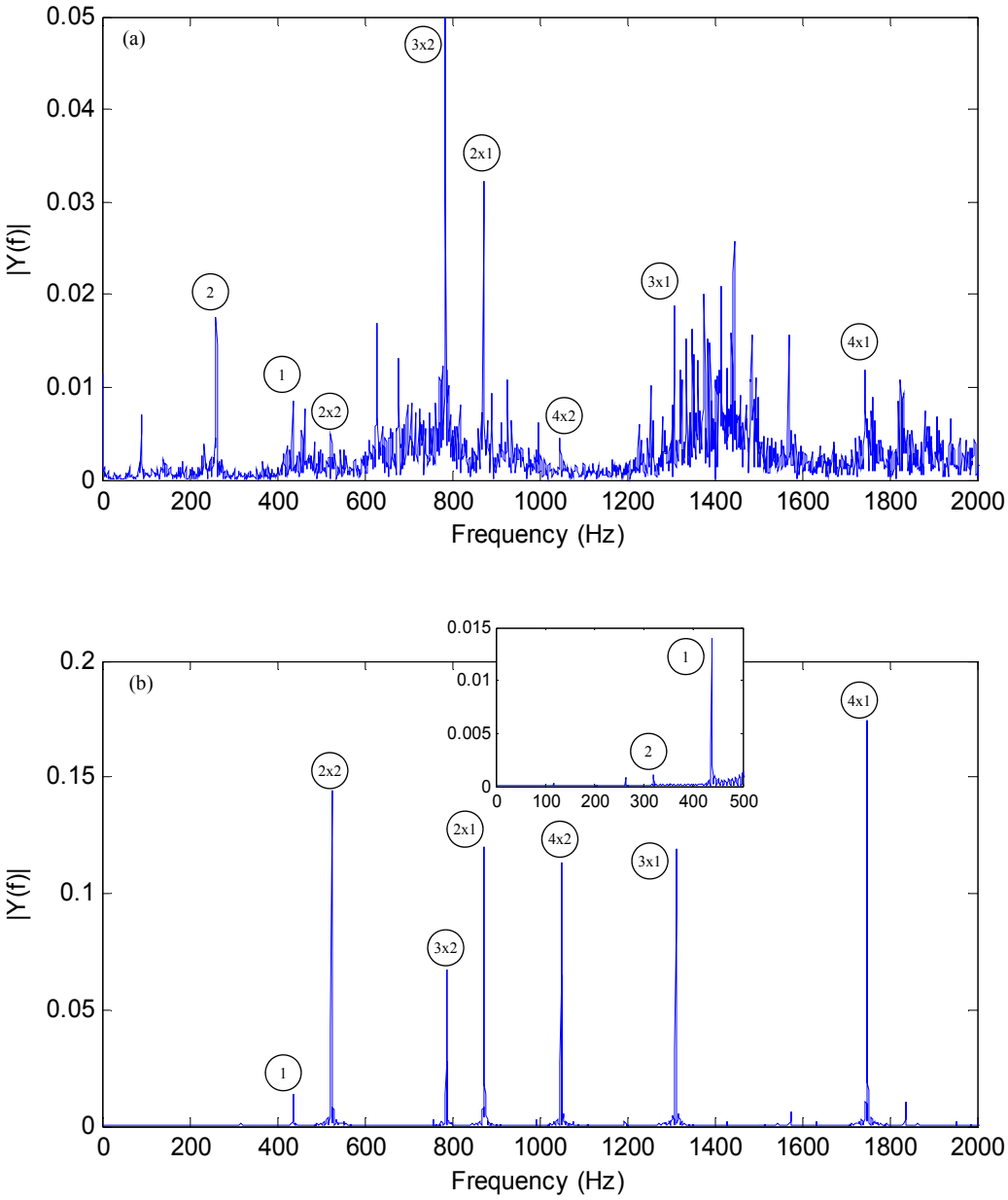

Figure 53. Spectrum analysis of experimental data and 12 DOF DGM results for 820 rpm constant speed test: (a) healthy data,(b) healthy model. ① - 1st stage gear mesh frequency, ② - 2nd stage gear mesh frequency.

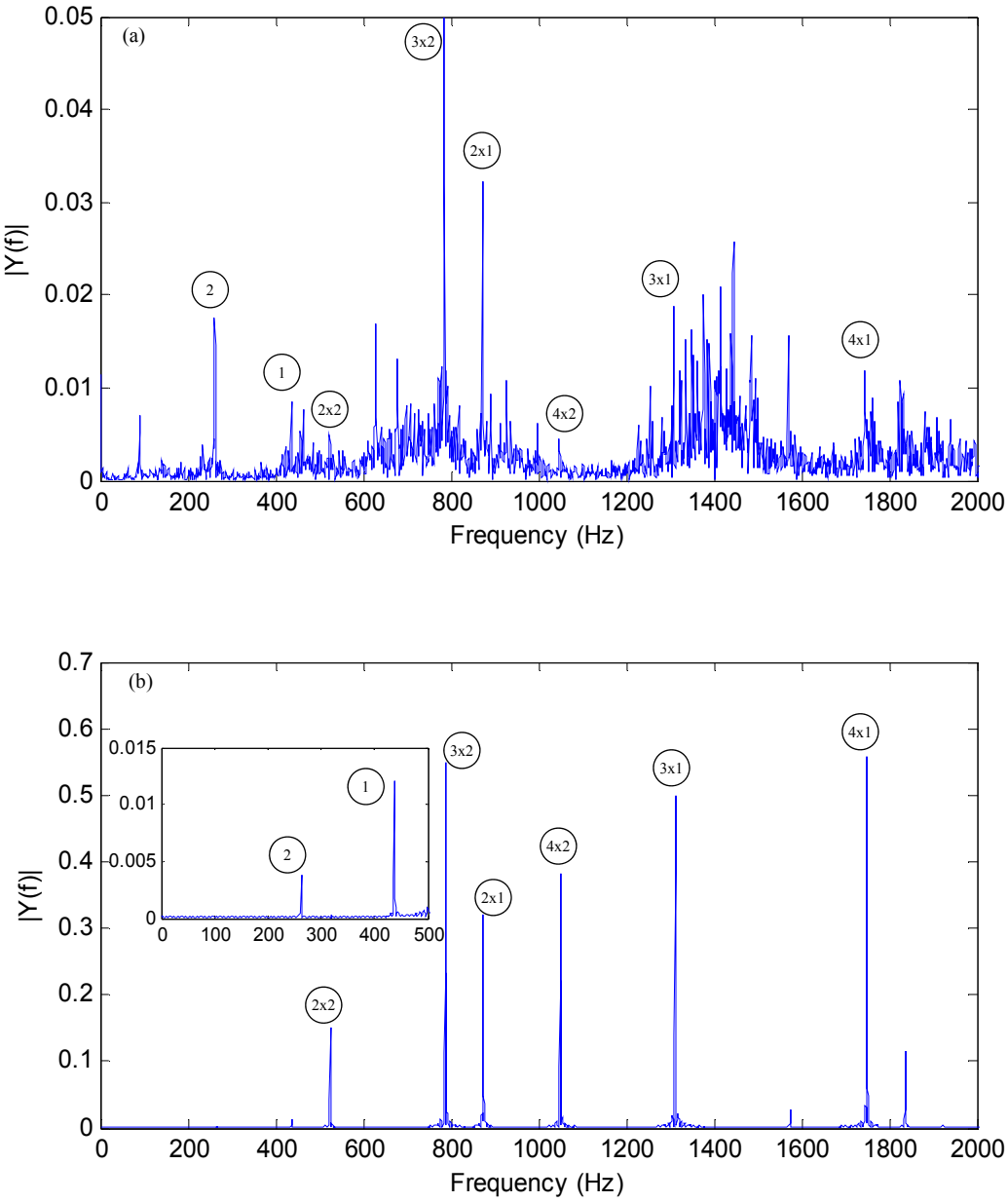

Figure 54. Spectrum analysis of experimental data and 26 DOF DGM results for 820 rpm constant speed test: (a) healthy data,(b) healthy model. ① - 1st stage gear mesh frequency, ② - 2nd stage gear mesh frequency.

To demonstrate one of the fault models described in Chapter 2, test data with a seeded fault (missing tooth) in first stage pinion and operating at the same constant speed conditions used above were recorded and compared to the 26 DOF model results with modeled missing tooth fault. The spectrum results of unfiltered experimental data and model results are presented in Figure 55. Peak frequencies are labeled and show many of the same frequency changes and features indicating gear damage.

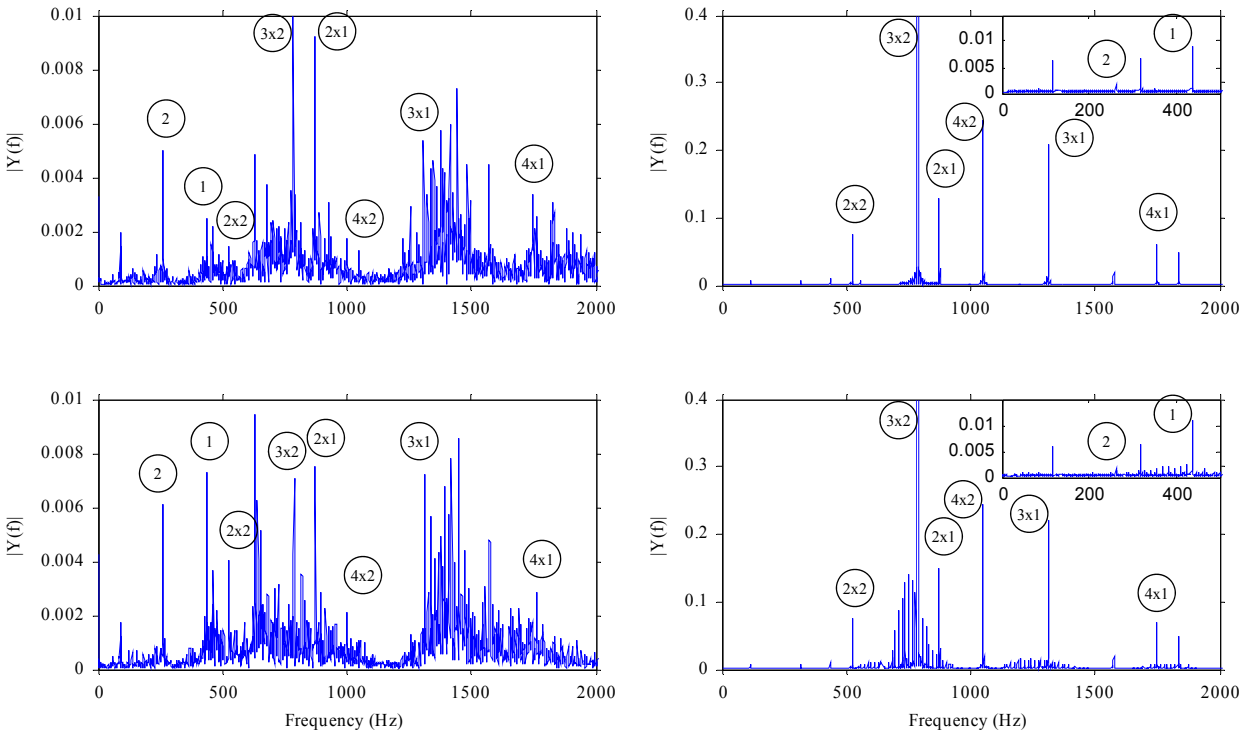

Figure 55. Spectrum analysis of experimental data and model results for 820 rpm constant speed test: (a) healthy data,(b) healthy model, (c) damaged (missing tooth) data, and (d) damaged model. ① - 1st stage gear mesh frequency, ② - 2nd stage gear mesh frequency.

The two primary fault indicators in a gear system spectrum analysis are the increased magnitude at multiples of the gear mesh frequency and the sideband prevalence near the primary gear mesh frequencies and integer multiples (Randall, 1982). The expected magnitude increase at the gear mesh frequencies and multiples, as well as the presence of side-band frequency content, are present in both test and model results. These frequency plots, while validating that the model captures many of the effects of gear damage, also reaffirm the difficulty achieving perfect agreement between the data and model. Many of

the peaks are disproportionate, with the low frequency content being particularly under-represented in the model, requiring a zoomed window to show this detail. In spite of these shortcomings, this data and model comparison demonstrates the ability of the DGM to capture the behavior of the physical gearbox and represent a damaged gear.

Chapter 4 – Signal Processing with the Harmonic Wavelet Transform

Condition monitoring of rotating machinery has historically been performed on machines operating at constant speeds by processing vibration data with the fast Fourier transform (FFT) into the frequency domain. Nevertheless, FFT and other frequency-domain techniques are not well suited for analyzing non-stationary signals such as machinery with changing speeds (Peng and Chu, 2004). One important example is the operation of a wind turbine whose rotational speed is, in part, dependent on wind speed. The non-stationary complication can be overcome by remaining in the time-domain or by applying time-frequency techniques (Jardine et al, 2006; Lee et al, 2014; Kan et al, 2015). Time-frequency domain analysis reveals the waveform energy distribution across both time and frequency, and can be useful to identify transient events as well as fault patterns. Examples of time-frequency distribution techniques are the short-time Fourier Transform (STFT), Wigner–Ville distribution (WVD) and wavelet transforms (WT). The STFT segments a signal into discrete time windows to find the frequency content in that window, but window size limits the resolution, making STFT only effective for analysis on slowly changing non-stationary signals (Jardine et al, 2006). While WVD does not segment time as STFT, it is susceptible to interference between "cross terms" that can cause misleading results (Peng and Chu, 2004). WT is conceptually similar to FFT except localized functions, called "mother wavelets", are used instead of sinusoidal functions, allowing the time of an event to be retained. Wavelets are useful in condition monitoring for their ability to characterize frequency and time content within a signal to find faults in rotating equipment as documented in (Heng et al, 2009; Omar et al, 2012; Yan et al, 2014).

Among mother wavelets, the Harmonic Wavelet Transform (HWT) (Newland, 1993) in particular is well suited for analyzing gear vibration since it is similar to the natural occurring structure of vibration waves (Bonel-Cerdan and Nikolajsen, 1997; Liu et al, 1997; Newland, 1999; Yen and Lin, 2000). The HWT mother wavelet is derived in a manner which makes it a logical choice for analyzing vibration signals. Additionally, HWT has shown promise in identifying faults in non-stationary gear vibration signals (Samuel et al, 2000; Lu et al, 2012). What follows is the analysis of both experimental test data

and DGM results to demonstrate how these two methods can be used in conjunction to identify gear fault types as well as gear fault severity in non-stationary gearboxes.

4.1 Harmonic Wavelet Transform Background

Newland introduced the Harmonic Wavelet Transform (HWT) which has several advantages over other wavelets in capturing frequency and time content (Newland, 1993). One of the main advantages arises from the derivation that begins in the frequency domain as a step function, so the bandwidth of each wavelet is well defined. Equation 1 and Figure 56 present the band limited step function in the frequency domain, where m and n define the band limits.

$$W_{m,n}(\omega) = \begin{cases} \frac{1}{2\pi(n-m)} & for\ m(2\pi) \le \omega < n(2\pi), \\ 0 & \text{elsewhere} \end{cases} \quad (1)$$

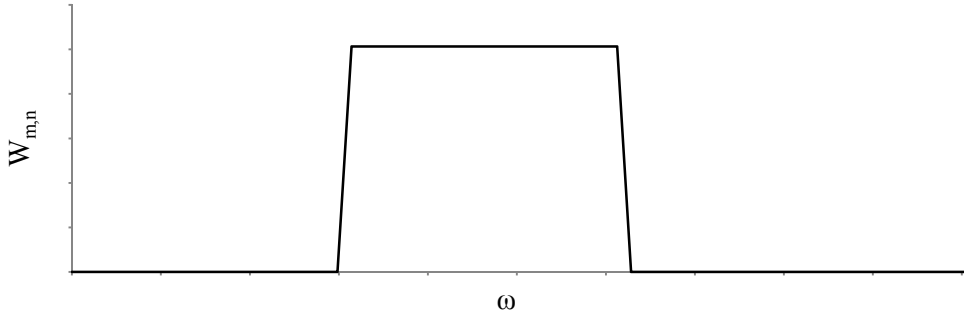

Figure 56. Harmonic Wavelet in the Frequency Domain

Transforming this step wave from the frequency domain to the time domain creates the harmonic wavelet expressed in Equation 2, where the integer k is the translational parameter, and plotted for example values of m and n in Figure 57.

$$w_{mnk}(t) = \frac{e^{in2\pi\left(t-\frac{k}{n-m}\right)} - e^{im2\pi\left(t-\frac{k}{n-m}\right)}}{(n-m)i2\pi t} \quad (2)$$

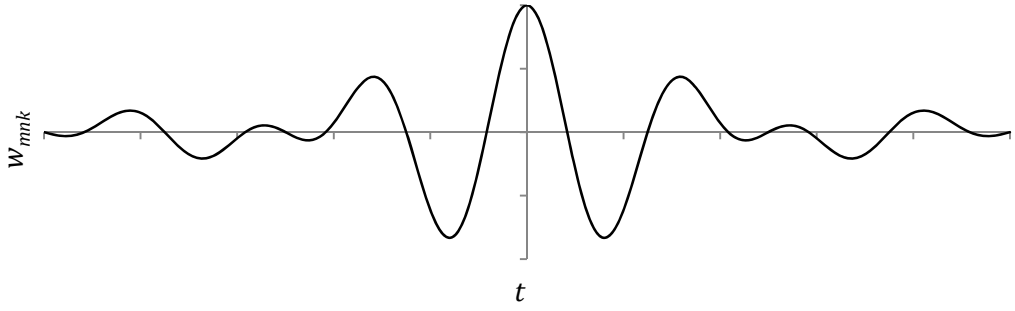

Figure 57. Harmonic Wavelet in the Time Domain

Another advantage of the HWT over other wavelet transforms is the relative ease in its implementation, since it can be constructed with an algorithm which uses the Fast Fourier Transform (FFT) and Inverse Fast Fourier Transform (IFF). Figure 58 presents a schematic of Newland's algorithm.

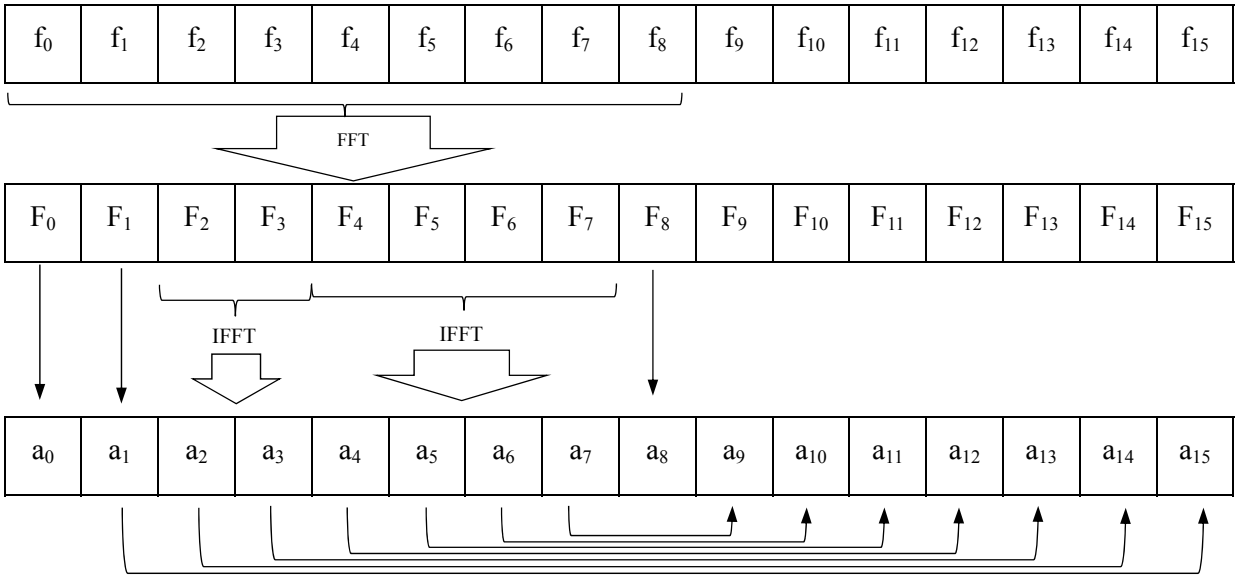

Figure 58. Schematic of HWT Algorithm

Because HWT are formed in the frequency domain, there is minimal leakage between frequency bands. Effective HWT implementation simply requires the choice of bandwidths (levels) that will efficiently represent the desired features. This is not necessarily an easy or universal choice. The

resolutions of time and frequency are always compromises in time-frequency analyses due to the uncertainty principle. The division of frequency and time, or "partition," does not necessarily need to form a specific pattern (Newland, 1994), but a consistent partition between analyses is needed to make detailed comparisons. In this analysis several different resolutions are discussed and used to search for gear faults. For the 4 seconds of 20kHz data, partitions based on 12.5 Hz frequency resolution and 0.08 seconds time resolution (referred to as 800x50), 25 Hz 0.04 seconds (referred to as 400x100), and 100 Hz and 0.01 seconds (referred to as 100x400) are demonstrated. The 800x50 and 100x400 resolutions were selected to analyze a portion of the operating profile where the shaft speed approaches 25Hz, causing sideband spacing at 25 Hz and fault impacts at 0.04 second intervals; the first resolution is necessary to reveal sidebands in the frequency and the second to reveal the occurrence of fault impacts.

4.2 Harmonic Wavelet Transform Implementation.

The output of a signal processed with HWT is a matrix of coefficients arranged with time columns and frequency rows, where the magnitude of each coefficient represents the signal energy. A contour plot of this matrix of coefficients is used to visualize the distribution of energy with time and frequency. When applied to the vibration of a non-stationary gear set, the HWT contour plot is expected to contain energy concentrated along regions that are multiples of the gear mesh frequency.

Figure 59 shows color contour plots, or *wavelet maps*, of the HWT coefficients for the constant speed tests previously shown in the two-stage DGM validation section, with test data and DGM results for healthy and missing tooth fault. HWT is applied to the 4 second constant speed tests with the 400x100 partition which creates a 400 row, 100 column matrix of coefficients. Wavelet maps indicate the energy distribution with frequency on the vertical axis and time on the horizontal axis. A contour color scale was chosen so white-to- blueish colors represent regions of low energy and reddish-to-black regions represent higher energy. The magnitude of the coefficients was adjusted to use the same contour scales for both processed data and model results. The fault's influence on the vibration in both time and frequency is easily recognizable, especially in the DGM simulation.

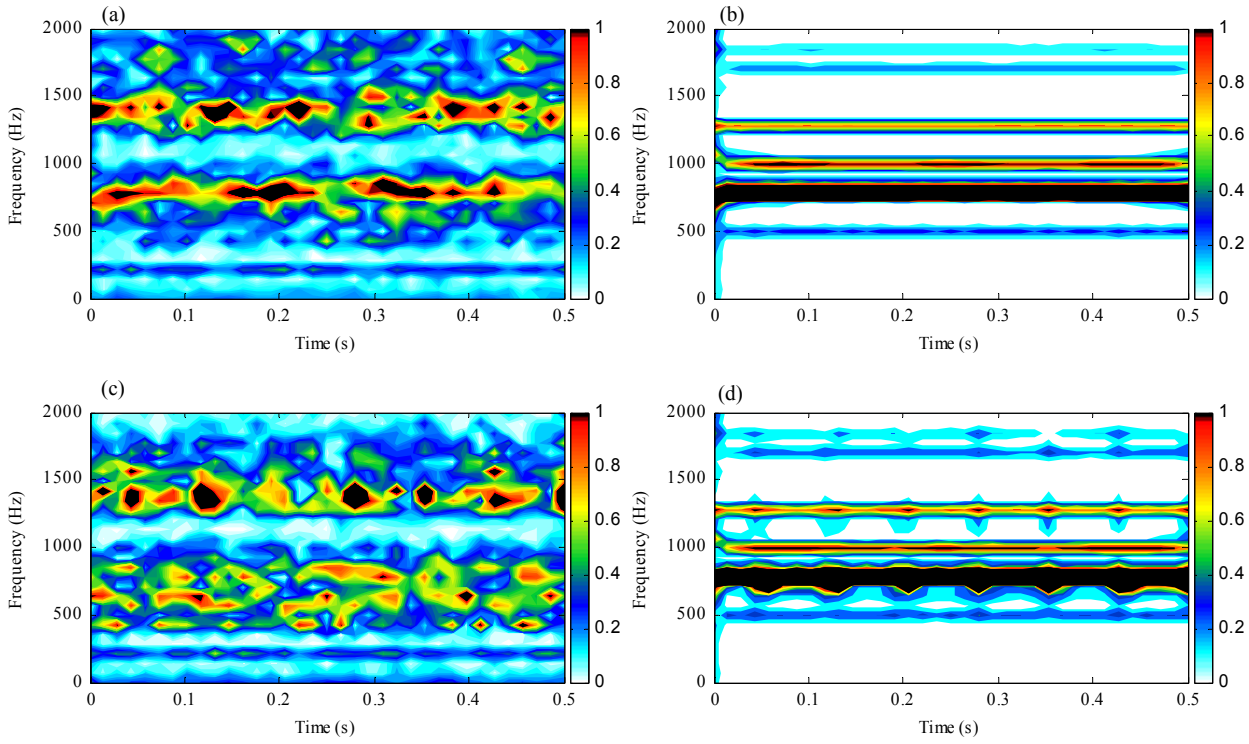

Figure 59. HWT at 400x100 resolution of experimental data and model results for 820 rpm constant speed test: (a) healthy data, (b) healthy model, (c) damaged (missing tooth) data, and (d) damaged model.

The disruption due to the missing tooth appears as a pulse in the HWTs of the damaged gear at approximately the rate of input shaft rotation, 820 rev/min or 13.7 Hz, for a period of 0.073 seconds. This figure demonstrates the capability of HWT and DGM to characterize a fault in the signal. It also highlights a major benefit of using a DGM to build fault libraries, as the fault signature is more easily distinguishable in the gear fault model DGM signal than it is in the noisy damaged experimental data.

To demonstrate the non-stationary capability, the 4-second motor speed-time profile used by (Lu et al, 2012) and shown in Figure 60a (also shown in Chapter 2 Figure 3) is used. The speed increases from stop to 10 Hz (600 rpm) after one second, then increases up to 25 Hz (1500 rpm) at two seconds, and maintains this speed to three seconds before decelerating to a stop. This speed profile is used as a representative non-stationary operation benchmark and was also used in (Diehl et al, 2012) and (Diehl and Tang, 2016). It is important to note that the speed-time profile described here represents the control

message to the motor, and that actual motor speed varies with each run. The test data used in the discussions which follow are selected from multiple runs and used for general comparison rather than precise matching since the expected variation between test runs, including actual speed profile and random noise, make detailed comparisons difficult. Operating the testbed repeatedly, with the same speed command profile, returns significantly different measured/actual speed profile results in both timing and shaft speed as seen in Figure 60b.

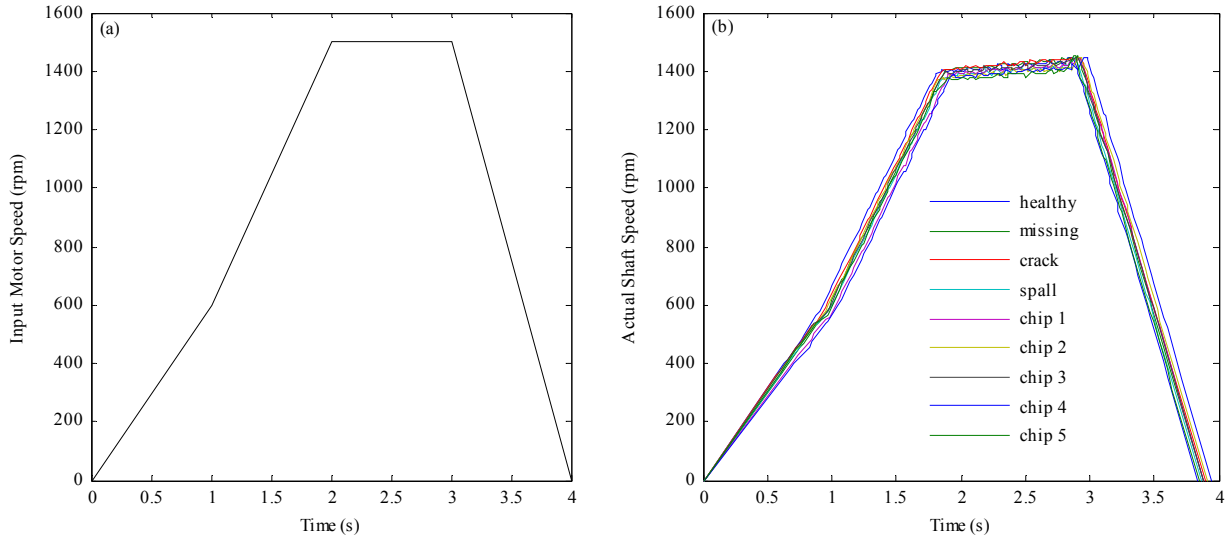

Figure 60. Speed-time profile (a) input and (b) actual.

Figure 61 presents a comparison of test data with healthy gear and missing tooth and model results with the measured speed-time profiles and processed with HWT. Note that the speed-profile of the healthy test was used for the healthy DGM, and likewise, the damaged gear test speed-profile was used for the damaged DGM. The measured motor speed multiplied by the number of teeth in the first stage pinion is the anticipated Gear Mesh Frequency (GMF1), and the second stage pinion times the intermediate shaft speed is GMF2. These GMF frequency-time profiles and their integer multiples are the kinematic behavior of the system and are superimposed on the contour plots of Figure 61 for both gear stages. The energy distribution in the HWT plots matches many of these GMFs and multiples.

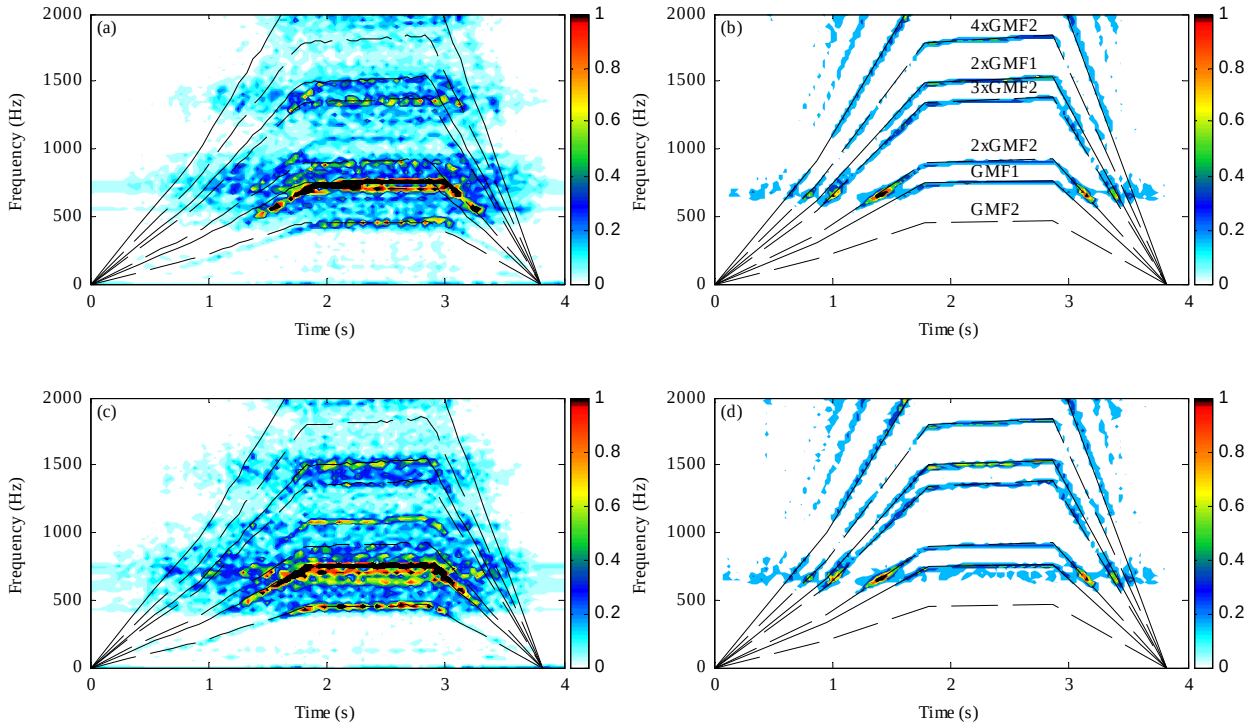

Figure 61. HWT at 400x100 resolution of experimental data and model results for varying speed test: (a) healthy data, (b) healthy model, (c) damaged (missing tooth) data, and (d) damaged model, with gear mesh frequencies (GMF) and integer harmonics superimposed.

Visual comparisons of the HWT contour plots in Figure 61 reveal differences between the healthy and damaged cases in both experimental data and model results. While the healthy-damaged differences are not entirely consistent between data and model, there are fault feature trends in common, such as the increase in magnitude in GMF2 and widening of the regions near and around GMF1. While these contour plots aid in visualizing the wave map, the subtle numerical differences within the coefficient matrix contain feature patterns to be used to build libraries within pattern recognition algorithms. Considering the speed variation in test data and also factoring in random noise, the test data is mostly useful for representative or anecdotal comparisons. The benefits of using a DGM to compare healthy and faulty behavior include the repeatability of speed profile and minimal noise, besides artifacts of the numerical integration, allowing for more direct comparisons, isolating the differences due to the faults.

This variation can be mimicked by the DGM, but data-driven approaches are generally unable to account for this variation. To demonstrate the effectiveness of comparing healthy and faulty DGM,

Figure 62 presents a contour plot of the subtraction of a damaged gear DGM HWT coefficient matrix from a healthy one when both use the same speed-profile. The ability to control the speed of the DGM precisely enables isolation of the effects of the damaged gear on the energy distribution in frequency and time. A noteworthy feature in Figure 62 is the similarity within the relatively constant speed region to the pulses found in the constant speed results of Figure 59. These pulses represent a potential feature that a pattern recognition algorithm can use when developing fault libraries and are investigated further in a later section which uses refined time resolution.

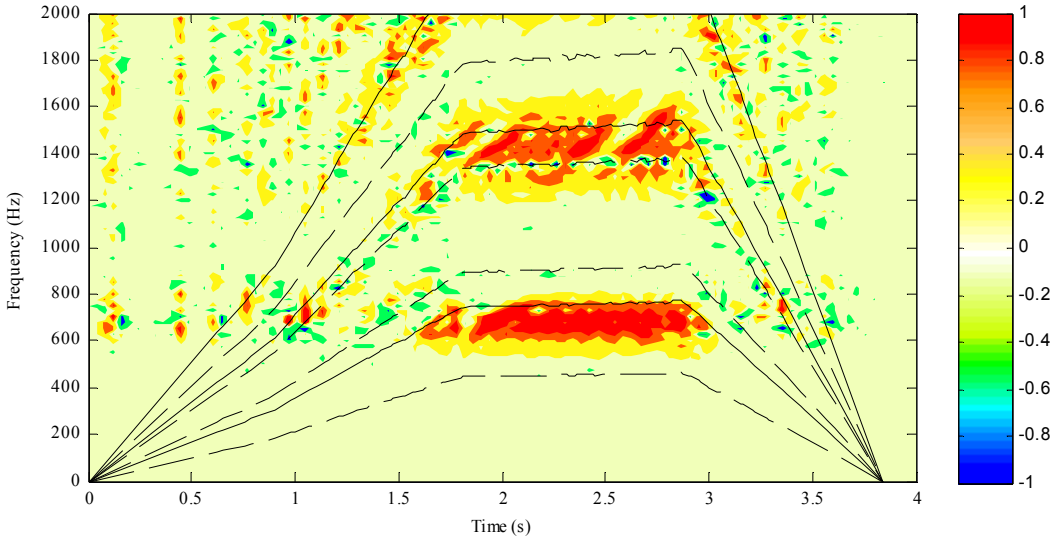

Figure 62. Contour plot of difference between HWTs at 400x100 resolution of healthy and damaged model results, with gear mesh frequencies (GMF) and integer harmonics superimposed.

4.3 HWT Applied to Data and DGM for Different Fault Types

The color scale represents energy intensity of the contour plots, therefore characterizing the energy distribution of the vibration signal with respect to both frequency and time. The contour plots used throughout this section are presented with consistent scales for comparison between fault types and fault severity; although a different scale is used for test data and model results. Since the purpose of the contour plots is visualizing the HWT coefficients, the contour level and scale are selected for best presentation, but the HWT coefficient values have more subtle distribution, therefore closer inspection of the changes due to faults is made by focusing on particular times or frequencies and taking "slices" through the coefficient matrix. Slices through a particular time represent snapshots of the frequency spectrum, and slices through a particular frequency reveal the time history at that frequency, although the operating speed needs to be relatively steady for this time history to be meaningful.

The presence of a fault in the frequency domain is indicated by increases in the magnitude of gear mesh frequency integer multiples and the presence and increase of side-bands around those frequencies (Norton et al, 2003). Sidebands develop due to shaft rotation frequency modulation with the higher gear mesh frequency (GMF) and are typical of localized gear faults.

Sidebands typically appear symmetrically at intervals equal to the shaft speed frequency about the GMF multiples. If the frequency resolution is low, then the sidebands appear as thicker, darker areas around the GMF lines on HWT contour plots. Changes in the HWT contour plots with varied faults are differences in vibration signal energy distribution due to the gear fault type or severity, suggesting a unique characteristic or feature to be associated with that fault type. Finding particular fault features can make them identifiable in pattern recognition applications.

The goal of this analysis is to use the DGM to characterize these features. Sidebands found within the slices of test data HWT contour plots are often inconsistent, as is expected not only because of noise and variation but also because the fault is intermittent and the slices through the HWT are at specific times. The data must therefore be analyzed carefully to extract sideband content. A selective process which

identifies only peaks on each side of the GMF in the test data is applied to find the average sideband value across all the test runs performed.

Contour time-frequency plots of HWT processed experimental test data and corresponding model results are presented side-by-side in Figure 63 at 800x50 resolution and Figure 64 at 100x400 resoution. The plots include healthy gear operation and four types of faults: chipped tooth, missing tooth, root crack, and spall. The basic shape of the speed profile from Figure 60 is evident in all graphs with varying intensity. The lines superimposed on the contour plots shown in all the graphs represent the gear mesh frequency of the first stage gear pair (GMF1) and second stage gear pair (GMF2) and integer multiples, referred to as 2xGMF1, 2xGMF2, 3xGMF1, 3xGMF2…etc. These frequencies are usually the largest in gearbox vibration signals. This discussion focuses on the relatively flat plateau region of the speed profile which is 1500 rpm (25 Hz) in the command speed profile but in the actual speed profile typically rises gradually within the range 1350 and 1450 rpm. The vertical double arrowed section lines on Figure 64 represent *times slices* located approximately at 2.4 seconds, when the speed reaches 1400 rpm in most of the tests. This is where much of the analysis which follows focuses. Table 14 summarizes the expected gear mesh frequencies when the machine operates at that speed.

Table 14. Expected frequencies (Hz) from gearbox operating at speed profile plateau*.

GMF2	GMF1	2x GMF2	3x GMF2	2x GMF1	4x GMF2	3x GMF1 and 5x GMF2	6x GMF2	4x GMF1
450	750	900	1350	1500	1800	2250	2700	3000

*Approximately 1400 rpm
GMF: gear mesh frequency

The *frequency slice* locations indicated in Figure 63 and used for discussion are taken at approximately 1500 Hz which corresponds to 2xGMF1 between 2.3 and 2.5 seconds.

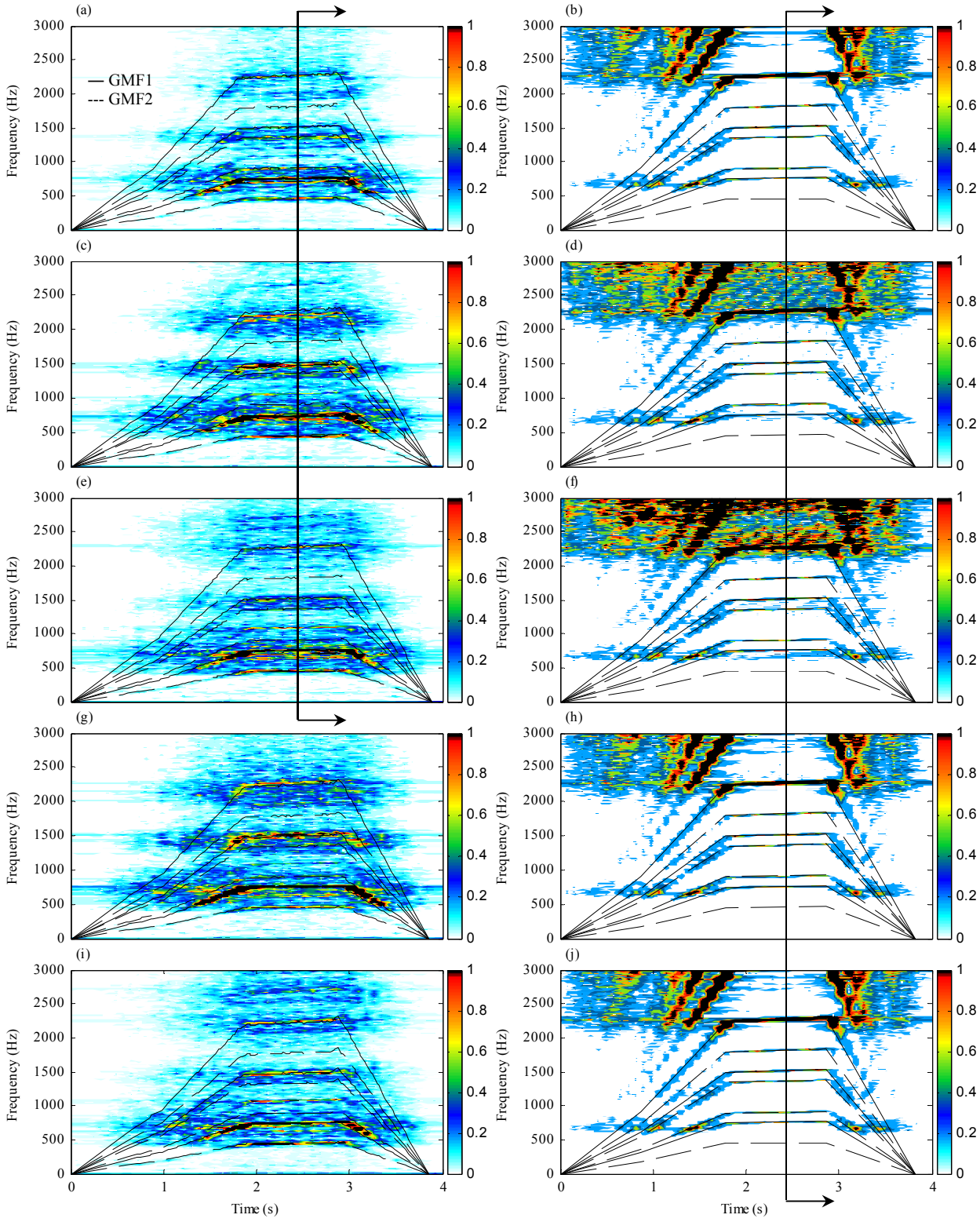

Figure 63. HWT contour plots at 800x50 resolution of (a) healthy data, (b) healthy model, (c) chip 5 data, (d) chip 5 model, (e) missing tooth data, (f) missing tooth model, (g) root crack data, (h) root crack model, (i) spall data, and (j) spall model. Gear mesh frequencies (GMF) and integer harmonics superimposed.

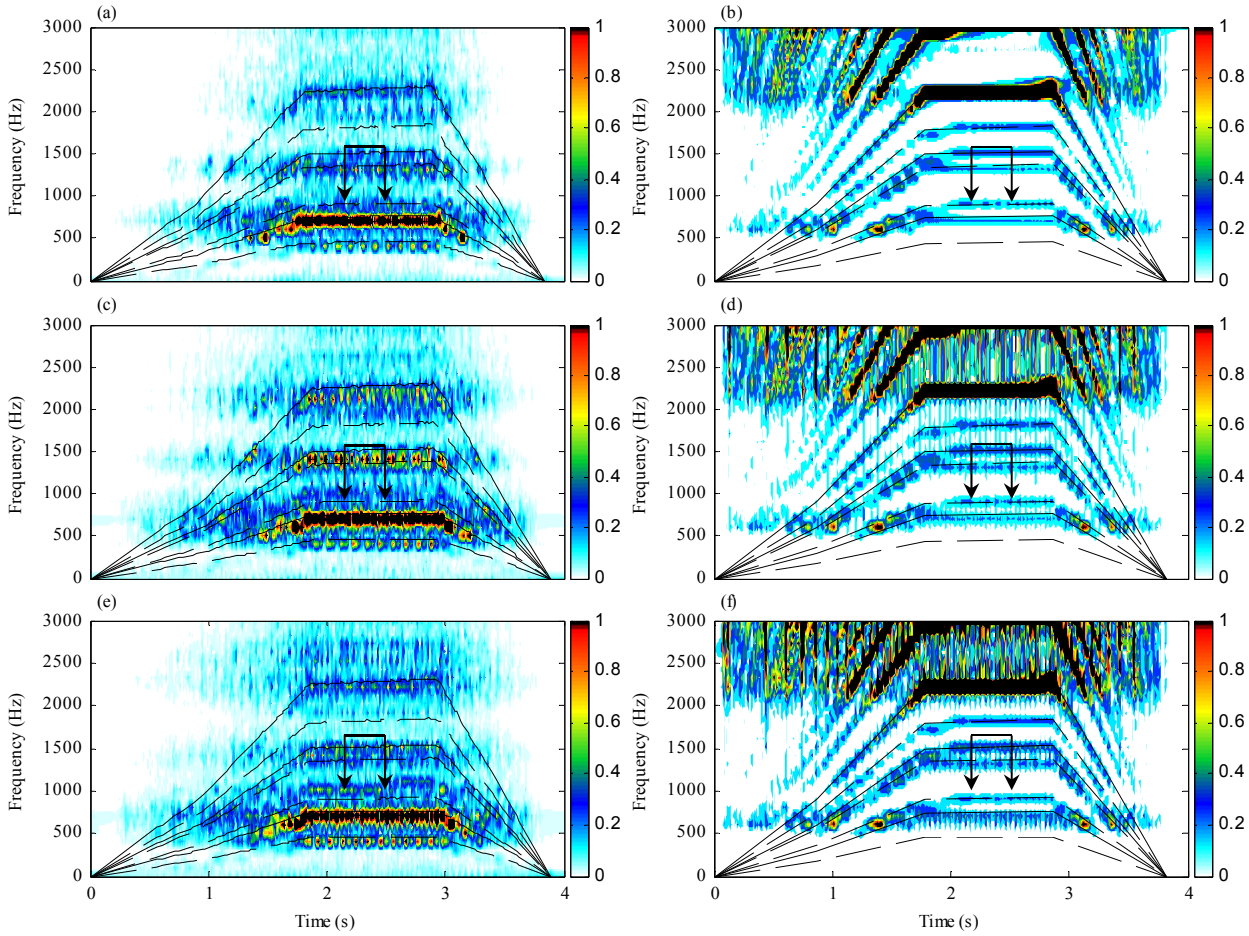

Figure 64. HWT contour plots at 100x400 resolution of (a) healthy data, (b) healthy model, (c) chip 5 data, (d) chip 5 model, (e) missing tooth data, and (f) missing tooth model. Gear mesh frequencies (GMF) and integer harmonics superimposed.

4.4 HWT Used for DGM Validation

This model was previously validated using spectrum analysis of constant speed test data and model in Chapter 3. Here test data and DGM results are compared via slices through the HWT. Figure 65 shows a comparison of contour plot vertical slices of Figures 63a and 63b. The overlain frequency maps of both test and model in Figure 65 reveal the presence of first and second gear mesh frequencies (GMF1 and GMF2) and their first second and third multiples in both test data and model marked by numbered circles. The values of GMF2 and multiples are relatively small in the test data, likely due to the location of the accelerometer closer to the first stage than the second. There is relatively low noise between GMFs and multiples in both test data and DGM results in this healthy state comparison, allowing for observation of changes due to faults. As will be seen in the sections demonstrating gear fault comparisons, faults often fill the regions between GMFs. The model shows much more high frequency content than the tests. This is a disparity attributed to factors such as damping, model natural frequency and features not modeled. The model damping is linear and based on the first natural frequency of an impact test, and therefore does not attenuate these higher frequencies.

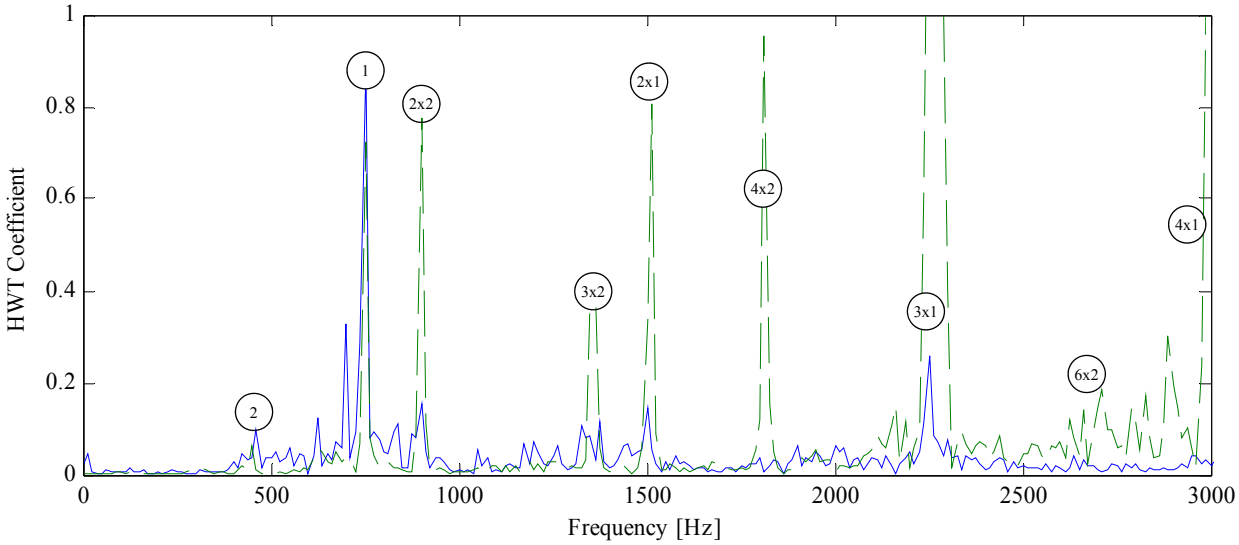

Figure 65. Vertical slices of HWT contour plots at 2.4 seconds of healthy test data (—) and model results (---) at 800x50 resolution. ① - 1st stage gear mesh frequency, ② - 2nd stage gear mesh frequency.

The natural frequencies of the lumped parameter DGM summarized in Table 15 (repeated from Chapter 3) include many in the region above 3000 Hz while few response frequencies above 3000 Hz were found from hammer tests of the gearbox shafts and housing. Many of these frequencies are due to the combination of bearing stiffness and shaft bending stiffnesses since they shift when these parameter are changed. A notable observation was made when increasing the shaft bending stiffnesses by several orders of magnitude: the high frequency content was much improved but the model solution speed was reduced dramatically. The solution speed became so slow as to make this model unusable for the intended investigations. This is attributed to the differential equations becoming "stiff". Other solution methods than the 4th order Runge-Kutta were attempted without successfully increasing the solution speed to an acceptable, usable rate. This finding, however, demonstrates a potential solution warranting further investigation in future research.

Table 15. DGM Natural frequencies (Hz)

1st	2nd	3rd	4th	5th	6th	7th	8th	9th	10th	11th	12th	13th
0	75	117	677	744	841	859	882	901	2150	2260	2320	2820
14th	15th	16th	17th	18th	19th	20th	21st	22nd	23rd	24th	25th	26th
2820	3620	3870	3870	4430	4460	4480	4660	5430	5630	5740	6070	8250

Other aspects contributing to the difference between test data and DGM results includes omission of features in the model. These include the attenuation effects of the transmission path at the bearing housing and the natural filtering effects of the instrumentation are not considered in the DGM. While these modeling issues exaggerate some frequencies, the differences between healthy DGM and fault models are easily identified and the overall comparison of healthy test data and DGM results is quite good below 2500 Hz. The presence of the expected frequencies in both test and model validates that the model captures the basic kinematic behavior of the gearbox.

4.5 DGM Sensitivity to Fault Type

The frequency behavior of measured faults and modeled faults is expected to be unique since the stiffness variations due to the faults are also unique as demonstrated in Figures 16 through 19 of Chapter 2. Slices through the contour plots for each fault type shown in Figures 63 and 64 are shown in Figures 66 through 70 and discussed below. Note that coefficient ranges as well as frequency ranges vary amongst these graphs to assist in highlighting areas of interest. For this discussion the chipped tooth and missing tooth faults are grouped together and the root crack and spall also grouped since these faults have several in-common traits.

4.5.1 Chipped Tooth and Missing Tooth Faults

The chipped tooth fault and missing tooth fault both disrupt the varying mesh stiffness pattern by removing a portion and briefly changing the number of teeth pairs sharing the load, therefore causing the contact ratio to momentarily change. The reduction of teeth pairs can also result in an impact when the next undamaged teeth pair collide before resuming the regular mesh pattern. The sudden change in mesh stiffness pattern causes vibration changes, and the periodic nature is reflected in the frequency content.

The chip used for this discussion is referred to as “chip 5” since it is the largest of the five chip sizes discussed in the next section. Figures 66a and 66b show the vertical slices through the contour plots of Figures 63a, 63b, 63c and 63d to compare the healthy and chip fault frequency behavior. Figure 67a shows the vertical slices of healthy and missing tooth test data contour plots from Figures 63a and 63c, and Figure 68b shows the vertical slices of the corresponding model results.

The changes to frequency content in the slices for these two faults have much in common, which is expected since a missing tooth can be thought of as a severe case of a chipped tooth although the test data indicates more changes in magnitudes and sidebands than the missing tooth. The most readily apparent changes in both chipped and missing tooth are the activity around all three GMF1 multiples where sidebands appear. The region around 2xGMF1 is found to be especially important as will be discussed in

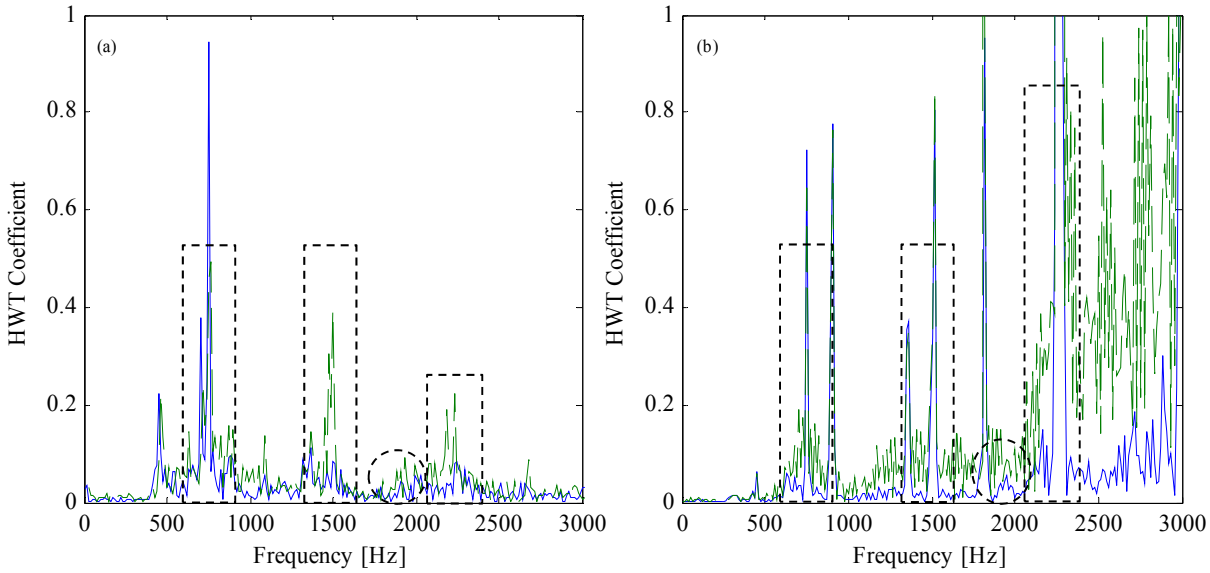

Figure 66. Vertical slices of HWT contour plots at 2.4 seconds of healthy (—) and chip 5 (---) for (a) test data and (b) model results at 800x50 resolution.

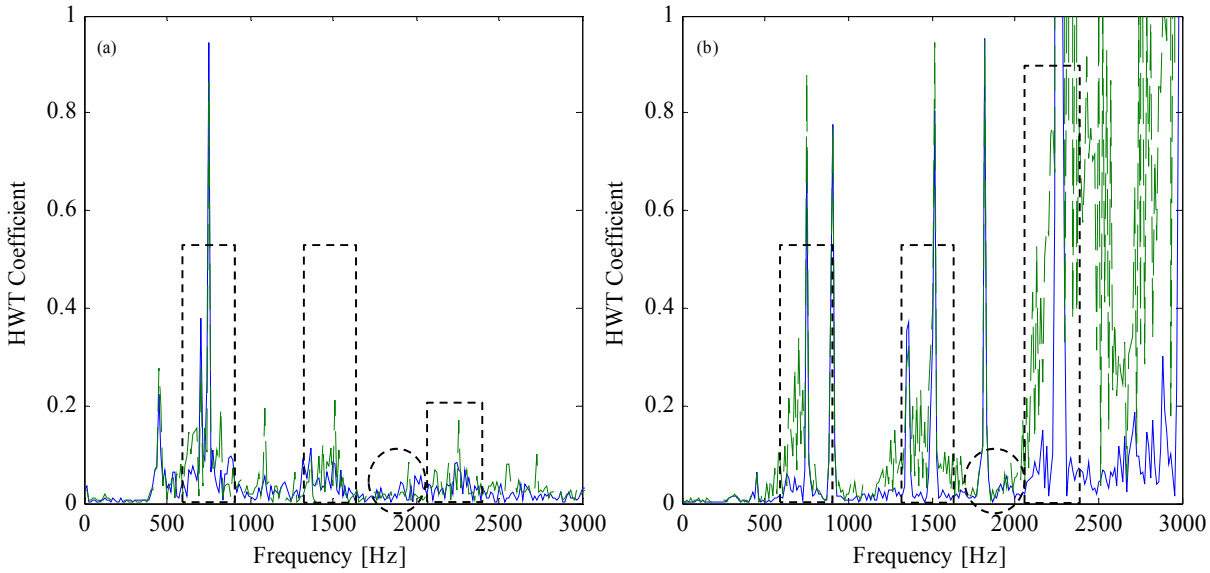

Figure 67. Vertical slices of HWT contour plots at 2.4 seconds of healthy (—) and missing tooth (---) for (a) test data and (b) model results at 800x50 resolution.

the section on chip size. The results of a sideband search show an increase around 2xGMF1 of approximately 170% for chip 5 and 80% for the missing tooth compared to the healthy baseline floor which had few genuine sidebands, as expected. The DGM predicts an approximate 900% increase for chip 5 and 1250% for the missing tooth sidebands compared to the very low floor of the healthy DGM baseline on either side of 2xGMF1. The missing tooth fault model used in the DGM produces a larger

change in the mesh stiffness than the chip fault model causing a larger effect on the vibration. The majority of peaks at GMF multiples show no clear trends for the chip faults nor the missing tooth fault in test data or fault model results. Many of the peaks decreased in both test data and model results from the healthy condition. The peak at 2xGMF1 reinforces the sideband situation where the model predicts a larger value for the missing tooth than chip 5 but the data indicates the reverse. The missing tooth in the physical gear completely eliminates a gear tooth pair impact with each shaft revolution, and while the change to the mesh pattern causes vibration, the tip of the chipped tooth causes an impact onto its gear counterpart the missing tooth does not experience. The missing tooth fault is also aided by the high contact ratio used in the test rig, since a missing tooth in a lower contact ratio gearset is a much more severe fault. This may explain the counterintuitive discrepancy between prediction and test data, suggesting that the missing tooth fault model requires refinement.

Figure 68 shows a horizontal slice through the 100x400 resolution HWT contour plot of Figures 64a through 64f in the vicinity of 2xGMF1 (1500 Hz) to provide a time history of the events when the shaft speed is approximately 1400 rpm or 23 Hz. The resolution of this HWT slice (0.01 seconds) favors time to reveal impact events taking place at approximately 0.04 second intervals which is close to every shaft revolution. Figure 68a shows that the test data for chip 5 has larger periodic peak magnitudes than the missing tooth. Figure 68b indicates that the missing tooth DGM fault model has greater magnitude than the chip 5 fault model. The conclusion drawn is that the missing tooth fault model is either exaggerating the effect of the mesh variation or the chip 5 fault model does not sufficiently capture the impact behavior. Using the time history together with the frequency of the HWT, and changing the resolutions to target particular frequencies allows for better characterization of the fault behavior and to identify areas for improving the fault models.

Besides sidebands and GMF peaks, faults may produce frequency content in between the expected bands. An example is found in the DGM results for the missing tooth where a region around 1700 – 2000 Hz, highlighted in the figures by a dashed oval, shows little change from the healthy condition, approximately 30% excluding the band just around 1800 where 3xGMF2 has a peak. Similarly, the test

results in this region only increase 10% for the missing tooth. The frequency content in this region for chip 5 increases by 250% and 110% in the model and test data, respectively. Another example is the region between 3xGMF1 and 4xGMF1, which is 2350 – 2950 Hz. In both test data and model the missing tooth fault has a larger increase in average energy content for this region; the test data increases by 30% for chip 5 and 85% for the missing tooth while the model increases 500% for chip 5 and 800% for the missing tooth. Referring back to Figures 63c through 63f confirms this is a region of more activity in the contour plot for the missing tooth than for chip 5 in both test data and model. While not definitive, this approach to investigating common patterns of fault behavior is a useful tool for identifying features where fault models can predict fault features. A similar approach is used in the discussion of root crack and spall faults which follows.

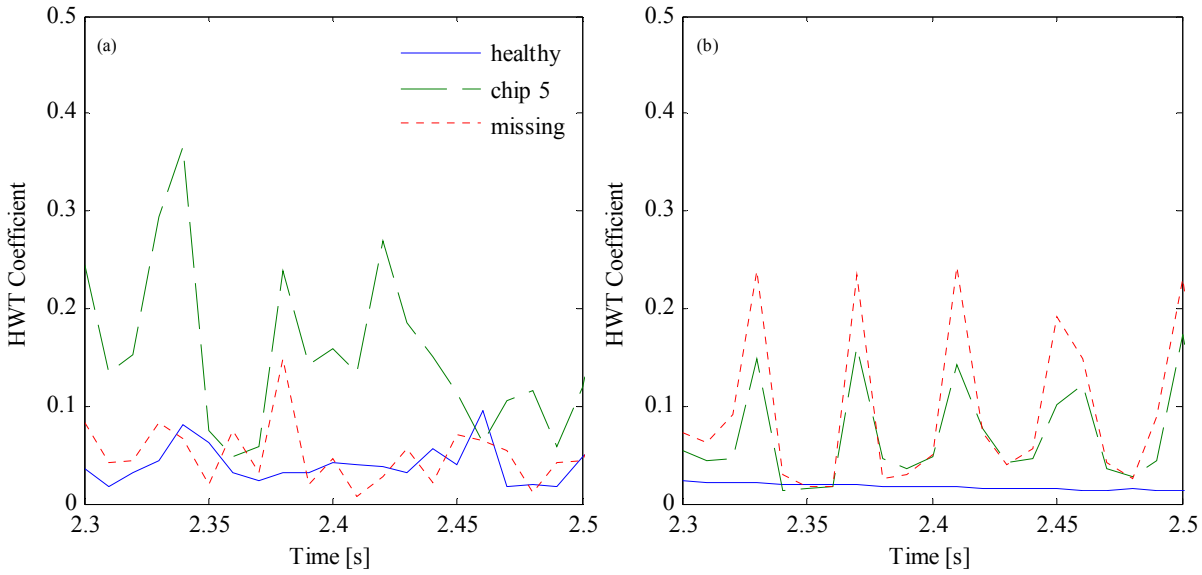

Figure 68. Horizontal slices of HWT contour plots at 1500 Hz of healthy and different faults for (a) test data and (b) model results at 100x400 resolution.

4.5.2 Root Crack and Spalled Tooth Faults

The root crack and spalled tooth faults are similar in that the stiffness of a single tooth is reduced by the defect rather than removed or ended early. The crack and spall faults, purposefully selected as challenging tests of fault detection, are more difficult to detect and distinguish than the chip and missing tooth and have features not easily modeled. For instance, an important aspect of a real root crack omitted from the test sample and fault model in this investigation is the opening and closing of the crack which can generate chatter-like impacts in the vibration. The seeded fault in the tested gear was made using a wire cut leaving a substantial gap at the simulated crack, so this feature is not an issue but noteworthy nonetheless. The real cracked tooth will also tend to vibrate at its local natural frequencies after initial impact more readily and at lower frequencies than the other healthy teeth; a feature not included in the model. Features not modeled but existing in the real spall include lose of contact surface area changing the contact stiffness and missing surface material changing the friction between the damaged tooth and mating gear tooth. Lube oil retained within the gap in the cracked tooth and within the pit of the spall may also change the local damping and further periodically disrupt the meshing process. The combined effects of these omitted fault features are believed to have contributed to significant differences in test data and DGM results. As will be seen, both fault models produce has very little difference in lower frequencies, below 2000 Hz. The test data does contain differences to the magnitudes and sidebands around GMF multiples in this range similar to the chip and missing tooth faults due to the disruption of normal meshing. Rather than attempt to make direct comparisons between the test data and DGM fault model HWT results, the severities of the fault models are increased to highlight the particular signatures uncovered between prominent frequencies.

Other researchers of gear cracks and spalls have found identifying them to be challenging. Increases in the prominent frequency gaps have also been observed as identifiers by other researchers of these fault types. Spur gear crack simulation studies such as (Wu et al, 2008) and (Mohammed et al, 2015) found modest to no indication below 30% crack which is approximately the crack size used in our testbed, suggesting that crack models in this range yield less obvious vibration signatures. Cracked experimental

data and a 12-DOF single-stage DGM were compared by (Ma et al, 2015) for four crack depths, including some spectral analysis which was found to be inconclusive regarding measured crack size. The researchers were able to use empirical mode decomposition along with statistical indicators to identify the larger cracks (50% and 60%) but had mixed results for smaller cracks. Researchers using spall models include (Jia and Howard, 2006) who used a 26-DOF two-stage DGM to compare a tooth crack and spall models, (Chaari et al, 2008) who used an eight-DOF single-stage DGM to compare spalls and chipped teeth models, (Endo et al, 2009) who used a static analysis method to compare FEA models and experiments of varying sizes of tooth cracks and spalls in a differential diagnosis technique based on auto-regressive filters, and (Ma et al, 2012) (not the same researcher as (Ma et al, 2015)) who used a two-DOF single-stage model and test rig to compare four different spall sizes. Of these spall fault studies, only (Chaari et al, 2008) and (Ma et al, 2012) used spectrum comparisons to healthy gear, and (Chaari et al, 2008) was purely model based. The spectrum plots of DGM results and experimental data presented by (Ma et al, 2012) showed increased frequency content between gear mesh frequency multiples, which suggests the similar peaks identified in our results have physical meaning. The research discussed above show that while identifying small root cracks and spalls in models and tests is possible, there exist opportunities to further develop models of these fault types.

To characterize the root crack and spall faults, their severities are increased and the results used for an apples-to-apples comparison. The root crack fault model is increased from 30% to 50% through the tooth thickness, and the spall fault model depth is doubled. The results are presented in Figures 69 and 70, showing vertical slices through the HWT contour plots from Figures 63h and 63j, respectively, with frequency range extended up to 6000 Hz. Both fault models begin to show significant increases above 3xGMF1, approximately 2300 Hz. The frequency content in regions between gear mesh frequencies and other bands believed to be indicative of the presence of faults is presented in Table 16 for comparison. The values in the table represent average percentage increases of the root crack and spall models compared to the healthy DGM results for frequency regions between spikes indicated by the boxed numbers in the table and both Figures 69 and 70. The average increase in frequency content in these

regions can be used to quantify the amount of energy increase. Some regions with increased energy above the healthy baseline do not increase with these fault size changes while others do. This parametric approach reveals particular traits of the fault model that can inform the search in real data.

In region 1, between 3xGMF1 and 4xGMF1, the average frequency content increases by approximately 25% and 70% for increased crack size, while the larger spall has the same 45% increase as the smaller spall. Similarly, region 6, 5400 – 6000 Hz increases with a larger crack while the spall has the same increase regardless of size. Both fault size increases create larger changes in region 2, which is between 4xGMF1 and 5xGMF1, with the root crack size having greater effect than the larger spall. Region 3, which includes 9xGMF2, 4050 Hz, has very little change in either spall size while the crack a modest 25% change. Region 4 between 4600 and 4900 Hz has greater spall energy increase than the root crack for both sizes. And finally, the narrow band of region 5, which is between 11xGMF2 and 7xGMF1, shows increases in both root crack and spall and relatively little difference due to size. These comparisons demonstrate subtle yet measurable changes the fault model type has on the energy distribution found from taking the HWT of the changing signal. Taking slices through the HWT contour plot helps the discussion of results, but the future implementation will use pattern recognition algorithms across the entire HWT mapping including impacts events in the time domain as well as frequency content.

Table 16. Average Increases of Crack and Spall Fault Model Results

	Frequency Bands [Hz]					
Fault Model	2300-2900 [1]	3100 - 3700 [2]	3900 - 4400 [3]	4600 - 4900 [4]	5000 - 5200 [5]	5400 - 6000 [6]
30% Crack	25%	60%	25%	40%	85%	190%
50% Crack	70%	130%	25%	40%	85%	145%
Spall	45%	70%	2%	50%	50%	95%
2xSpall	45%	100%	3%	60%	60%	95%

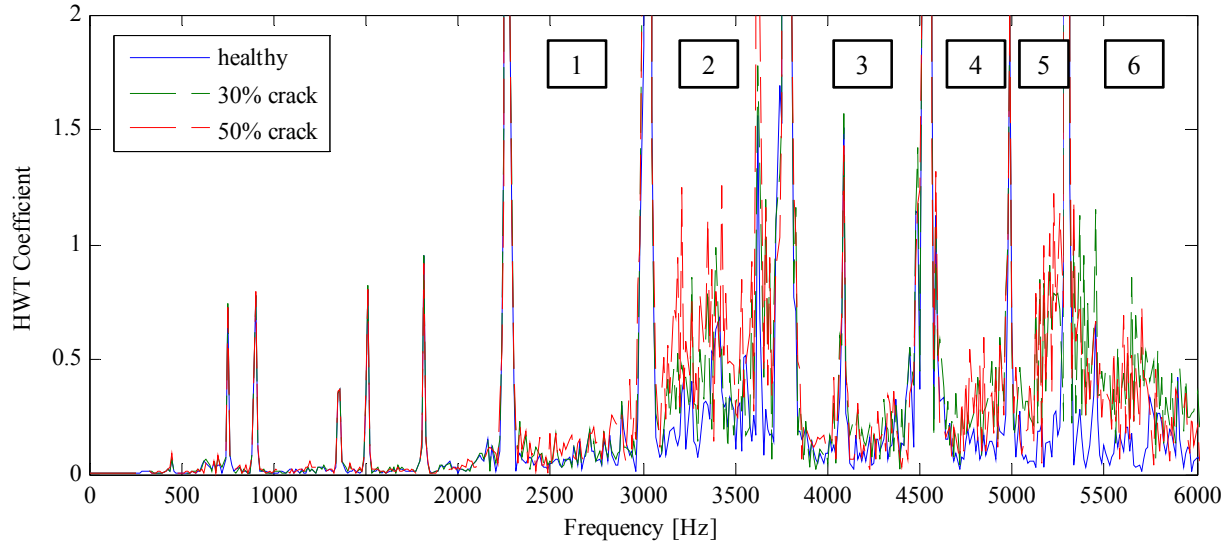

Figure 69. Vertical slices of HWT contour plots at 2.4 seconds of healthy (—), 30% root crack (---), and 50% root crack (---) model results at 800x50 resolution, 0-6000 Hz.

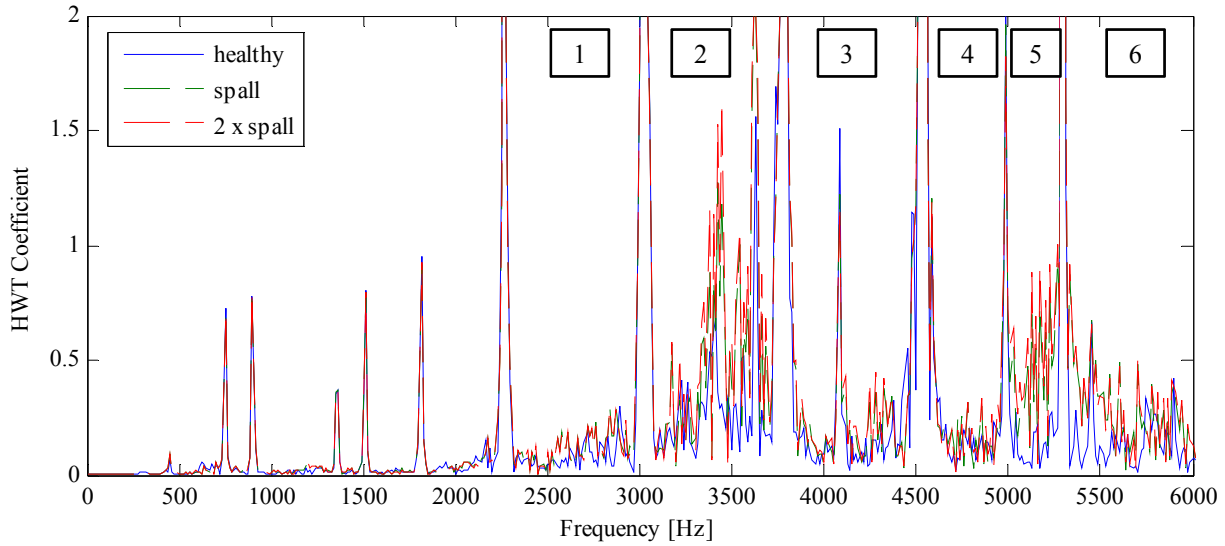

Figure 70. Vertical slices of HWT contour plots at 2.4 seconds of healthy (—), spall (---), and 2 x spall (---) model results at 800x50 resolution, 0-6000 Hz.

4.5.3 Fault Type DGM Differential

Subtracting the healthy DGM from the faulty DGM HWT matrices, a differential contour plot can be created to help visualize the effects of the various faults on the energy distribution in the vibration signal. Figure 71 presents differential contour plots of the four fault types. The differential concept is quite similar to the residuals often used in other fault detection methods. Because the speed of the model is controlled to operate at the same speed profile each time, each matrix cell represents the same frequency and instant in time, and any difference is attributable to the fault. This eliminates the influence of the variation between tests and random noise to isolate the changes in energy distribution.

The HWT differentials of the chipped tooth (Figure 71a) and missing tooth (Figure 71b) show the largest differences, especially in the high frequency range, which, as previously noted, are exaggerated by the model due to the type of damping and DGM natural frequency excitation. These coincide with the increases seen in Figures 66 and 67 but show the entire time history of changes to the frequency content, highlighting increases around GMF1 and 2xGMF1, where the missing tooth fault model has larger magnitude. The root crack (Figure 71c) HWT differential shows energy increase around GMF3 in the vicinity of the plateau, while the spall (Figure 71d) has only minor energy differences in the range of 2500 Hz and higher. As noted earlier, the root crack and spall fault models require further investigation and refinement, but their model signatures appear to be distinguishable. While there are increases in magnitude in the test data not present in the model results and vice versa and the fault models require further development and refinement, the overall comparison demonstrates the capacity of the fault model to mimic potentially key fault features and predict others. As will be seen in the next section, the chip fault model results in a feature, sidebands around 2xGMF1, which grows with increased fault severity as does the test data.

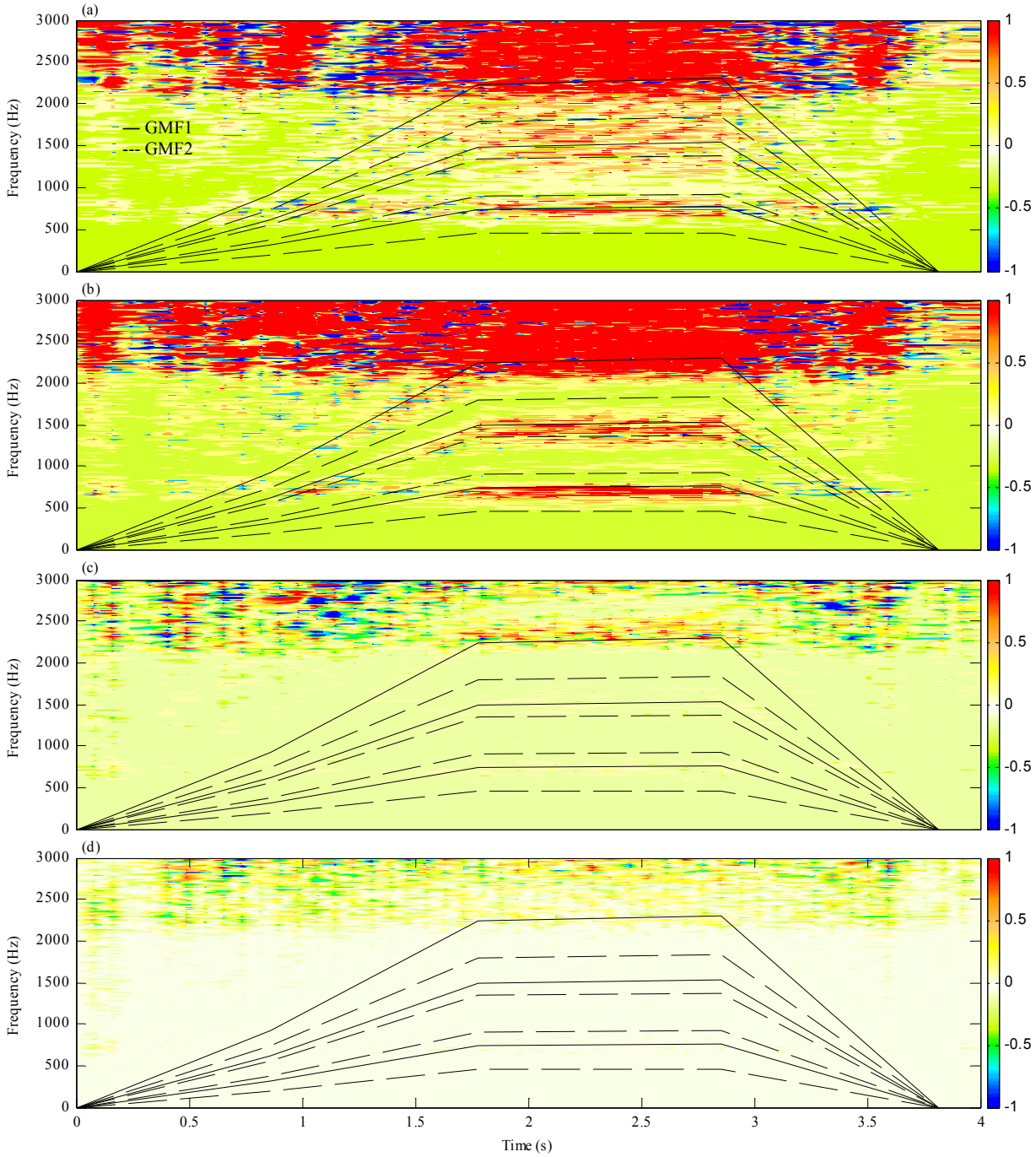

Figure 71. Contour plots of the HWT differential between healthy and (a) chip 5, (b) missing tooth, (c) root crack, and (d) spall model results at 800x50 resolution. Gear mesh frequencies (GMF) and integer harmonics superimposed.

4.6 Test Data and DGM Sensitivity to Fault Severity

Increasing chip fault severity HWT contour plots are shown in Figures 72a through 72*l* featuring healthy and five levels of chip for test data and DGM results with 800x50 resolution which favors frequency. Figures 73a through 73*l* show the same data processed with HWT of 100x400 resolution favoring time. Note that the chipped tooth fault described in the previous section is chip 5 in these figures. Section arrows are drawn through the Figure 72 contour plots at approximately 2.4 seconds to assist in discussing the results, taking vertical slices of the HWT matrix at that location, while horizontal section arrows are shown in Figure 73 indicating short duration slices taken through 1500 Hz for comparison.

Figure 74 shows HWT coefficient versus frequency plots resulting from these vertical slices of Figure 72 with boxes highlighting the regions around GMF1, 2xGMF1 and 3xGMF1 where sidebands appear. The sidebands tend to grow around all three GMF multiples in the test data, but those around 2xGMF1 were found to have a repeatable and consistent trend. Therefore the discussion of chip severity focuses on this region.

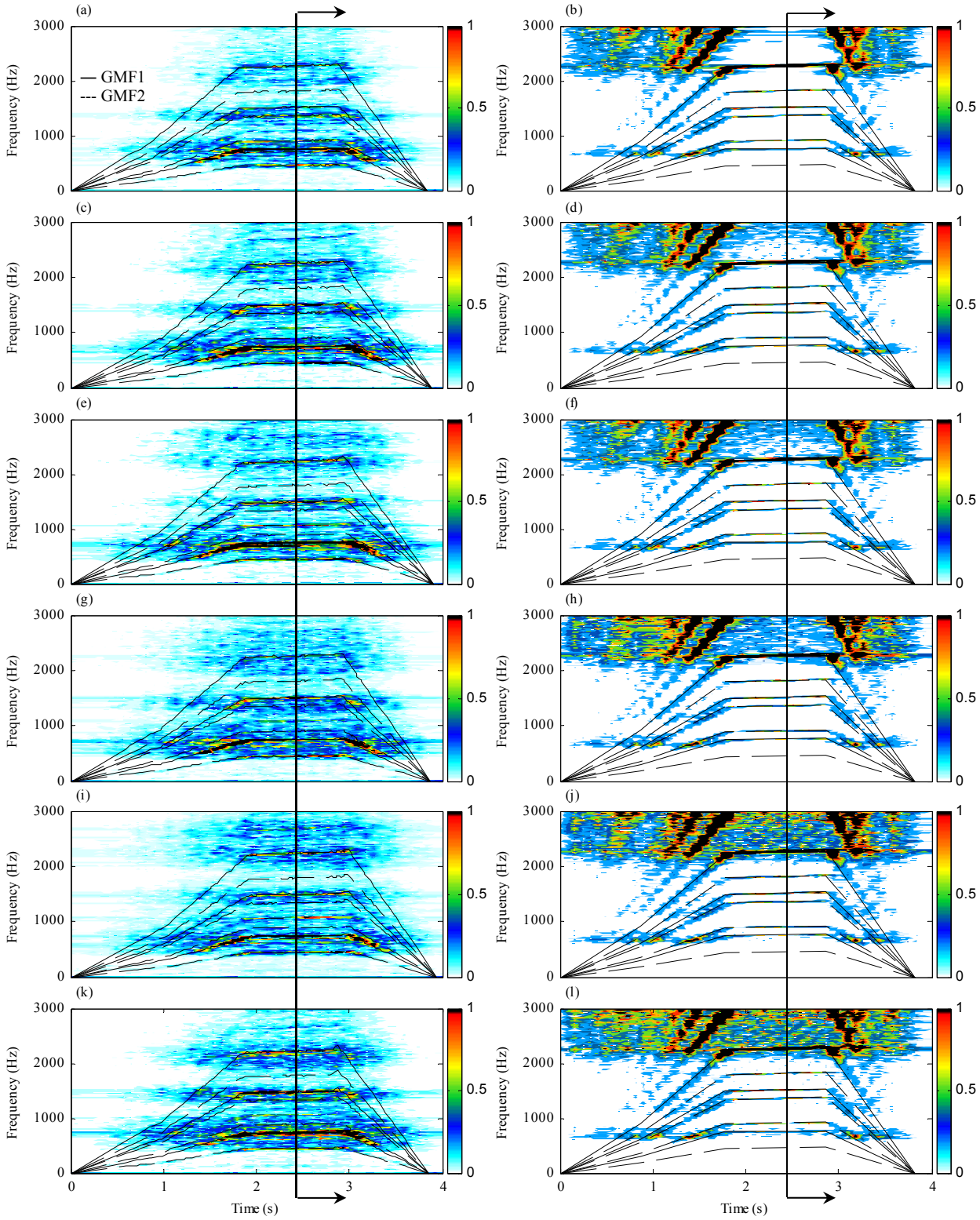

Figure 72. HWT contour plots at 800x50 resolution of (a) healthy data, (b) healthy model, (c) chip 1 data, (d) chip 1 model, (e) chip 2 data, (f) chip 2 model, (g) chip 3 data, (h) chip 3 model, (i) chip 4 data, (j) chip 4 model, (k) chip 5 data, (l) chip 5 model. Gear mesh frequencies (GMF) and integer harmonics superimposed.

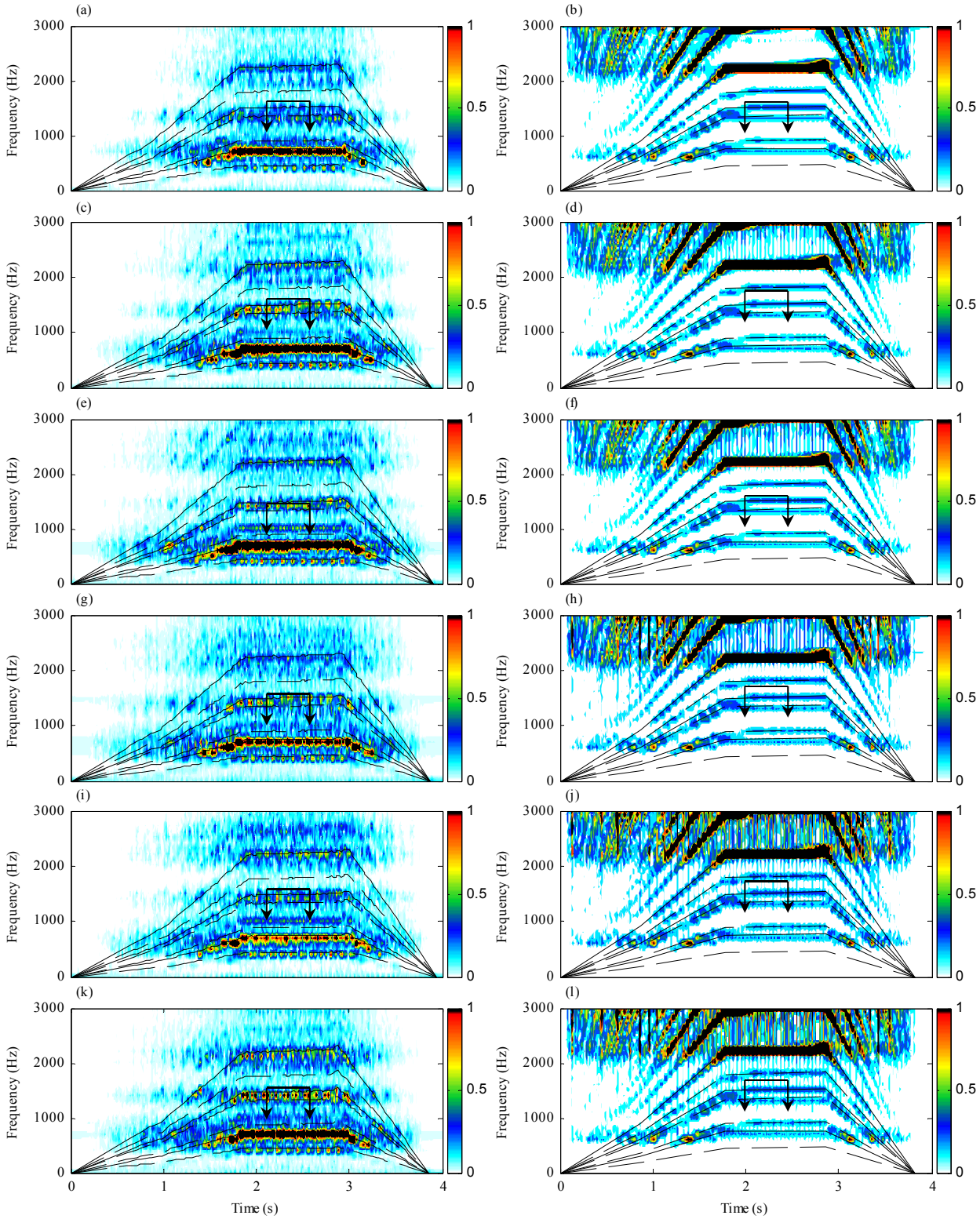

Figure 73. HWT contour plots at 100x400 resolution of (a) healthy data, (b) healthy model, (c) chip 1 data, (d) chip 1 model, (e) chip 2 data, (f) chip 2 model, (g) chip 3 data, (h) chip 3 model, (i) chip 4 data, (j) chip 4 model, (k) chip 5 data, (l) chip 5 model. Gear mesh frequencies (GMF) and integer harmonics superimposed.

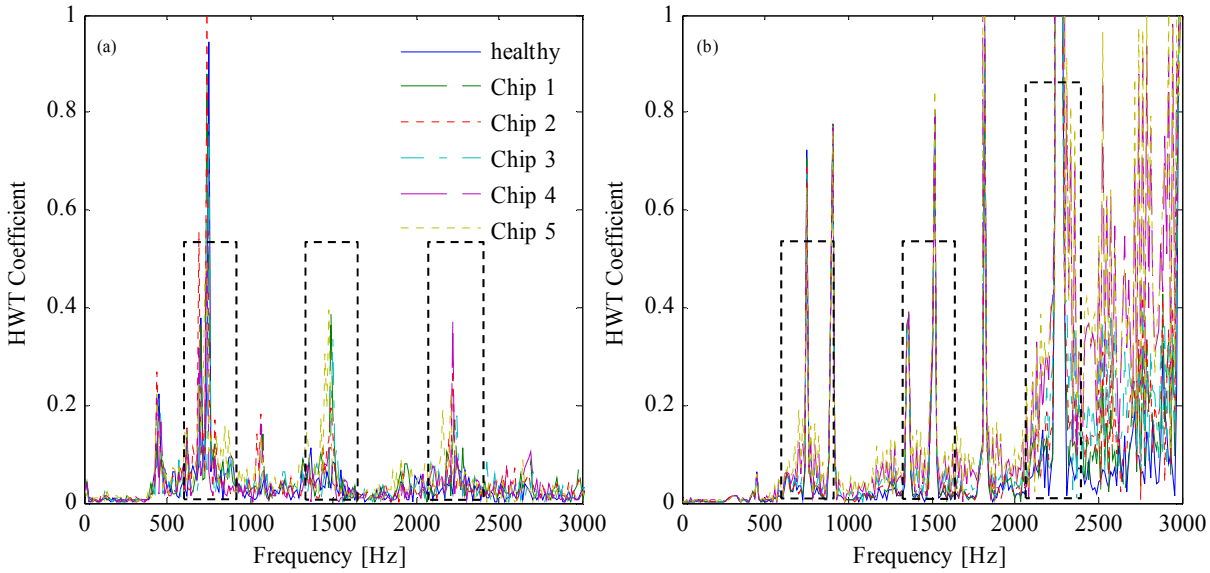

Figure 74. Vertical slices of HWT contour plots at 2.4 seconds of healthy and increasing chip size for (a) test data and (b) model results at 800x50 resolution.

Figure 75 zooms into +/- 100 Hz around 2xGMF1, but note that the data shown in 26a are selected from different test runs and sections in the vicinity of 2.4 and intended to demonstrate representative average sidebands found in this range. Since the HWT coefficient matrix includes the timing of events as well as frequency, adjacent temporal columns of the matrix are not consistent. Additionally, distinguishing what is and is not a sideband in the data requires some decision criteria, so great care has been taken to fairly select peaks. Future efforts will use pattern recognition algorithms with optimized decision criteria for identification. Also, the resolution chosen for the analysis also plays a key role in distinguishing sidebands, which are typically found symmetrically to each side of GMF multiples at intervals equaling orders of the gear rotation frequency, in this case approximately 23-25 Hz or just twice the frequency resolution. At this relatively low resolution some sidebands tend to blur and combine with peaks, appearing as wider areas around the base and sides of the GMF. The sidebands which form in the DGM around the base of 2xGMF1 shown in Figure 75b extend beyond the gear rotation frequency because of the large base. Since sidebands typically repeat to each side of the GMF, the next sideband away, approximately 50 Hz from 2xGMF1, is used when averaging the DGM sidebands.

Figure 76 presents a plot of the test data and DGM average sideband values around 2xGMF1. As can be seen, the trend for both test and model sidebands increases mostly upward, though a dip appears in the test data for chip 3. Still, the agreement is present and based on the trends seen here fault severity is detectable in the DGM using HWT. The dip in the test data at chip 3 may arise as a consequence of the high contact ratio where removing some tip can potentially somewhat improve the vibration and momentarily make the contact ration nearly 2. In this scenario the disruption to the normal meshing patter will still produce vibration, but the impact from the reduced tooth may lessen. The stiffness pattern used in the DGM and shown in Figure 22 of Chapter 2 has a small spike for chip 2 and a small dip for chip 3. Therefore the DGM fault models don't transition without a disruption, although the upward trend of the DGM sideband average has some curvature between chips 1 and 4. The horizontal slices indicated on Figure 73 of the 100x400 resolution HWT are shown in Figure 77. The periodic impacts in this region can be seen in both test data and DGM with a similar trend, where the DGM has increasing peak magnitude with increasing chip size while the test data peaks grow for chips 1 and 2, decrease somewhat for chip 3, and increase again for chips 4 and 5. The take away conclusion is that sidebands around 2xGMF1 are a fault feature that can be used to evaluate chip size in test data as predicted by the DGM fault model. This is exactly the scenario proposed: DGM fault models processed with HWT and used to predict fault features.

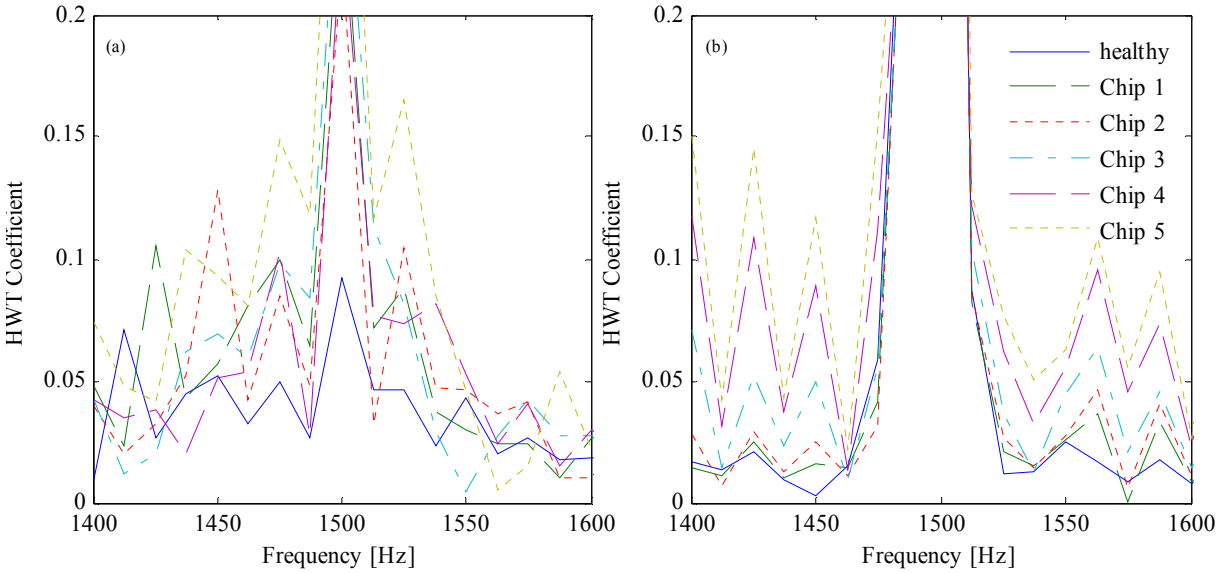

Figure 75. Vertical slices of HWT contour plots at 2.4 seconds of healthy and increasing chip size for (a) selectively representative test data and (b) model results at 800x50 resolution.

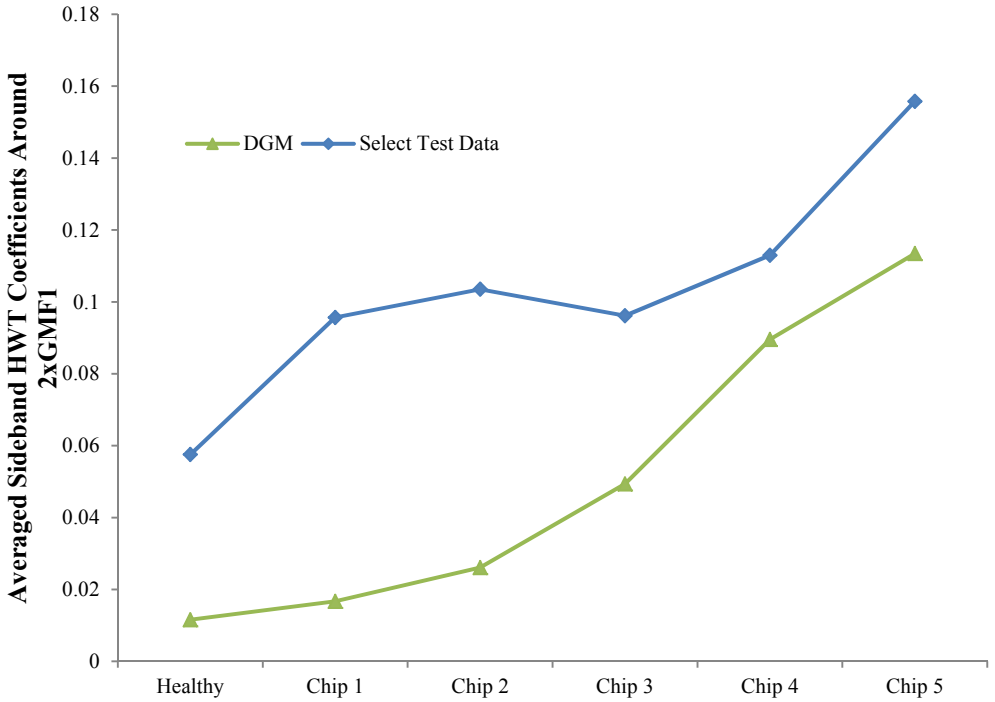

Figure 76. Average sideband HWT coefficients around 2xGMF1 with increasing chip size for select test data and DGM results.

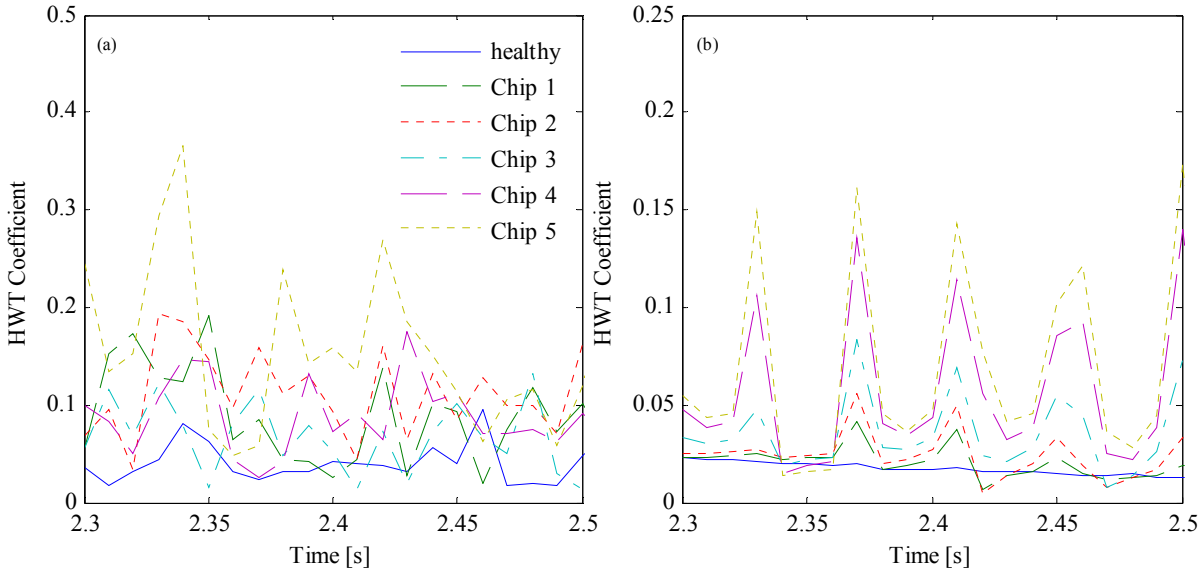

Figure 77. Horizontal slices of HWT contour plots at 1500 Hz of healthy and increasing chip size for (a) test data and (b) model results at 100x400 resolution.

The HWT differentials for the DGM with increasing chip severity are shown in Figure 78 to illustrate the time-frequency nature of the HWT and DGM analysis technique. Figures 78a through 78e show the increasing energy around the GMF multiples previously described in Figure 74 for one instant of time, but here across the entire speed profile. From this differential the signature of a chip, even a small chip from the tip of the gear tooth, emerges. The energy intensity seen below and above 3xGMF1 in chip 1 (Figure 78a) grows steadily with increasing chip size, especially above 2500 Hz, and becomes visible around GMF1 and 2xGMF1 in chip 3 (Figure 78c), larger in chip 4 (Figure 78d) and then obvious in chip 5 (Figure 78e). As mentioned in the analysis of Figure 74, sidebands are present even in Chip 1, though not visible in the differential contour plot here due to color-map resolution. Again, the purpose of these diagrams is to present the energy distribution due to the fault in both time and frequency allowing an observer to get an overall impression of the fault when presented as a contour plot. Pattern recognition algorithms, on the other hand, can use the differential coefficient values to identify fault patterns and evaluate their relative magnitude.

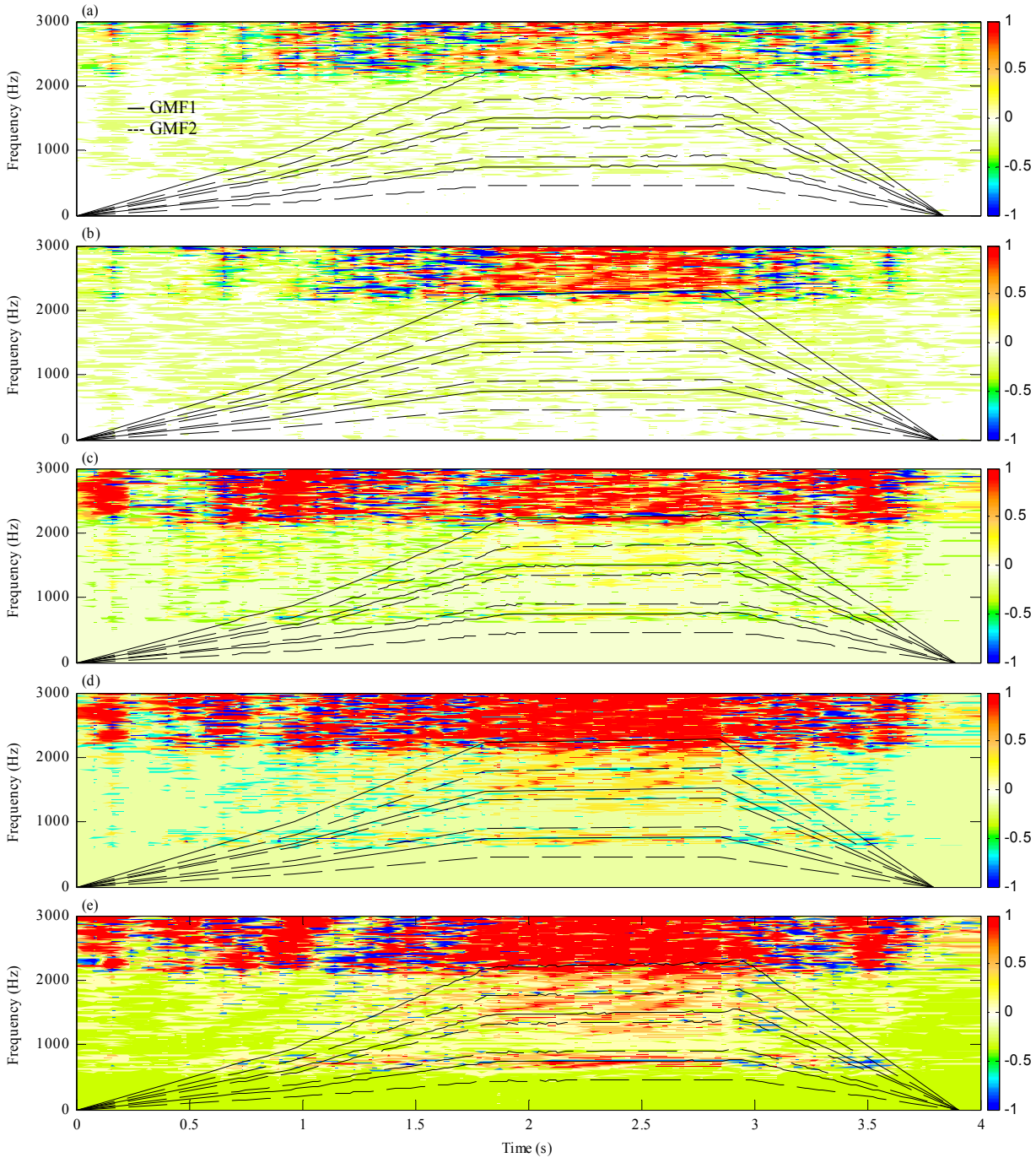

Figure 78. Contour plots of the HWT differential between healthy and increasing chip size model results. (a) chip 1, (b) chip 2, (c) chip 3, (d) chip 4, (e) chip 5 at 800x50 resolution. Gear mesh frequencies (GMF) and integer harmonics superimposed.

5. Future Work

Chapter 4 demonstrated that HWT can be used to extract features that characterize different DGM fault models and can assess fault severity in both test data and DGM results, all while operating at varying speeds. While all of the fault models, especially the missing tooth, root crack and spall, require significant development and refinement, the potential of using HWT and DGMs together to predict faults is clear. Areas for near-term further research include base model refinement to address high-frequency differences between experimental and model results and fault model development and improvements, including comparisons to more experiments with varied fault severity. Pattern recognition algorithms will be incorporated into the approach and used for blind gear fault assessment of experimental data, where the existence, type and severity of a gear fault are unknown to the analyst (but documented separately) to test the validity and ability of the approach.

The anticipated implementation of this technique is discussed here to layout the framework for future work. To use this condition monitoring technique on new machinery, a DGM is built with the minimum number of DOFs to represent the layout of the physical equipment including specific location and direction of installed accelerometers. Crucial mass, damping and stiffness parameters are measured, gathered, calculated, and developed. Initial model refinement is performed using data collected from the physical unit compared to simulated DGM results for the healthy operation. Model parameters are updated and adjusted to address issues such as choice of linear values and lumping allocation that best capture the physical behavior of non-linear components and features such as bearings and damping. Fault models are developed for anticipated fault types based on a variety of sources including first principles, experience with previous other equipment, and emerging modeling technology. The DGM with fault model types and severities are run using typical operating speed profiles and processed with HWT to identify fault features. Up to this point, the scenario described is the state of the current research presented in this paper. What follows is future work.

A pattern recognition algorithm will be used to develop fault feature libraries from the HWT processed DGM results. While the present research manually identified some possible features, pattern recognition

can process much more information to find features using multiple HWT resolutions, detect both frequency and time trends in the HWT. The DGM can operate in parallel with the machinery at the same load and speed, referred to as "co-simulation", which is especially useful in equipment such as wind turbines whose load and speed may vary continuously. Since the lumped parameter DGM is computationally efficient and computer processing speeds continue to increase, multiple models with a variety of fault types will be able to be run in parallel, all processed with HWT and with fault traits matched by the pattern recognition algorithms. When suspected faults are detected, the severity of the fault models being run in parallel can be altered to evaluate the fault extent making failure prediction possible. The result of merging the "white box" approach of the DGM with the signal processing "black box" of the HWT and pattern recognition is a "grey box" approach to condition monitoring of gear sets that predicts failure, and therefore achieves prognosis.

6. Concluding remarks

This research demonstrates combining DGM and HWT to characterize the behavior of gear fault types and fault severity in non-stationary machinery with comparisons to experimental data, working towards creating a condition monitoring technique that predicts gear failure. The technique can use DGM simulated faults processed with HWT to match machinery speed and load. The DGM used in this research is especially useful because it has real physical meaning compared to the purely data-driven CM algorithms and has been experimentally validated using frequency and time comparisons. The DGM is capable of using a variety of easily modified and refined fault models. The proposed technique will benefit from the numerous researchers who continue to develop gear fault models. The proposed technique has the potential to replace the time and expense that data-based CM techniques require to build fault libraries. Solving the lumped-parameter DGM and processing with HWT are computationally efficient; so continued improvements in computer processor speed can be exploited for real-time parallel operation with machinery.

The value of this research includes the direct comparison of DGM results to experimental data frequency content, adding to the relatively scarce experimentally validated DGM research. A commercially available gearbox testbed is modeled so other researchers may replicate and build upon it. Spectrum comparisons are made to experimental data for DGM validation instead of the non-linear jump phenomenon which, while common, is a relatively circuitous means of model comparison. This research is unique in that is uses a multi-stage gearbox with high contact ratio gear sets in non-stationary operatio and also investigates different fault type models with different severities comparing to real experimental data which is uncommon in existing research.

Future research is anticipated to use this CM technique to develop the fault libraries for use with pattern recognition algorithms and perform blind tests to demonstrate effectiveness. The prospects for running this technique continuously in parallel with machine operation will lead towards a CM technique that does not entirely rely on experiencing faults and enables prognosis.

REFERENCES

Aherwar, A., & Khalid, M. S. (2012). Vibration analysis techniques for gearbox diagnostic: a review. *International Journal of Advanced Engineering Technology*, *3*(2), 4-12.

Ahmadzadeh, F., & Lundberg, J. (2014). Remaining useful life estimation: review. *International Journal of System Assurance Engineering and Management*, *5*(4), 461-474.

Åkerblom, M. (2001). Gear Noise and Vibration: A Literature Survey.

Ali, N. J., & García, J. M. (2010). Experimental studies on the dynamic characteristics of rolling element bearings. *Proceedings of the Institution of Mechanical Engineers, Part J: Journal of Engineering Tribology*, *224*(7), 659-666.

Al-Shyyab, A., & Kahraman, A. (2005). Non-linear dynamic analysis of a multi-mesh gear train using multi-term harmonic balance method: sub-harmonic motions. *Journal of Sound and Vibration*, *279*(1), 417-451.

Al-Shyyab, A., & Kahraman, A. (2005). Non-linear dynamic analysis of a multi-mesh gear train using multi-term harmonic balance method: period-one motions. *Journal of Sound and Vibration*, *284*(1), 151-172.

Al-Shhyab, A., & Kahraman, A. (2007). A nonlinear torsional dynamic model of multi-mesh gear trains having flexible shafts. *JJMIE*, *1*(1), 31-41.

Amabili, M., & Fregolent, A. (1998). A method to identify modal parameters and gear errors by vibrations of a spur gear pair. *Journal of sound and vibration*, *214*(2), 339-357.

Archard, J. (1953). Contact and rubbing of flat surfaces. *Journal of applied physics*, *24*(8), 981-988.

Bajpai, P., Kahraman, A., & Anderson, N. E. (2003, January). A surface wear prediction model for parallel-axis gear pairs. In *ASME 2003 International Design Engineering Technical Conferences and Computers and Information in Engineering Conference* (pp. 817-826). American Society of Mechanical Engineers.

Bartelmus, W. (2001). Mathematical modelling and computer simulations as an aid to gearbox diagnostics. *Mechanical Systems and Signal Processing*,*15*(5), 855-871.

Baud, S., & Velex, P. (2002). Static and dynamic tooth loading in spur and helical geared systems-experiments and model validation. *Journal of Mechanical Design*, *124*(2), 334-346.

Blankenship, G. W., & Kahraman, A. (1996, September). Gear dynamics experiments, part i: characterization of forced response. In *ASME Power Transmission and Gearing Conference, San Diego*.

Bonel-Cerdan, J. I., & Nikolajsen, J. L. (1997, June). An Introduction to Harmonic Wavelet Analysis of Machine Vibrations. In ASME 1997 *International Gas Turbine and Aeroengine Congress and Exhibition* (pp. V004T14A011-V004T14A011). American Society of Mechanical Engineers.

Bonori, G., & Pellicano, F. (2007). Non-smooth dynamics of spur gears with manufacturing errors. *Journal of Sound and Vibration*, *306*(1), 271-283..

Chaari, F., Baccar, W., Abbes, M. S., & Haddar, M. (2008). Effect of spalling or tooth breakage on gearmesh stiffness and dynamic response of a one-stage spur gear transmission. *European Journal of Mechanics-A/Solids*,*27*(4), 691-705.

Chaari, F., Fakhfakh, T., & Haddar, M. (2009). Analytical modelling of spur gear tooth crack and influence on gearmesh stiffness. *European Journal of Mechanics-A/Solids*, *28*(3), 461-468.

Cheng, Z., Hu, N., Gu, F., & Qin, G. (2011). Pitting damage levels estimation for planetary gear sets based on model simulation and grey relational analysis. *Transactions of the Canadian Society for Mechanical Engineering*,*35*(3), 403-417.

Choy, F. K., Ruan, Y. F., Zakrajsek, J. J., & Oswald, F. B. (1992). Modal Simulation of Gearbox Vibration with Experimental Correlation (No. NASA-E-7090).

Choy, F. K., Ruan, Y. F., ZAKRAJSEK, J., & Oswald, F. B. (1993). Modal simulation of gear box vibration with experimental correlation. *Journal of Propulsion and Power*, *9*(2), 301-306.

Choy, F. K., Braun, M. J., Polyshchuk, V., Zakrajsek, J. J., & Townsend, D. P. (1994). *Analytical and Experimental Vibration Analysis of a Faulty Gear System* (No. NASA-TM-106689). NATIONAL AERONAUTICS AND SPACE ADMINISTRATION CLEVELAND OH LEWIS RESEARCH CEN TER.

Choy, F. K., Huang, S., Zakrajsek, J. J., Handschuh, R. F., & Townsend, D. P. (1994). *Vibration Signature Analysis of a Faulted Gear Transmission System* (No. NASA-E-8914). NATIONAL AERONAUTICS AND SPACE ADMINISTRATION CLEVELAND OH LEWIS RESEARCH CEN TER.

Comparin, R. J., & Singh, R. (1989). Non-linear frequency response characteristics of an impact pair. *Journal of sound and vibration*, *134*(2), 259-290.

Del Rincon, A. F., Viadero, F., Iglesias, M., García, P., De-Juan, A., & Sancibrian, R. (2013). A model for the study of meshing stiffness in spur gear transmissions. *Mechanism and Machine Theory*, *61*, 30-58.

Diehl, E. J., Tang, J., & DeSmidt, H. (2012). Gear fault modeling and vibration response analysis. In *ASME 2012 5th Annual Dynamic Systems and Control Conference joint with the JSME 2012 11th Motion and Vibration Conference* (pp. 709-718).

Diehl, E. J., & Tang, J. (2016). Predictive Modeling of A Two-Stage Gearbox Towards Fault Detection. *Shock and Vibration*, vol. 2016, Article ID 9638325, 13 pages. doi:10.1155/2016/9638325

Dietl, P., Wensing, J., & Van Nijen, G. C. (2000). Rolling bearing damping for dynamic analysis of multi-body systems—experimental and theoretical results. *Proceedings of the Institution of Mechanical Engineers, Part K: Journal of Multi-body Dynamics*, *214*(1), 33-43.

Ding, H., & Kahraman, A. (2007). Interactions between nonlinear spur gear dynamics and surface wear. *Journal of Sound and Vibration*, *307*(3), 662-679.

Dion, J. L., Le Moyne, S., Chevallier, G., & Sebbah, H. (2009). Gear impacts and idle gear noise: Experimental study and non-linear dynamic model. *Mechanical Systems and Signal Processing*, *23*(8), 2608-2628.

Endo, H., Randall, R. B., & Gosselin, C. (2004). Differential diagnosis of spall versus cracks in the gear tooth fillet region. *Journal of Failure Analysis and Prevention*, *4*(5), 63-71.

Endo H, Randall RB and Gosselin C (2009) Differential diagnosis of spall vs. cracks in the gear tooth fillet region: experimental validation. *Mechanical Systems and Signal Processing* 23(4): 636-651.

Faggioni, M., Samani, F. S., Bertacchi, G., & Pellicano, F. (2011). Dynamic optimization of spur gears. *Mechanism and machine theory*, *46*(4), 544-557.

Feng, Z., Zuo, M. J., & Chu, F. (2010). Application of regularization dimension to gear damage assessment. *Mechanical Systems and Signal Processing*, *24*(4), 1081-1098.

Flodin, A., & Andersson, S. (1997). Simulation of mild wear in spur gears.*Wear*, *207*(1), 16-23.

Gargiulo, E. P. (1980). A simple way to estimate bearing stiffness. *Machine Design*, *52*(17), 107-110.

Guilbault, R., Lalonde, S., & Thomas, M. (2012). Nonlinear damping calculation in cylindrical gear dynamic modeling. *Journal of Sound and Vibration*, *331*(9), 2110-2128.

Guo, Y., & Parker, R. G. (2012). Stiffness matrix calculation of rolling element bearings using a finite element/contact mechanics model.*Mechanism and Machine Theory*, *51*, 32-45.

Guo, Y., Eritenel, T., Ericson, T. M., & Parker, R. G. (2014). Vibro-acoustic propagation of gear dynamics in a gear-bearing-housing system. *Journal of Sound and Vibration*, *333*(22), 5762-5785.

Harris, T. A., & Kotzalas, M. N. (2006). *Rolling bearing analysis*. CRC/Taylor & Francis,.

He, S. (2008). *Effect of sliding friction on spur and helical gear dynamics and vibro-acoustics* (Doctoral dissertation, The Ohio State University).

Heng, A., Zhang, S., Tan, A. C., & Mathew, J. (2009). Rotating machinery prognostics: State of the art, challenges and opportunities. *Mechanical Systems and Signal Processing*, *23*(3), 724-739.

Hiroaki, E., & Nader, S. (2012). *Gearbox Simulation Models with Gear and Bearing Faults*. INTECH Open Access Publisher.

Hotait, M. A., & Kahraman, A. (2013). Experiments on the relationship between the dynamic transmission error and the dynamic stress factor of spur gear pairs. *Mechanism and Machine Theory*, *70*, 116-128.

Howard, I., Jia, S., & Wang, J. (2001). The dynamic modelling of a spur gear in mesh including friction and a crack. *Mechanical systems and signal processing*, *15*(5), 831-853.

Inalpolat, M., Handschuh, M., & Kahraman, A. (2015). Influence of indexing errors on dynamic response of spur gear pairs. *Mechanical Systems and Signal Processing*, *60*, 391-405.

Inoue, T., & Sueoka, A. (2008). Detection of a Small Fault in a Rotating Gear by the Harmonic Wavelet Transform. *Journal of System Design and Dynamics*, 2(1), 197-208.

ISO, I. (1996). 6336-1-1996 Calculation of Load Capacity of Spur and Helical Gears-Part 1: Basic Principles, Introduction and General Influence Factors.

Jardine, A. K., Lin, D., & Banjevic, D. (2006). A review on machinery diagnostics and prognostics implementing condition-based maintenance.*Mechanical systems and signal processing*, *20*(7), 1483-1510.

Jia, S., Howard, I., & Wang, J. (2003). The dynamic modeling of multiple pairs of spur gears in mesh, including friction and geometrical errors.*International Journal of Rotating Machinery*, *9*(6), 437-442.

Jia, S., & Howard, I. (2006). Comparison of localised spalling and crack damage from dynamic modelling of spur gear vibrations. *Mechanical Systems and Signal Processing*, *20*(2), 332-349.

Jones, A. B. (1960). A general theory for elastically constrained ball and radial roller bearings under arbitrary load and speed conditions. *Journal of Basic Engineering*, *82*(2), 309-320.

Kahraman, A., & Singh, R. (1990). Non-linear dynamics of a spur gear pair.*Journal of sound and vibration*, *142*(1), 49-75.

Kahraman, A., & Singh, R. (1991). Non-linear dynamics of a geared rotor-bearing system with multiple clearances. *Journal of sound and vibration*,*144*(3), 469-506.

Kahraman, A., & Singh, R. (1991). Interactions between time-varying mesh stiffness and clearance non-linearities in a geared system. *Journal of Sound and Vibration*, 146(1), 135-156.

Kahraman, A., & Blankenship, G. W. (1996, September). Gear dynamics experiments, Part-II: effect of involute contact ratio. In ASME Power Transmission and Gearing Conference, San Diego, CA.

Kahraman, A., & Blankenship, G. W. (1996, September). Gear dynamics experiments, Part-III: effect of involute tip relief. In ASME Power Transmission and Gearing Conference, San Diego, CA.

Kahraman, A., & Blankenship, G. W. (1997). Experiments on nonlinear dynamic behavior of an oscillator with clearance and periodically time-varying parameters. *Journal of Applied Mechanics*, *64*(1), 217-226.

Kahraman, A., & Blankenship, G. W. (1999). Effect of involute contact ratio on spur gear dynamics. *Journal of Mechanical Design*, *121*(1), 112-118.

Kahraman, A., & Blankenship, G. W. (1999). Effect of involute tip relief on dynamic response of spur gear pairs. *Journal of mechanical design*, *121*(2), 313-315.

Kan, M. S., Tan, A. C., & Mathew, J. (2015). A review on prognostic techniques for non-stationary and non-linear rotating systems. *Mechanical Systems and Signal Processing*, *62*, 1-20.

Kiekbusch, T., & Howard, I. (2007). A common formula for the combined torsional mesh stiffness of spur gears. In *Proceedings of the 5th Australasian Congress on Applied Mechanics* (p. 710). Engineers Australia.

Kiekbusch, T., Sappok, D., Sauer, B., & Howard, I. (2011). Calculation of the combined torsional mesh stiffness of spur gears with two-and three-dimensional parametrical FE models. *Strojniški vestnik-Journal of Mechanical Engineering*, *57*(11), 810-818.

Krämer, E. (1993). *Dynamics of rotors and foundations*. Springer Science & Business Media.

Kraus, J. J. J. S. G., Blech, J. J., & Braun, S. G. (1987). In situ determination of rolling bearing stiffness and damping by modal analysis.*Journal of vibration, acoustics, stress, and reliability in design*, *109*(3), 235-240.

Kubur, M., Kahraman, A., Zini, D. M., & Kienzle, K. (2004). Dynamic analysis of a multi-shaft helical gear transmission by finite elements: model and experiment. *Journal of vibration and acoustics*, *126*(3), 398-406.

Kuang, J. H., & Yang, Y. T. (1992). An estimate of mesh stiffness and load sharing ratio of a spur gear pair. *Advancing power transmission into the 21 st century*, 1-9.

Kuang, J. H., & Lin, A. D. (2001). The effect of tooth wear on the vibration spectrum of a spur gear pair. *Journal of Vibration and Acoustics*, *123*(3), 311-317.

Kubo, A., Yamada, K., Aida, T., & Sato, S. (1972). Research on ultra high speed gear devices. *Trans. Jpn. Soc. Mech. Eng*, *38*, 2692-2715.

Lee, J., Wu, F., Zhao, W., Ghaffari, M., Liao, L., & Siegel, D. (2014). Prognostics and health management design for rotary machinery systems—Reviews, methodology and applications. *Mechanical Systems and Signal Processing*, *42*(1), 314-334.

Leem, S. H., & Choi, J. H. (2013, June). Model-based diagnosis of gear fault under variable loading condition. In *Prognostics and Health Management (PHM), 2013 IEEE Conference on* (pp. 1-6). IEEE.

Lei, Y., & Zuo, M. J. (2009). Gear crack level identification based on weighted K nearest neighbor classification algorithm. *Mechanical Systems and Signal Processing*, *23*(5), 1535-1547.

Lei, Y., Zuo, M. J., He, Z., & Zi, Y. (2010). A multidimensional hybrid intelligent method for gear fault diagnosis. *Expert Systems with Applications*,*37*(2), 1419-1430.

Lewicki, D. G. (2002). Gear Crack Propagation Path Studies-Guidelines for Ultra-Safe Design. *Journal of the American Helicopter Society*, *47*(1), 64-72.

Li, C. J., & Limmer, J. D. (2000). Model-based condition index for tracking gear wear and fatigue damage. *Wear*, *241*(1), 26-32.

Lim, T. C., & Singh, R. (1990). Vibration transmission through rolling element bearings, part I: bearing stiffness formulation. *Journal of sound and vibration*,*139*(2), 179-199.

Lin, H. H., Oswald, F. B., & Townsend, D. P. (1994). Dynamic loading of spur gears with linear or parabolic tooth profile modifications. *Mechanism and Machine Theory*, *29*(8), 1115-1129.

Liu, B., Ling, S. F., & Meng, Q. (1997). Machinery diagnosis based on wavelet packets. *Journal of vibration and control*, 3(1), 5-17.

Liu, B. (2003). Adaptive harmonic wavelet transform with applications in vibration analysis. *Journal of sound and vibration*, *262*(1), 45-64.

Liu, G. (2007). *Nonlinear dynamics of multi-mesh gear systems* (Doctoral dissertation, The Ohio State University).

Liu, G., & Parker, R. G. (2008). Dynamic modeling and analysis of tooth profile modification for multimesh gear vibration. *Journal of Mechanical Design*, *130*(12), 121402.

Lu, Y., Tang, J., & Luo, H. (2012). Wind turbine gearbox fault detection using multiple sensors with features level data fusion. *Journal of Engineering for Gas Turbines and Power*, *134*(4), 042501.

Ma, R., Chen, Y., & Cao, Q. (2012). Research on dynamics and fault mechanism of spur gear pair with spalling defect. *Journal of Sound and Vibration*, 331(9), 2097-2109.

Ma, H., Pang, X., Feng, R., Song, R., & Wen, B. (2015). Fault features analysis of cracked gear considering the effects of the extended tooth contact. *Engineering Failure Analysis*, *48*, 105-120.

Maliha, R., Doğruer, C. U., & Özgüven, H. N. (2004). Nonlinear dynamic modeling of gear-shaft-disk-bearing systems using finite elements and describing functions. *Journal of Mechanical Design*, *126*(3), 534-541.

Meagher, J., Wu, X., Kong, D., & Lee, C. H. (2011). A comparison of gear mesh stiffness modeling strategies. In *Structural Dynamics, Volume 3* (pp. 255-263). Springer New York.

Mohammed, O. D., Rantatalo, M., & Aidanpää, J. O. (2015). Dynamic modelling of a one-stage spur gear system and vibration-based tooth crack detection analysis. *Mechanical Systems and Signal Processing*, *54*, 293-305.

Mosher, M., Pryor, A. H., & Huff, E. M. (2002). Evaluation of standard gear metrics in helicopter flight operation.

Mourad, D., Titouche, N. E., Djaoui, M., & Mohammed, Q. (2008). The calculation of ball bearing nonlinear stiffness theoretical and experimental study with comparisons. *J. Eng. App. Sci*, *3*(11), 872-883.

Munro RG (1962) *The dynamic behavior of spur gears*. PhD Dissertation, University of Cambridge, UK.

Newland, D. E. (1993, October). Harmonic wavelet analysis. In *Proceedings of the Royal Society of London A: Mathematical, Physical and Engineering Sciences* (Vol. 443, No. 1917, pp. 203-225). The Royal Society.

Newland, D. E. (1994). Harmonic and musical wavelets. In*Proceedings of the Royal Society of London A: Mathematical, Physical and Engineering Sciences* (Vol. 444, No. 1922, pp. 605-620). The Royal Society.

Newland, D. E. (1994). Wavelet Analysis of Vibration: Part 1—Theory.*Journal of vibration and acoustics*, *116*(4), 409-416.

Newland DE (1994) Wavelet analysis of Vibration, part II: wavelet maps. *Journal of Vibration and Acoustics* 116(4): 417-425.

Newland, D. E. (1996). *Wavelet analysis of vibration signals* (pp. 585-597). John Wiley & Sons, Inc..

Newland, D. E. (1999). Harmonic wavelets in vibrations and acoustics.*Philosophical Transactions of the Royal Society of London A: Mathematical, Physical and Engineering Sciences*, *357*(1760), 2607-2625.

Omar, F. K., Moustafa, K. A., & Emam, S. (2011). Mathematical modeling of gearbox including defects with experimental verification. *Journal of Vibration and Control*, 1077546311403791.

Omar, F. K., & Gaouda, A. M. (2012). Dynamic wavelet-based tool for gearbox diagnosis. *Mechanical Systems and Signal Processing*, *26*, 190-204.

Oswald, F. B., Rebbechi, B., Zakrajsek, J. J., Townsend, D. P., & Lin, H. H. (1991). *Comparison of analysis and experiment for dynamics of low-contact-ratio spur gears* (No. NASA-E-5648). NATIONAL AERONAUTICS AND SPACE ADMINISTRATION CLEVELAND OH LEWIS RESEARCH CENTER.

Oswald, F. B., Seybert, A. F., Wu, T. W., & Atherton, W. (1992). *Comparison of analysis and experiment for gearbox noise* (No. NASA-E-6696). NATIONAL AERONAUTICS AND SPACE ADMINISTRATION CLEVELAND OH LEWIS RESEARCH CENTER.

Özgüven, H. N., & Houser, D. R. (1988). Mathematical models used in gear dynamics—a review. *Journal of sound and vibration*, *121*(3), 383-411.

Özgüven, H. N. (1991). A non-linear mathematical model for dynamic analysis of spur gears including shaft and bearing dynamics. *Journal of Sound and Vibration*, *145*(2), 239-260.

Palmgren, A. (1959). Ball and roller bearing engineering. *Philadelphia: SKF Industries Inc., 1959*, *1*.

Parey, A., & Tandon, N. (2003). Spur gear dynamic models including defects: A review. *The Shock and Vibration Digest*, *35*(6), 465-478.

Parey, A., El Badaoui, M., Guillet, F., & Tandon, N. (2006). Dynamic modelling of spur gear pair and application of empirical mode decomposition-based statistical analysis for early detection of localized tooth defect.*Journal of sound and vibration*, *294*(3), 547-561.

Parey, A., & Tandon, N. (2010). Fault detection of spur gears using vibration monitoring. *Lambert, Saarbrucken, Germany*.

Park, H. G., & Zak, M. (2003). Gray-box approach for fault detection of dynamical systems. *Journal of dynamic systems, measurement, and control*, *125*(3), 451-454.

Parker, R. G., Vijayakar, S. M., & Imajo, T. (2000). Non-linear dynamic response of a spur gear pair: modelling and experimental comparisons.*Journal of Sound and vibration*, *237*(3), 435-455.

Parker, R. G., Guo, Y., Eritenel, T., & Ericson, T. M. (2012). Vibration propagation of gear dynamics in a gear-bearing-housing system using mathematical modeling and finite element analysis. *NASA Contractor Report NASA/CR-2012-217664, NASA*.

Peng, Z. K., & Chu, F. L. (2004). Application of the wavelet transform in machine condition monitoring and fault diagnostics: a review with bibliography. *Mechanical systems and signal processing*, *18*(2), 199-221.

Peng, Y., Dong, M., & Zuo, M. J. (2010). Current status of machine prognostics in condition-based maintenance: a review. *The International Journal of Advanced Manufacturing Technology*, *50*(1-4), 297-313.

Randall, R. B. (1982). A new method of modeling gear faults. *Journal of Mechanical Design*, *104*(2), 259-267.

Randall, R. B. (1984). Separating excitation and structural response effects in gearboxes. In *International Conference on Vibrations in Rotating Machinery, 3 rd, Heslington, England* (pp. 101-107).

Randall, R. B. (1987). *Frequency analysis*. Brül & Kjor.

Randall, R. B., & Kelly, D. W. (1990). Analytical and Experimental Vibration Analysis of a Gearbox Casing. In *Australian Vibration and Noise Conference 1990: Vibration and Noise-measurement Prediction and Control; Preprints of Papers* (p. 68). Institution of Engineers, Australia.

Randall, R. B. (2004). State of the art in monitoring rotating machinery-part 1.*Sound and vibration*, *38*(3), 14-21.

Randall, R. B. (2004). State of the art in monitoring rotating machinery-part 2.*Sound and Vibration*, *38*(5), 10-17.

Randall, R. B. (2011). Vibration-based condition monitoring: industrial, aerospace and automotive applications. John Wiley & Sons.

Ruiz, B. J. A., López, J. F. L., & Riaza, H. F. Q. (2013, September). Vibration analysis in gear damage: Mathematical modeling and experimental validation. In *Symposium of Signals, Images and Artificial Vision-2013: STSIVA-2013* (pp. 1-5). IEEE.

Sait, A. S., & Sharaf-Eldeen, Y. I. (2011). A review of gearbox condition monitoring based on vibration analysis techniques diagnostics and prognostics. In *Rotating Machinery, Structural Health Monitoring, Shock and Vibration, Volume 5* (pp. 307-324). Springer New York.

Samuel, P. D., Pines, D. J., & Lewicki, D. G. (2000). A Comparison of Stationary and Non-Stationary Metrics for Detecting Faults in Helicopter Gearboxes. *Journal of the American Helicopter Society*, 45(2), 125-136.

Samuel, P. D., & Pines, D. J. (2005). A review of vibration-based techniques for helicopter transmission diagnostics. *Journal of sound and vibration*,*282*(1), 475-508.

Sawalhi, N., & Randall, R. B. (2008). Simulating gear and bearing interactions in the presence of faults: Part I. The combined gear bearing dynamic model and the simulation of localised bearing faults. *Mechanical Systems and Signal Processing*, *22*(8), 1924-1951.

Sawalhi, N., & Randall, R. B. (2008). Simulating gear and bearing interactions in the presence of faults: Part II: Simulation of the vibrations produced by extended bearing faults. *Mechanical Systems and Signal Processing*, *22*(8), 1952-1966.

Scheffer, C., & Girdhar, P. (2004). *Practical machinery vibration analysis and predictive maintenance*. Elsevier.

Shigley, J. E., Mischke, C. R., & Budynas, R. G. (2015). *Mechanical engineering design*. McGraw-Hill,.

Sikorska, J. Z., Hodkiewicz, M., & Ma, L. (2011). Prognostic modelling options for remaining useful life estimation by industry. *Mechanical Systems and Signal Processing*, *25*(5), 1803-1836.

Smallwood, D. (2011). Using a Modified Harmonic Wavelet Transform to Characterize Mechanical Shock. *Journal of the IEST*, *54*(2), 85-102.

SpectraQuest (2009) *Gearbox dynamics simulator operating manual*. Available at: http://spectraquest.com/drivetrains/details/gds/ (accessed 13 May 2011)

Tamminana V, Kahraman A and Vijayakar S (2007) A study of the relationship between the dynamic factors and the dynamic transmission error of spur gear pairs. *Journal of Mechanical Design* 129(): 75-84.

Tian, Z., Zuo, M. J., & Wu, S. (2012). Crack propagation assessment for spur gears using model-based analysis and simulation. *Journal of Intelligent Manufacturing*, *23*(2), 239-253.

Velex, P., & Maatar, M. (1996). A mathematical model for analyzing the influence of shape deviations and mounting errors on gear dynamic behaviour. *Journal of Sound and Vibration*, 191(5), 629-660.

Velex, P., & Ajmi, M. (2007). Dynamic tooth loads and quasi-static transmission errors in helical gears–Approximate dynamic factor formulae.*Mechanism and Machine Theory*, *42*(11), 1512-1526.

Velex, P. (2012). On the modelling of spur and helical gear dynamic behaviour. *arXiv preprint arXiv:1204.2636*.

Walha, L., Fakhfakh, T., & Haddar, M. (2009). Nonlinear dynamics of a two-stage gear system with mesh stiffness fluctuation, bearing flexibility and backlash. *Mechanism and Machine Theory*, *44*(5), 1058-1069.

Wan, Z., Cao, H., Zi, Y., He, W., & He, Z. (2014). An improved time-varying mesh stiffness algorithm and dynamic modeling of gear-rotor system with tooth root crack. *Engineering Failure Analysis*, *42*, 157-177.

Wang, J., Li, R., & Peng, X. (2003). Survey of nonlinear vibration of gear transmission systems. *Applied Mechanics Reviews*, *56*(3), 309-329.

Wang, J., & Howard, I. (2004). The torsional stiffness of involute spur gears.*Proceedings of the Institution of Mechanical Engineers, Part C: Journal of Mechanical Engineering Science*, *218*(1), 131-142.

Wang, J., & Howard, I. (2005). Finite element analysis of high contact ratio spur gears in mesh. *Journal of tribology*, *127*(3), 469-483.

Wang, J. D., & Howard, I. M. (2006). Error analysis on finite element modeling of involute spur gears. *Journal of Mechanical Design*, *128*(1), 90-97.

Wang, W. J., & McFadden, P. D. (1996). Application of wavelets to gearbox vibration signals for fault detection. *Journal of sound and vibration*, *192*(5), 927-939.

Wang, W., & Wong, A. K. (2002). Autoregressive model-based gear fault diagnosis. *Journal of vibration and acoustics*, *124*(2), 172-179.

Wang, W. (2003). An evaluation of some emerging techniques for gear fault detection. *Structural Health Monitoring*, *2*(3), 225-242.

While, M. F. (1979). Rolling element bearing vibration transfer characteristics: effect of stiffness. *Journal of applied mechanics*, *46*(3), 677-684.

Wu, S., Zuo, M. J., & Parey, A. (2008). Simulation of spur gear dynamics and estimation of fault growth. *Journal of Sound and Vibration*, *317*(3), 608-624.

Yan, R., & Gao, R. X. (2005). An efficient approach to machine health diagnosis based on harmonic wavelet packet transform. *Robotics and Computer-Integrated Manufacturing*, *21*(4), 291-301.

Yan, R., & Gao, R. X. (2010). Harmonic wavelet-based data filtering for enhanced machine defect identification. *Journal of Sound and Vibration*,*329*(15), 3203-3217.

Yan, R., Gao, R. X., & Chen, X. (2014). Wavelets for fault diagnosis of rotary machines: A review with applications. *Signal Processing*, *96*, 1-15.

Yang, J. (2013). Vibration analysis on multi-mesh gear-trains under combined deterministic and random excitations. *Mechanism and Machine Theory*, *59*, 20-33.

Yen, G. G., & Lin, K. C. (2000). Wavelet packet feature extraction for vibration monitoring. *IEEE transactions on industrial electronics*, 47(3), 650-667.

Yesilyurt, I., Gu, F., & Ball, A. D. (2003). Gear tooth stiffness reduction measurement using modal analysis and its use in wear fault severity assessment of spur gears. *NDT & E International*, *36*(5), 357-372.

Zakrajsek, J. J., Townsend, D. P., & Decker, H. J. (1993). *An analysis of gear fault detection methods as applied to pitting fatigue failure data* (No. NASA-E-7470). NATIONAL AERONAUTICS AND SPACE ADINISTRATION CLEVELAND OH LEWIS RESEARCH CENTER.

Zhou X, Shao Y, Lei Y and Zuo M (2012) Time-varying meshing stiffness calculation and vibration analysis for a 16DOF dynamic model with linear crack growth in a pinion. *Journal of Vibration and Acoustics* 134(2): 1-11.

Zorzi, E., & Walton, J. (1982). Evaluation of shear mounted elastomeric damper.